

D I S S E R T A T I O N

SURFACE REACTIVITY AND HOMOEPITAXIAL GROWTH OF STRONTIUM TITANATE (110)

Ausgeführt zum Zwecke der Erlangung des akademischen Grades eines Doktors
der technischen Wissenschaften unter der Leitung von

Univ.Prof. Dr.techn. Ulrike Diebold
Institut für Angewandte Physik (E134)

und mitbetreut von

Ao.Univ.Prof. Dr.techn. Michael Schmid
Institut für Angewandte Physik (E134)

eingereicht an der Technischen Universität Wien
Fakultät für Physik

von

Stefan Gerhold
e0626843
Grundsteingasse 22/207, 1160 Wien

Wien, Mai 2016

Acknowledgement

I would like to express my gratitude to everyone who has supported me during the last three years and made it possible for me to perform this PhD work.

First of all, I would like to thank my supervisor Prof. Ulrike Diebold for giving me the opportunity to work in the very interesting field of surface physics in her research group at TU Wien. I am grateful for all the discussions and the help in interpreting the results presented in this thesis. Many thanks go to my colleagues at TU Wien. I am especially grateful for many fruitful discussions with Michael Schmid, Zhiming Wang, and Michele Riva. I also very much appreciated the motivating and friendly environment in this research group.

In addition, I would like to thank my parents Renate and Franz, and my girlfriend Birgit for supporting me throughout my studies. It would not have been possible without you.

Finally, I gratefully acknowledge financial support by the European Research Council (ERC) Advanced Grant “OxideSurfaces”, and the Austrian Science Fund (FWF) project F45-07 (FOXSI), as well as project W1243 (Solids4Fun).

Abstract

This thesis focuses on the experimental investigation of the (110) surface of strontium titanate (SrTiO_3 , STO). SrTiO_3 is a complex oxide of the perovskite class. It exhibits a wide range of interesting properties. For example, it is well known for its photocatalytic activity, and it is widely used as a substrate for the growth of complex oxides.

Experimental results about the preparation and properties of different STO(110) surface reconstructions are presented. The samples have been studied using scanning tunneling microscopy (STM), photoemission spectroscopy (XPS and UPS), X-ray absorption spectroscopy (XAS), low-energy- and high-energy electron diffraction (LEED and RHEED), and low-energy ion scattering spectroscopy (LEIS). Experiments were conducted in different ultra-high vacuum (UHV) chambers.

Well-defined STO(110) surfaces with specific surface reconstructions were prepared by sputtering and annealing. Central to surface preparation is the phase diagram established by Wang *et al.* [Phys. Rev. B, 83, 155453 (2011)]. It describes the dependence of the surface reconstructions on the near-surface stoichiometry. This enables us to switch between surface reconstructions on STO(110) by deposition of Ti or Sr metal and subsequent annealing. Furthermore, it allows to associate changes in the surface reconstruction of thin films grown by pulsed laser deposition (PLD) with the stoichiometry of the deposited film.

The already established structure model of the $\text{SrTiO}_3(110)-(4\times 1)$ surface reconstruction is discussed, and its experimental characterization by means of STM, LEED, RHEED, and XAS is shown. In addition, the transition (induced by reactive Ti growth) from $(n\times 1)$ ($n = 4-6$) to $(2\times m)$ ($m = 4, 5$) reconstructions on the STO(110) surface is discussed, and the (2×5) surface structure is characterized by highly-resolved STM, LEED, and XAS. XAS reveals a change from tetrahedral coordination of Ti in the (4×1) reconstruction, to a surface where Ti is in octahedral coordination for the (2×5) structure. A model of the (2×5) structure, as well as details about its preparation are presented.

The second part of this thesis discusses the surface chemistry of the (4×1) reconstruction. I present results about the interaction of water with this surface, and

how its properties change upon adsorption of Ni metal, and NiO_x clusters. The results showed that the $\text{SrTiO}_3(110)-(4\times 1)$ surface is inert towards the adsorption of water. Water adsorbs molecularly only at low temperatures, while it adsorbs dissociatively on the reduced surface at surface oxygen vacancies. The identification of surface hydroxyls, oxygen vacancies, and molecularly adsorbed water on this surface by STM is shown.

Ni metal adsorbs on the (4×1) surface at room temperature as single adatoms at specific sites in the surface reconstruction unit cell. Mild annealing leads to clustering of the atoms. The adsorption of Ni adatoms is characterized by means of STM, XPS, and UPS.

The system $\text{NiO}_x\text{-SrTiO}_3$ has recently been found to be active in the photocatalytic splitting of water, which motivated the study of the adsorption of NiO_x on the (4×1) surface. Adsorbed NiO_x was characterized by means of STM, XPS, and UPS. NiO_x does not grow epitaxially on this surface – only disordered patches were observed in STM. XPS and UPS results indicate the dissociative adsorption of water on the NiO_x -modified surface. Furthermore, the results suggest that the adsorption of NiO_x influences the band structure of STO in a way that increases its photocatalytic activity.

The third part of this thesis is about the homoepitaxial growth of SrTiO_3 by pulsed laser deposition (PLD). PLD is a physical vapor deposition technique, often used for the growth of complex oxides. We have recently started the operation of our new PLD system with *in-situ* growth analysis with RHEED, and present our approach of combining high-pressure growth with ultra-high vacuum surface science. The PLD system is connected to the analysis chamber, allowing for the rapid *in-vacuo* transfer of as-grown films to perform surface analysis. In order to obtain control over the new growth technique, we performed homoepitaxial growth studies on the (4×1) reconstructed surface of $\text{STO}(110)$. Homoepitaxy provides the advantage of performing growth studies without the influence of interface strain. Therefore, the dependence of the growth characteristics on the deposition parameters (UV laser fluence and background pressure) could directly be monitored. Pristine surfaces were prepared to exhibit predominantly the (4×1) reconstruction.

By deposition of sub-monolayer amounts under different conditions, the influence of the deposition parameters on the island density and the surface morphology is shown. We verified the correlation between RHEED intensity oscillations and ideal 2D layer-by-layer growth. By directly relating variations in the RHEED intensity with the actual density of steps on the surface, as determined by STM, we were able to refine the step density model. This model explains such variations in the RHEED specular spot intensity by variations of the step density on the surface. The results indicate that, in addition to the steps introduced by the islands circumference, also the interfaces between inherently different reconstruction coexisting on the surface have to be taken into account.

The final chapter of this thesis presents growth studies of up to 39 ML-thick homoepitaxial films. The influence of the deposition parameters on the morphology and structure of the film surface was investigated, and island growth on different STO(110) surfaces was characterized. The results indicate that the pristine surface structure has a strong influence on the morphology of the resulting thin film. In addition, a change in the surface structure during deposition was observed. Using the calibrated phase diagram of STO(110), the stoichiometry of the PLD-grown film can be determined with a high accuracy.

Kurzfassung

Im Zuge dieser Dissertation wurde die (110) Oberfläche von Strontiumtitanat (SrTiO_3 , STO) untersucht. SrTiO_3 ist ein Oxid aus der Klasse der kubischen Perowskite, das für eine Vielzahl interessanter Effekte bekannt ist, unter anderem für die photo-katalytische Dissoziation von Wassermolekülen auf der Oberfläche und für seine Verwendung als Substrat für das Wachstum von komplexen Oxidschichten. In dieser Dissertation wurden mit Hilfe der experimentellen Methoden der Rastertunnelmikroskopie (STM), der niederenergetischen und hochenergetischen Elektronenbeugung (LEED und RHEED), der Photoemissionsspektroskopie (XPS und UPS), der Röntgenabsorptionsspektroskopie (XAS), sowie der niederenergetischen Ionenstreuung (LEIS) die Erzeugung und die Eigenschaften einiger Rekonstruktionen auf der $\text{SrTiO}_3(110)$ Oberfläche untersucht. Alle Experimente fanden in Ultrahochvakuumkammern statt.

Wohl-definierte Oberflächen mit einer bestimmten Rekonstruktion wurden durch Argon-Ionen-Zerstäubung und Ausheilen in Sauerstoff präpariert. Wang *et al.* [Phys. Rev. B, 83, 155453 (2011)] entwickelten ein Oberflächen-Phasendiagramm, welches zeigt, dass man auf der $\text{SrTiO}_3(110)$ Oberfläche durch Aufdampfen von Titan oder Strontium und Ausheilen in Sauerstoff zwischen mehreren Rekonstruktionen reproduzierbar hin- und herwechseln kann. Mit dieser Herangehensweise konnte für alle Experimente eine überwiegend (4×1) rekonstruierte Oberfläche erzeugt werden.

Im ersten Teil dieser Dissertation wird das bereits etablierte Strukturmodell der (4×1) Rekonstruktion diskutiert und diese Oberflächenstruktur mit STM, LEED, RHEED, und XAS charakterisiert. Weiters wird der Übergang von $(n\times 1)$ ($n = 4-6$) zu $(2\times m)$ ($m = 4, 5$) Rekonstruktionen durch reaktive Deposition von Ti beschrieben. Die (2×5) Rekonstruktion wurde mit STM, LEED, und XAS untersucht. Die Resultate zeigen, dass sich die Koordination der Ti Atome an der Oberfläche bei dem Übergang von $(n\times 1)$ nach $(2\times m)$ von tetraedrisch nach oktaedrisch ändert. Weiters wird das Strukturmodell dieser Rekonstruktion diskutiert und deren Präparation beschrieben.

Der zweite Teil behandelt die Oberflächenchemie der (4×1) Rekonstruktion. Die

Adsorption von Wasser auf dieser Oberfläche wurde untersucht. Die Resultate zeigen, dass Wasser auf der stöchiometrischen Oberfläche bei Raumtemperatur nicht adsorbiert. Einzig bei tiefen Temperaturen adsorbieren Wassermoleküle in ihrer molekularen Form, während die reduzierte Oberfläche und die damit assoziierten Sauerstofffehlstellen die dissoziative Adsorption von Wassermolekülen ermöglichen. Mittels STM konnten adsorbierter atomarer Wasserstoff (*i.e.*, Oberflächen-Hydroxylgruppen), Sauerstofffehlstellen und molekular adsorbierte Wassermoleküle, sowie deren Adsorptionsgeometrie festgestellt werden.

Die Adsorption von Nickel auf der (4×1) Oberfläche wurde ebenfalls untersucht. STM Resultate zeigen, dass einzelne Nickel Adatome bei Raumtemperatur auf dieser Oberfläche stabilisiert werden. Weiters zeigt STM, dass diese Adatome an speziellen Plätzen in der Einheitszelle der Oberflächenrekonstruktion sitzen. Leichtes Heizen der Probe führt zum Sintern der Adatome und dadurch zur Bildung von Clustern auf der Oberfläche.

Da bereits seit Längerem bekannt ist, dass die Kombination von SrTiO_3 mit Nickeloxid (NiO_x) eine hohe Aktivität in der photokatalytischen Dissoziation von Wasser zeigt, wurde die Adsorption von NiO_x auf der $\text{SrTiO}_3(110)-(4 \times 1)$ Oberfläche untersucht. NiO_x wächst auf dieser Oberfläche in ungeordneten Inseln. XPS-, UPS-, und LEIS-Resultate zeigen, dass Wasser auf der NiO_x -modifizierten Oberfläche in dissoziativer Weise adsorbiert. Des Weiteren zeigen diese Resultate, dass die Adsorption von NiO_x die Bandstruktur von STO in für die Photokatalyse günstiger Art und Weise verändert.

Der dritte Teil dieser Dissertation zeigt Resultate über das homoepitaktische Wachstum von dünnen SrTiO_3 Schichten mittels gepulster Laser-deposition (PLD). PLD gehört zu den Methoden der physikalischen Gasphasenabscheidung und wird häufig für das Wachstum komplexer Oxid-Schichten herangezogen. Die neue PLD Maschine wurde erst kürzlich in Betrieb genommen und es wird unser Ansatz beschrieben, um die Methode des PLD-Wachstums mit Ultrahochvakuum Oberflächenanalyse zu vereinbaren. Das neue System kombiniert das PLD Wachstum mit RHEED. Dadurch kann die Dicke der Schicht während des Wachstums gemessen werden. Da die PLD-Vakuumkammer direkt mit der Oberflächenanalysekammer

verbunden ist, können dünne Schichten direkt nach dem Wachstum *in-vacuo* untersucht werden, ohne sie der Atmosphäre auszusetzen. Um Kontrolle über das PLD-Verfahren zu erhalten, wurde das homoepitaktische Wachstum auf der STO(110) Oberfläche untersucht. Homoepitaxie ermöglicht die Studie von Wachstumsprozessen ohne dem Einfluss von Spannungen an der Grenzfläche zwischen Substrat und dünnem Film. Die Resultate zeigen daher direkt den Einfluss der Depositionsparameter (UV Laserfluenz und Gasdruck beim Schichtwachstum) auf das Wachstum. Für jede Deposition wurde die Probe erneut präpariert. Durch systematisches Ändern der Depositionsparameter während des Wachstums von sub-Monolagen-dicken Schichten haben wir den Einfluss dieser Parameter auf die Inseldichte und auf die Morphologie der Oberfläche untersucht. Die Resultate zeigen, dass Oszillation der RHEED-Intensität direkt mit optimalen 2D Schichtwachstum korrelieren. Das Modell der Stufendichte erklärt Oszillationen der RHEED-Intensität während des Wachstums mit Oszillationen der Stufendichte auf der Oberfläche. Die Ergebnisse deuten darauf hin, dass zusätzlich zu den Stufenkanten welche durch den Umfang der Inseln auf der Oberfläche erzeugt werden, auch die Grenze zwischen zwei unterschiedlichen Rekonstruktionen auf den Inseln selbst zur Stufendichte beitragen.

Abschließend werden Resultate über das homoepitaktische Wachstum von bis zu 39 Monolagen dicken Schichten gezeigt. Auch hier wurde der Einfluss der Depositionsparameter auf die Struktur und die Morphologie dieser Schichten bestimmt. Die Resultate zeigen, dass die Morphologie der Oberfläche des dünnen Films stark von der Zusammensetzung der ursprünglichen Oberflächenrekonstruktionen abhängt. Durch Heranziehen des STO(110) Oberflächen-Phasendiagramms kann über die Änderungen der Oberflächenstruktur während des Wachstums auf die Zusammensetzung der dünnen Schicht geschlossen werden. Dies ermöglicht eine präzise Bestimmung der Stöchiometrie dieser dünnen Schichten.

Publication list

- Paper I** **Photoelectron angular distributions of Cu, Ag, Pt and Au samples: experiments and simulations**
Tasneem G., Tomastik C., Gerhold S., Werner W.S.M., Smekal W., Powell C.J.
Surf. Interface Anal. 43 (2011) 934
- Paper II** **Water Adsorption at the Tetrahedral Titania Surface Layer of SrTiO₃(110)-(4×1)**
Wang Z., Hao X., Gerhold S., Novotny Z., Franchini C., McDermott E., Schulte K., Schmid M., Diebold U.
J. Phys. Chem. C 117 (2013) 26060
- Paper III** **Stoichiometry-Driven Switching Between Surface Reconstructions on SrTiO₃(001)**
Gerhold S., Wang Z., Schmid M., Diebold U.
Surf. Sci. 621 (2014) L1
- Paper IV** **Anisotropic Two-Dimensional Electron Gas at SrTiO₃(110)**
Wang Z., Zhong Z., Hao X., Gerhold S., Stöger B., Schmid M., Sanchez-Barriga J., Varykhalov A., Franchini C., Held K., Diebold, U.
Proc. Natl. Acad. Sci. USA 111 (2014) 3933
- Paper V** **Vacancy Clusters at Domain Boundaries and Band Bending at the SrTiO₃(110) Surface**
Wang Z., Hao X., Gerhold S., Schmid M., Franchini C., Diebold U.
Phys. Rev. B 90 (2014) 035436
- Paper VI** **Stabilizing Single Ni Adatoms on a Two-Dimensional Porous Titania Overlayer at the SrTiO₃(110) Surface**
Wang Z., Hao X., Gerhold S., Mares P., Wagner M., Bliem R., Schulte K., Schmid M., Franchini C., Diebold U.
J. Phys. Chem. C 118 (2014) 19904

- Paper VII** **Nickel-Oxide-Modified $\text{SrTiO}_3(110)-(4\times 1)$ Surfaces and Their Interaction with Water**
Gerhold S., Riva M., Wang Z., Bliem R., Wagner M., Osiecki J., Schulte K., Schmid M., Diebold U.
J. Phys. Chem. C 119 (2015) 20481
- Paper VIII** **Adsorption and Incorporation of Transition Metals at the Magnetite $\text{Fe}_3\text{O}_4(001)$ Surface**
 Bliem R., Pavelec J., Gamba O., McDermott E., Wang Z., Gerhold S., Wagner M., Osiecki J., Schulte K., Schmid M., Blaha P., Diebold U., Parkinson G.S.
Phys. Rev. B 92 (2015) 075440
- Paper IX** **Adjusting Island Density and Morphology of the $\text{SrTiO}_3(110)-(4\times 1)$ Surface: Pulsed Laser Deposition Combined with Scanning Tunneling Microscopy**
Gerhold S., Riva M., Yildiz B., Schmid M., Diebold U.
Surf. Sci. 651 (2016) 76
- Paper X** **Transition From Reconstruction Toward Thin Film on the (110) Surface of Strontium Titanate**
 Wang Z., Loon A., Subramanian A., Gerhold S., McDermott E., Enterkin J. A., Hieckel M., Russell B. C., Green R. J., Moewes A., Guo J., Blaha P., Castell M.R., Diebold U., Marks L.D.
Nano Lett. 16 (2016) 2407
- Paper XI** **$\text{Fe}_3\text{O}_4(110)-(1\times 3)$ Revisited: Periodic (111) Nanofacets**
 Parkinson G. S., Lackner P., Gamba O., Maaß S., Gerhold S., Riva M., Bliem R., Diebold U., Schmid M.
Surf. Sci. 649 (2016) 120

Paper XII Homoepitaxial Growth of $\text{SrTiO}_3(110)-(4\times 1)$ Surface: Influence of Surface Structure on the Growth and Determination of the PLD-grown Film Stoichiometry

Gerhold S., Riva M., Yildiz B., Schmid M., Diebold U.

Manuscript in preparation

Paper XIII Bridging the gap: New experimental approach to oxygen tracer diffusion on $\text{SrTiO}_3(110)$

Riva M., Kubicek M., Gerhold S., Yildiz B., Franchini C., Franceschi G., Schmid M., Fleig J., Diebold U.

Manuscript in preparation

Papers that are discussed in this thesis and my contribution to each of them:

Many people were involved in the experimental studies that are combined in the publications mentioned above. Here, I will shortly list my contribution to these papers.

In papers **I**, **IV**, **VIII**, and **XI**, I had only a minor contribution to the design of the experiment, experimental work, and interpretation of the data.

In papers **II**, **V**, **VI**, **X**, and **XIII**, I had only a minor contribution to the design of the experiments, while I had considerably contributed to the experimental work, and data analysis.

I had a larger responsibility for papers **III**, **VII**, **IX**, and **XII**, for which I designed the experiments, did a large part of the data analysis, and wrote the manuscripts.

The results presented in this thesis have to a large extent been published in papers **II**, **V**, **VI**, **VII**, **IX**, and **X**.

Theoretical calculations presented in papers **II**, **IV**, **V**, and **VI** were performed by Xianfeng Hao and Cesare Franchini.

Contents

1. Introduction	1
1.1. Metal oxides and surface science	1
1.2. Strontium titanate	4
2. Experimental techniques and setups	10
2.1. Photoemission spectroscopy (XPS and UPS)	10
2.2. X-ray absorption spectroscopy (XAS)	11
2.3. Low-energy He-ion scattering spectroscopy (LEIS)	14
2.4. Scanning tunneling microscopy (STM)	16
2.5. Low-energy electron diffraction (LEED)	17
2.6. Pulsed laser deposition (PLD)	18
2.7. Reflection high-energy electron diffraction (RHEED)	19
2.8. X-ray diffraction (XRD)	20
2.9. SPECS setup	21
2.10. Pulsed laser deposition (PLD): Chamber and Procedures	22
2.11. Strontium titanate samples	26
3. Results	28
3.1. SrTiO ₃ (110) surface reconstructions	28
3.1.1. SrTiO ₃ (110)-(4×1) surface reconstruction	28
3.1.2. Transition from ($n \times 1$) to ($2 \times m$) reconstructions	38
3.2. SrTiO ₃ (110)-(4×1) and its interaction with H ₂ O	48
3.2.1. Water adsorption in STM	48
3.2.2. Water adsorption in PES	53

Contents

3.2.3.	Summary and discussion: H ₂ O adsorption on SrTiO ₃ (110)- (4×1)	56
3.3.	Single Ni adatoms on the SrTiO ₃ (110)-(4×1) surface	58
3.3.1.	Adsorption of Ni adatoms in STM	59
3.3.2.	Adsorption of Ni adatoms in PES	63
3.3.3.	Summary and discussion: Ni adatoms and clusters on SrTiO ₃ (110)- (4×1) surface	64
3.4.	NiO clusters on the SrTiO ₃ (110)-(4×1) surface	67
3.4.1.	NiO cluster on (4×1) in XPS/UPS	68
3.4.2.	NiO clusters on the (4×1) surface in STM	71
3.4.3.	NiO cluster on (4×1) in NEXAFS	74
3.4.4.	Water interaction with NiO-modified SrTiO ₃ (110)-(4×1) . .	77
3.4.5.	Summary and discussion: NiO and H ₂ O on SrTiO ₃ (110)- (4×1) surface	78
3.5.	Early stages of homoepitaxial film growth of STO(110) by PLD . .	82
3.5.1.	Island nucleation on the SrTiO ₃ (110)-(4×1) surface	82
3.5.2.	RHEED oscillations corresponding to layer-by-layer growth .	86
3.5.3.	Verification and extension of the step density model	87
3.5.4.	Substrate temperature versus island density and shape . . .	90
3.5.5.	Using the UV laser repetition rate to tune the growth mode	91
3.5.6.	Summary: Early stages of STO(110)-(4×1) homoepitaxial growth	91
3.6.	Homoepitaxial growth of multi-layer films of STO(110) by PLD . .	95
3.6.1.	Overview and Background	95
3.6.2.	Stoichiometry measured by XPS	99
3.6.3.	Slightly Sr-rich growth	101
3.6.4.	Slightly Ti-rich growth	104
3.6.5.	Test-experiments	106
3.6.6.	Using the evolution of surface reconstructions to determine the stoichiometry of thin films	111
3.6.7.	Test-experiment: Ex-situ XRD characterization	112

Contents

3.6.8. Discussion: Homoepitaxial multi-layer films on STO(110) and STM-derived stoichiometry determination	114
4. Summary	117
Bibliography	122
Appendix A. Appendix	136
A.1. Determination of UV laser spot size	136
A.2. Reproducible alignment of target and substrate	136
A.3. Magnetic Disturbances influencing the RHEED	138

1. Introduction

1.1. Metal oxides and surface science

Most of the elements in the periodic table are metals. Since metal atoms tend to form strong bonding with oxygen, there is a high abundance of metal oxides in the environment, appearing either as bulk oxides or as passivating thin oxide films [1]. Fortunately, metal oxides exhibit very interesting and diverse properties, and have a high potential for applications. For example, the electrical properties of oxides can vary from wide-bandgap insulators (Al_2O_3), via semiconductors (SrTiO_3), to high- T_c superconductors ($\text{YBa}_2\text{Cu}_3\text{O}_{7-x}$) [2]. In most applications, the surfaces of the metal oxides are responsible for device functioning, *e.g.*, in heterogeneous and photo-catalysis, or in gas-sensing devices. Therefore, a detailed understanding of the surface electronic and geometric structure is key for tailoring the properties of these materials [3]. The crystal structure of metal oxides can vary from the simple rock salt structure like in NiO [4], which is formed by placing metal cations into each of the octahedral interstices formed by an fcc oxygen anion lattice, to more complicated crystal structures such as the perovskites. Perovskites have the chemical formula ABO_3 with A and B being metal cations (in SrTiO_3 , A and B cations exhibit formal charges of +4 and +2, respectively), and O stands for oxygen with -2 formal charge. Figure 1.1 shows a unit cell of the ABO_3 crystal structure. It consists of corner-sharing BO_6 octahedra and 12-fold coordinated A-cations centered between the BO_6 units. Depending on which metal cations sit on the A and B site, the crystal structure can be slightly distorted. Goldschmidt systematically evaluated X-ray diffraction data of many perovskite compounds and derived a relation between the ionic radii of the constituents (r_A , r_B , and r_O) and

1. Introduction

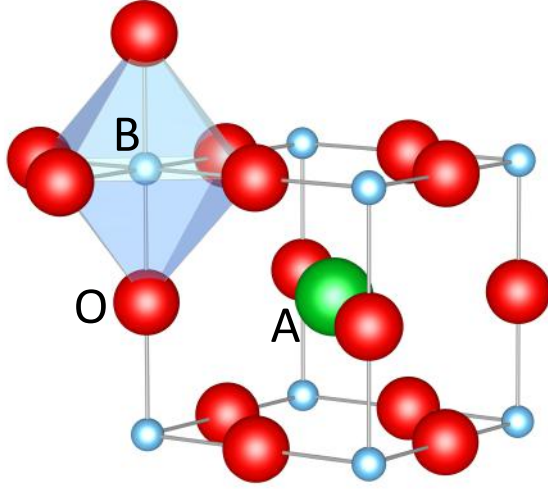


FIGURE 1.1.: Unit cell of the cubic perovskite structure. A or B, and O indicate metal cations, and oxygen anions.

the stability and degree of distortion of the lattice of the resulting ABO_3 material ($t \dots$ Goldschmidt tolerance factor): [5]

$$t = \frac{r_A + r_O}{\sqrt{2}(r_B + r_O)} \quad (1.1)$$

In a range of $0.71 < t < 1$ the perovskite is stable, with crystallization into the cubic perovskite phase in the range of $0.9 < t < 1$.

The physical and chemical properties of perovskite oxides also vary in a large range. For example, from wide-bandgap semiconductors (SrTiO_3) that can be readily made conductive by creation of oxygen vacancies [6], to high- T_c superconductors ($\text{YBa}_2\text{Cu}_3\text{O}_{7-x}$) [7], and from chemically inert (as we show here, H_2O only physisorbs on stoichiometric $\text{SrTiO}_3(110)-(4 \times 1)$) [8] to catalytically active (oxygen reduction reaction on $\text{La}_{1-x}\text{Sr}_x\text{MnO}_3$ solid oxide fuel cell cathode) [9]. Additionally, perovskites are known for exhibiting a high permittivity (SrTiO_3) [10], piezoelectricity ($\text{PbZr}_x\text{Ti}_{1-x}\text{O}_3$) [11], and ferroelectricity (BaTiO_3) [12].

The first task for a surface scientist is to prepare the surface of a given oxide crystal. Several approaches can be used to prepare nearly perfect surfaces. One of the best methods is cleavage in ultra-high vacuum (UHV). For example, the UHV cleavage of $\text{Sr}_3\text{Ru}_2\text{O}_7(001)$ results in almost perfect bulk-truncated surfaces with large terraces in the order of 1000 nm [13]. However, it was shown that cleavage can lead to emission of photons, electrons, atoms, and ions – obviously this

1. Introduction

method also often leads to non-ideal terminations of the bulk crystal structure [3]. Especially when attempting to prepare polar crystal faces, this method inevitably leads to non-optimal fracture [4]. A polar crystal face is an energetically unfavorable truncation of an ionic crystal. Such surfaces form if the crystal exhibits a net dipole moment in its repeat unit perpendicular to the surface. If not compensated in some way, the surface energy of such a truncated crystal diverges with its size. According to Tasker, such surfaces are called type-III polar surfaces [14].

A different approach to surface preparation is to cut the crystal parallel to the crystal face to be studied with subsequent polishing [3]. It is evident that cutting and polishing will cause harm to the crystal surface. Therefore, the crystals subsequently need to be heated to high temperatures (annealing) in UHV or in an oxygen environment to restore the crystal structure, and clean the surface from impurities created during cutting and polishing. Also with this method, one should not expect to get an ideal truncation of the bulk crystal structure and the preparation of polar surfaces remains again complex [4].

The third approach to be discussed here is the preparation of a surface by growing a thin film of the desired oxide material onto a suitable substrate. This method has to be applied if the oxide material of interest has a low electrical conductivity, or if it is not available in bulk form. The first point about the electrical conductivity is crucial, because most of the surface science analysis methods employ charged particles to probe the surface geometrical and electronic structure. Insulating bulk samples therefore become charged immediately and analysis is difficult. Thus, often thin films of these wide-bandgap materials are grown on suitable conducting substrates making them amenable for surface science analysis [15]. Alternatively, oxidation of a binary alloy can be used. For example, upon oxidation of a $\text{Pd}_3\text{Zr}(0001)$ alloy a trilayer ZrO_2 with a (111) surface is formed on top of the substrate alloy (band gap ≥ 5 eV) [16]. Of course, the quality of the oxide film is to a great extent dependent on the morphology and ordering of the substrate surface layer, and on the interaction of the oxide film with the substrate. This means, the substrate material and thin-film growth method have to be chosen wisely in order to obtain thin films of high quality.

1. Introduction

The second motivation for thin-film growth is the lack of bulk single-crystalline samples for some complex oxides. The only way to study surfaces of these materials is to grow a film of the corresponding oxide; if the thickness is sufficiently large (in the order of several monolayers), the film even exhibits bulk-like properties [17]. Typical physical vapor growth techniques applied are molecular beam epitaxy (MBE) or pulsed laser deposition (PLD). However, the growth of complex oxides is a difficult task for both techniques. In MBE, beside substrate temperature and background pressure, the fluxes of several evaporators have to be controlled precisely, while in PLD, all process parameters (UV laser fluence, temperature, and background pressure) need to be adjusted accurately. It should be mentioned that oxide PLD is rarely combined with surface analysis techniques. This is despite the fact that these techniques provide invaluable atomic-scale information concerning the prominent influence of surface and interface effects on both, growth phenomena and the resulting materials properties. Conversely, surface science needs model systems, where structure, stoichiometry, and defects are well controlled. This can, in principle, be provided by PLD heteroepitaxy for almost any kind of material. As complex multi-component oxides are at the heart of emerging applications in energy- and information-related research [18, 19], surface investigations of epitaxial films should be particularly promising in unraveling the molecular-scale surface processes that are central to device functionality. In the literature, only few groups report on combining PLD growth with *in-vacuo* scanning tunneling microscopy, *i.e.*, without breaking the vacuum. Both, homoepitaxial growth of $\text{SrTiO}_3(001)$ [20, 21] and heteroepitaxial growth of other perovskites [22–24] have been reported.

1.2. Strontium titanate

SrTiO_3 (STO) has evolved as a prototype for the perovskite materials for several reasons. Due to its very interesting and useful properties, STO attracts great interest in the scientific community. In addition to the fascinating semiconductor-to-superconductor transition of reduced crystals at low temperatures [25], Mavroides

1. Introduction

et al. observed a high water-splitting efficiency when using STO as the anode in photo-electrolysis [26]. Furthermore, it is widely used as a substrate for the growth of complex oxides because of a suitable lattice matching with other perovskites [27]. In addition to its technological benefits, STO is also a very practical material. It is available in single-crystalline form in suitable dimensions, and it crystallizes in the cubic perovskite structure and is therefore a very good model system for the class of perovskites.

SrTiO_3 is a semiconductor with a wide band-gap of around 3.2 eV [28]. A schematic energy-level diagram of SrTiO_3 is shown in Figure 1.2, reprinted from ref. [29]. The band structure is dominated by oxygen- and titanium-derived states. The highest occupied states, *i.e.*, the valence band, are mostly of O $2p$ character while the unoccupied conduction band states are of predominant Ti $3d$ character [30]. The valence- and conduction-characteristics of STO are therefore dominated by the TiO_6 complex of the STO unit cell. Because of the octahedral crystal field, the Ti $3d$ states experience a splitting into a subset of e_g and t_{2g} states, as observable in X-ray absorption spectroscopy of the Ti $L_{2,3}$ absorption edge (see section 3.4.3) [31]. STO is typically considered an ionic compound with formal charges of +4, +2, and -2 for the Ti, Sr, and O ions, respectively. However, covalency also plays an important role, because a fully ionic model of STO would exhibit a much larger bandgap [32]. STO can be turned into an n-type semiconductor by partially substituting Ti^{4+} with Nb^{5+} ions, or by creation of oxygen vacancies, *e.g.*, by reduction in UHV at high temperatures [6]. Doped crystals exhibit the Fermi level close to the conduction band minimum, as seen in ultra-violet photoelectron spectroscopy [33], and are well suited for surface science analysis techniques.

Figure 1.3 shows a SrTiO_3 crystal bulk-truncated at the (a) STO(100) and (b) STO(110) planes. Along [100] direction, STO is composed of an alternating stacking of formally charge-neutral planes of $(\text{SrO})^0$ and $(\text{TiO}_2)^0$. Cleaving a crystal parallel to the (100) plane therefore results in both, Sr- and Ti-terminated surfaces. Initially it was reported that STO does not cleave well supported by the presence of blurred spots in LEED after cleavage [29]. However, recent reports

1. Introduction

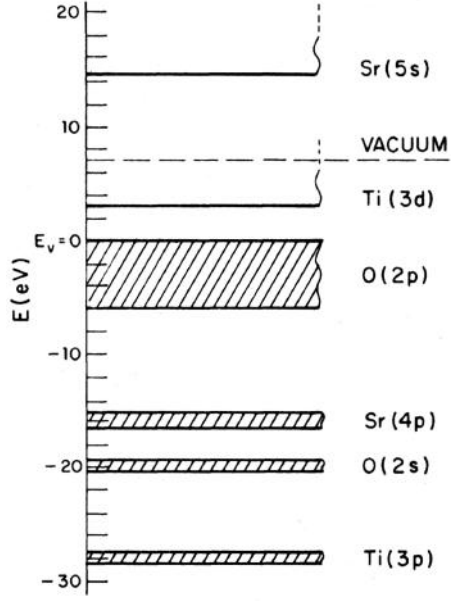


FIGURE 1.2.: Schematic energy-level diagram for SrTiO_3 . Figure reprinted with permission from ref. [29]. © 1978 American Physical Society.

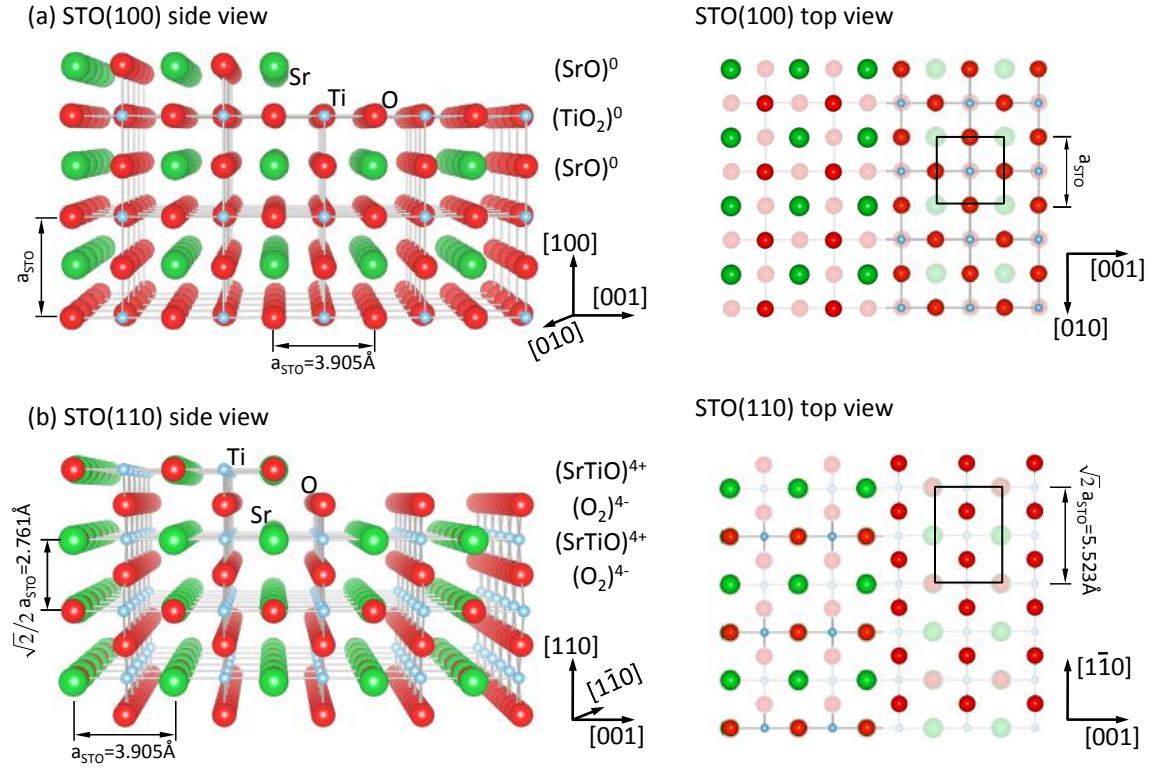


FIGURE 1.3.: Side and top view of (a) STO(100) and (b) STO(110) bulk-truncated surfaces.

1. Introduction

demonstrated the successful cleavage of STO crystals for surface science analysis, as seen in refs. [34–36].

STO crystals are typically cut and polished parallel to the surfaces to be studied. A widely accepted and commonly applied procedure for preparing STO(100) surfaces is to dip the polished samples into a buffered HF solution that dissolves all polishing residuals and terminal SrO layers, resulting in an exclusively TiO_2 -terminated surface [37]. However, it has been revealed recently that this method can lead to “unintentional F doping of SrTiO_3 ” [38]. Chambers *et al.* found approximately 13% of the terminal O anions to be replaced by F after HF treatment. They further suggest to only boil the STO samples in water instead to circumvent the F-doping. A subsequent annealing in oxygen in a tube furnace then yields flat and entirely TiO_2 -terminated surfaces.

Introduced into UHV, samples are either only annealed in oxygen environment at high temperatures (to ‘react away’ adsorbates) before analysis [39], or Ar^+ sputtered and annealed [40]. Due to different sputtering yields for the different constituents of the crystal, the surface inevitably becomes enriched with one of the species. On both, STO(100) and STO(110) surfaces, it has been reported that ion bombardment results in a Ti-enriched surface [29, 41]. Subsequent annealing of sputtered STO(100) surfaces does not necessarily restore the chemical composition of the bulk and often the resulting surfaces are reconstructed. In addition to the often reported (but not yet atomically resolved by STM) bulk-truncated STO(100)- (1×1) surface, numerous reconstructions have been observed, including (2×1) , (2×2) , $c(4 \times 2)$, $c(4 \times 4)$, (4×4) , $c(6 \times 2)$, $(\sqrt{5} \times \sqrt{5})\text{-R}26.6^\circ$, and $(\sqrt{13} \times \sqrt{13})\text{-R}33.7^\circ$. An overview of many reconstructions reported on STO(001) so far can be found in ref. [42]. In some cases, similar preparation conditions lead to different surface reconstructions indicating that the atomic control of the surface structure of STO(100) is rather complicated. The driving force behind the formation of reconstructions on STO(100) is not yet fully elucidated. It was proposed that one reason could be the undercoordinated nature of Ti ions in the bulk-truncated surface layer. Erdman and coworkers suggested in the case of the $c(4 \times 2)$ reconstruction that the formation of an overlayer is favorable as it replen-

1. Introduction

ishes the six-fold coordination of Ti in the surface layer [43]. Other interpretations suggest ordered oxygen vacancies [44, 45], or Sr adatoms [46, 47] to form the observed reconstructions.

STO(110) also shows a variety of reconstructions, but the underlying driving force seems to be more obvious than for the (100) surface. Along the [110] direction STO is composed of alternating charged layers of $(\text{SrTiO})^{4+}$ and $(\text{O}_2)^{4-}$, see Figure 1.3(b). This renders the STO(110) surface a Tasker type-III polar surface [14]. A macroscopic crystal with bulk-truncated surfaces would therefore bear a macroscopic dipole moment perpendicular to the surface. This so-called polar catastrophe can be balanced by introducing a surface layer that carries minus one half of the charge density of the preceding last bulk layer. This can be achieved in several ways, *e.g.*, by adsorption of charged species, by charge transfer to the surface, or by introduction of non-stoichiometry in the surface layer [48].

Polar compensation on STO(110) is obtained by reconstruction of the surface. Reconstructions are denoted as $(m \times l)$ with m and l being the periodicities along [001] and $[1\bar{1}0]$ directions, respectively. Several different structures haven been found on STO(110). Bando *et al.* observed (2×5) and $c(2 \times 6)$ structures [49], Brunen and Zegenhagen reported (2×5) , (3×4) , (4×4) , (4×7) , and (6×4) reconstructions [50], Russell *et al.* found $(n \times 1)$ ($n=3-6$) [51], and Wang *et al.* reported (2×8) and (6×8) structures. (The 8-fold periodicity along $[1\bar{1}0]$ reported by Wang and coworkers is referred to the reduced unit cell size of the bulk $(\text{O}_2)^{4-}$ layer, which measures half the size of the STO(110) unit cell along $[1\bar{1}0]$ direction [see Figure 1.3(b)] [40, 41]. Related to the full STO(110) unit cell, these structures exhibit a 4-fold periodicity along $[1\bar{1}0]$ direction and will be referred to as (2×4) and (6×4) throughout this thesis.) Wang and coworkers established a phase diagram that clearly shows that most of the surface structures on the STO(110) surface are connected through the near-surface stoichiometry, see Figure 1.4. They prepared a (6×1) reconstructed surface and monitored reflection high-energy electron diffraction (RHEED) patterns of the sample at 800 °C in 5×10^{-6} mbar O_2 while depositing Ti metal onto the surface. Fractional patterns of (5×1) and (4×1) reconstructions develop as the deposition dose increases, eventually result-

1. Introduction

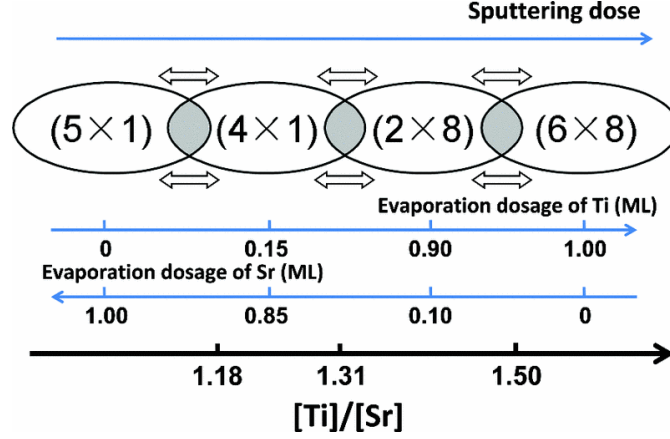


FIGURE 1.4.: Surface phase diagram of STO(110) surface. Deposition amounts are measured in monolayers (1 ML = 1 atom per STO(110) unit cell). Here, (2×8) and (6×8) structures are referred to the STO(110) bulk $(\text{O}_2)^{4-}$ layer. Referred to the full STO(110) unit cell, these structures are called (2×4) and (6×4) . This is the nomenclature adopted in the text. Figure reprinted with permission from ref. [41]. © 2011 American Physical Society.

ing in a (2×4) - and finally in a (6×4) -reconstructed surface [41, 52]. This change is reversible by deposition of Sr metal under the same conditions. Similarly, the surface structure can be tuned from (6×1) towards (6×4) by increasing the Ar^+ sputtering dose and subsequent annealing [40]. Their results are summarized in Figure 1.4 (reprinted from ref. [41]). The dependence of the surface reconstruction on the near-surface stoichiometry results in a straight-forward atomic-scale control of the surface structure.

2. Experimental techniques and setups

2.1. Photoemission spectroscopy (XPS and UPS)

Photoemission spectroscopy is a non-destructive experimental technique that allows probing the electronic structure of a solid, liquid, or gaseous material. Electrons from occupied states of the band structure or atomic core-levels (with binding energy E_B) are liberated into vacuum by absorption of a photon with sufficiently large energy ($h\nu$). The kinetic energy (E_{kin}) of the ejected electron traveling through vacuum and detected by an analyzer then equals

$$E_{kin} = h\nu - E_B - \Phi_A \quad (2.1)$$

with Φ_A being the work function of the analyzer, see Figure 2.1.

By analyzing the spectral distribution of the photoelectrons, *i.e.*, by measuring the intensity of photoelectrons versus their kinetic energy, one obtains a representation of the electronic structure of the material. Depending on the light used (X-rays or UV), the method is referred to as XPS or UPS. XPS and UPS allow studying the chemical and elemental composition of a material, and determining the chemical state of its constituents. Figure 2.2 shows an example of an overview spectrum of SrTiO_3 with the main features labeled. By varying the kinetic energy of the photoelectrons, or the angle of emission, this method can also be used for probing the near-surface region or for depth profiling (*cf.* universal curve from ref. [53]).

In addition, UPS data provide valuable information on the adsorption of water on surfaces. While molecularly adsorbed water is characterized by a three-peak

2. Experimental techniques and setups

feature with molecular states of H_2O at ~ 8 eV ($1b_2$), ~ 12 eV ($3a_1$), and ~ 14 eV ($1b_1$), hydroxyls only exhibit two peaks in this binding energy region, *i.e.*, OH 3σ (~ 11 eV) and OH 1π (~ 6 eV) [54]. Ultra violet photoemission spectroscopy has been carried out at the Maxlab synchrotron facility at beamline I311. The beamline is equipped with an undulator and monochromator that allows to choose the photon energy from 43 to 1500 eV, and a SCIENTA SES200 energy-analyzer. Due to a lack of accurate photon energy calibration for the synchrotron-based experiments, the absolute binding energy values of photoemission features are not fully reliable. A spread of up to 0.3 eV has been observed in the spectra, making conclusions on band bending less strong.

In Section 3.6.2, we present *in-situ* XPS-derived Sr $3d$ over Ti $2p$ intensity ratios. These ratios were computed by integrating the spectrum in the region of the core-levels after subtraction of a Shirley background. The inelastic mean free path of the photoelectrons originating from Ti $2p$ or Sr $3d$ core-levels excited by Al $K\alpha$ radiation and traveling through SrTiO_3 is on the order of 2.5 nm, corresponding to about 9 ML [55].

In the lab at TU Wien, photoelectrons were acquired with normal emission. At the Maxlab synchrotron facility, photoelectrons were acquired under a grazing exit of 55° with respect to the sample surface normal, which increases the surface sensitivity of the measurements.

2.2. X-ray absorption spectroscopy (XAS)

In X-ray absorption spectroscopy (XAS), electrons from core levels are excited into unoccupied states by absorption of a photon with a suitable energy. An abrupt rise of the absorption is observed when the photon energy exceeds the binding energy of an electron. The probability for absorption is determined by the density of final states combined with the selection rules for dipole transitions. Since the binding energies of the electrons are characteristic for different atoms or ions, XAS allows for probing the local density of empty states of the elements separately. Because the probed empty states are within several eV above the absorption edge,

2. Experimental techniques and setups

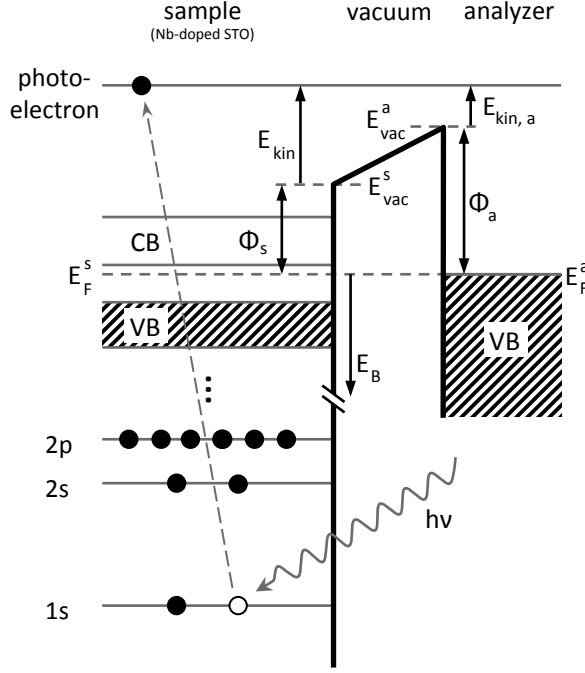


FIGURE 2.1.: Schematic representation of the photoemission process for an arbitrary sample. Abbreviations: E_F , E_B , E_{kin} , E_{vac} , Φ , VB, and CB stand for Fermi-, binding-, kinetic-, and vacuum-energy, workfunction, valence band, and conduction band, respectively.

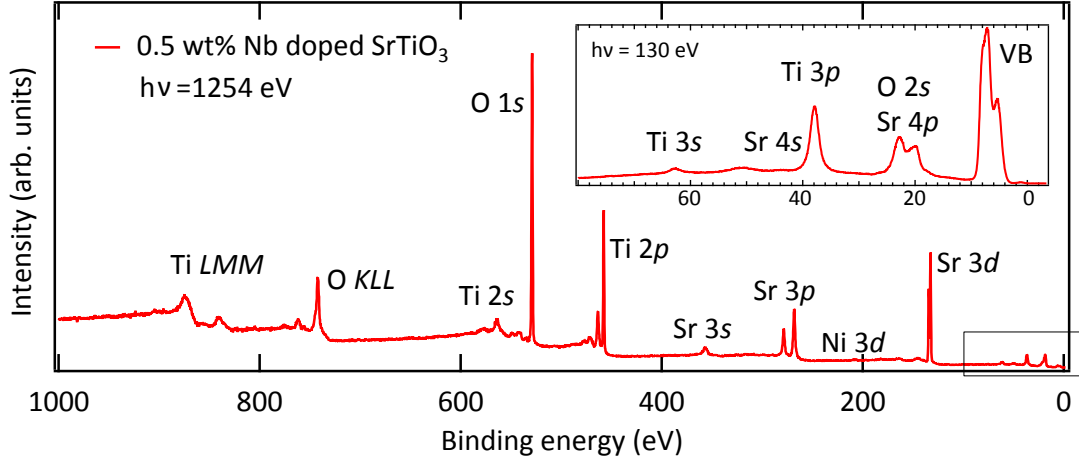


FIGURE 2.2.: XPS and UPS spectra of SrTiO_3 with photoemission and Auger peaks labeled.

2. Experimental techniques and setups

this techniques is also referred to as near edge X-ray absorption fine structure (NEXAFS), or X-ray absorption near-edge structure (XANES). The transition of electrons from core-levels into unoccupied states is associated by the formation of core-holes. These core-holes are then filled by higher-lying electrons, typically resulting in the emission of Auger electrons and secondary electrons.

In Auger-electron yield mode (AEY), an Auger electron associated with the initial core-hole is measured while sweeping the photon energy across the absorption edge. For the Ti $L_{2,3}$ edge, the Ti LMM Auger electron with a kinetic energy of ~ 390 eV was measured. For the O K edge, the O KLL Auger electron ($E_{\text{kin}} = 470$ eV) was measured. According to the universal curve [53], the inelastic mean free path of these electrons traveling through a solid is on the order of 1-10 Å, rendering this acquisition mode very surface sensitive.

In secondary-electron-yield mode (SEY), electrons with a kinetic energy of ~ 60 eV were acquired as an indication of the absorption of X-rays. Since there is no distinct peak in the photoemission spectrum at these kinetic energies, the signal consists of electrons that have lost energy in multiple scattering events. This results in a larger information depth for the SEY mode as compared to the AEY mode. In the total electron yield mode (TEY), the sample drain current is measured, *i.e.*, all secondary electrons that are able to leave the sample are measured. This renders the TEY mode the most bulk-sensitive mode.

The probed unoccupied states are sensitive to the local chemical environment of the ions. In SrTiO_3 , the unoccupied states close to the Fermi level are mainly of Ti $3d$ character (see Figure 1.2 in chapter 1.2). As illustrated in Figure 2.3, in an octahedral, or tetrahedral crystal field the Ti $3d$ states undergo a splitting into a subset of t_{2g} and e_g , or e and t states, respectively. The STO(110) ($n \times 1$) surface structure consists of a network of TiO_4 tetrahedra residing on planes of bulk STO where Ti is in octahedral coordination, see Section 1.2. Depending on the acquisition mode (AEY or SEY), the resulting spectrum of the Ti $L_{2,3}$ absorption edge exhibits more or less information of the surface TiO_4 tetrahedra, as can be seen in Figure 3.7. In section 3.1.1 Ti $L_{2,3}$ absorption edge spectra were simulated using the CTM4XAS code developed by de Groot and coworkers [56].

2. Experimental techniques and setups

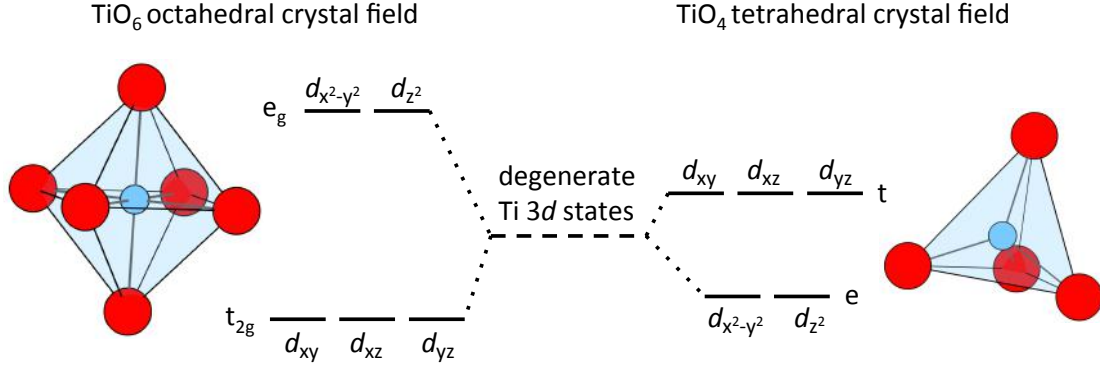


FIGURE 2.3.: Ti 3d states split into a subset of t_{2g} and e_g states in an octahedral crystal field (left). Similarly but reversed, these states split into a subset of e and t states in a tetrahedral crystal field (right). Ti and oxygen atoms are shown in blue and red, respectively.

2.3. Low-energy He-ion scattering spectroscopy (LEIS)

LEIS is an experimental technique to probe the surface elemental composition. He^+ ions are accelerated to 1 keV kinetic energy and directed onto the sample. Elastically backscattered ions are detected by the hemispherical energy analyzer, see Figure 2.4(a). Combining momentum and energy conservation, the energy of the backscattered He^+ ions (E_1) can be expressed in terms of the primary He^+ ion energy (E_0), the masses of the primary ion (m_{He}) and the surface scattering site (m_s), and the scattering angle (θ) [57]:

$$E_1 = E_0 \left(\frac{m_{\text{He}} \cos \theta \pm \sqrt{m_s^2 - m_{\text{He}}^2 \sin^2 \theta}}{m_{\text{He}} + m_s} \right)^2 \quad (2.2)$$

By measuring the kinetic-energy spectrum of the elastically scattered ions in a fixed geometry, the masses of the sample surface scattering atoms can be derived. By using He^+ as the primary ion, the resolution of this method allows for distinguishing different isotopes of oxygen (*e.g.*, ^{18}O and ^{16}O) on the surface. Because of a high probability for neutralization, this method is highly surface sensitive. LEIS peaks have been fitted with a Gaussian function after subtraction of a linear

2. Experimental techniques and setups

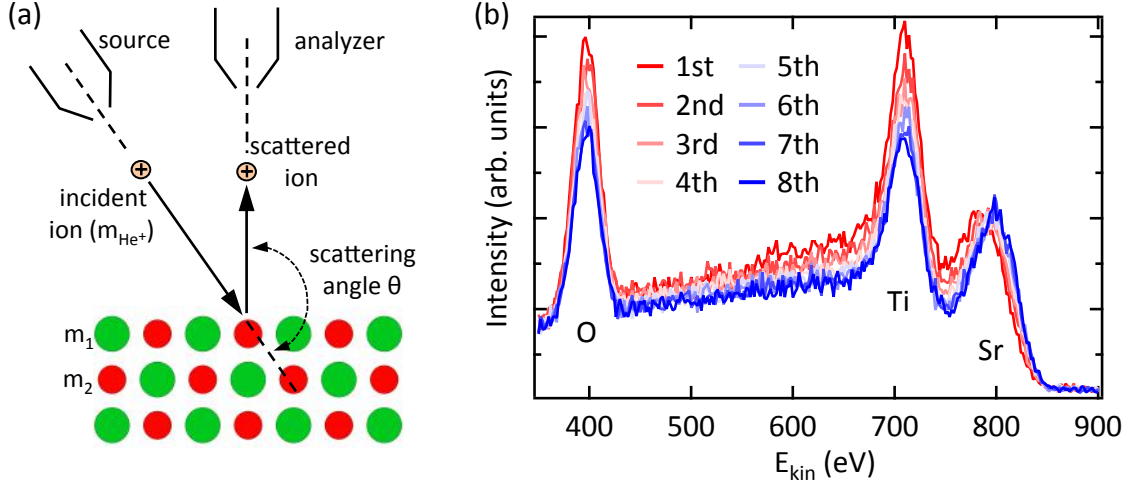


FIGURE 2.4.: (a) Schematic view of low-energy ion scattering spectroscopy. (b) Consecutively acquired ion scattering spectra of an $\text{SrTiO}_3(110)-(4 \times 1)$ sample. (Each scan takes about 1 min; total ion fluence of $\sim 1.5 \times 10^{14}$ ions/cm² for each spectrum).

background.

It should be mentioned that 1000 eV He^+ ions impinging on the surface progressively damage the surface, most likely due to intermixing of the first few surface layers. In particular, a considerable change of the apparent Ti to Sr ratio is visible already after 8 scans, see Figure 2.4(b). (Each scan takes about 1 min; the ion currents ranged from 15 to 23 nA, which corresponds to a total ion fluence of $\sim 1.5 \times 10^{14}$ ions/cm² for each spectrum). In order to limit beam damage as much as possible while still retaining good statistics, we used only the sum of the first four scans for each LEIS spectrum presented in the results section 3.4.4. In addition, the Sr-related peak in LEIS spectra exhibits a shift to higher kinetic energies with progressing beam damage, see Fig. 2.4(b). Probably this is related to the low Sr-content of the pristine (4×1) surface. The Sr peak in the first few spectra probably originates from ions scattered at subsurface Sr atoms and inelastic losses could lead to such a peak shift.

2.4. Scanning tunneling microscopy (STM)

Since its invention by Binnig and Rohrer [58], the scanning tunneling microscope has become an indispensable analysis technique in surface science. It is one of the few techniques that allows investigation of (semi-) conducting sample surfaces with atomic precision in real space. Its working principle is based on the quantum mechanical tunnel effect that enables electrons to tunnel through a vacuum barrier. Considering a conducting tip in close proximity of a sample surface, the wave-function $[\Psi(z)]$ of electrons outside of the tip can be described by the 1D time-independent Schrödinger equation:

$$\left(\frac{-\hbar^2}{2m} \Delta + U(z) \right) \Psi(z) = E \Psi(z), \quad (2.3)$$

with m , \hbar , U , and E being the electrons mass, the reduced Planck constant, the height of the vacuum barrier, and the kinetic energy of the electron, respectively. The solution of this equation inside the vacuum barrier is an exponentially decreasing function of the form

$$\Psi(z) \propto \exp(-z \kappa), \text{ with } \kappa = \sqrt{\frac{2m\Phi}{\hbar^2}}, \quad (2.4)$$

and Φ is proportional to the vacuum barrier. The tunneling current (I_t), which is proportional to the probability of the electrons tunneling through the barrier of width d then equals:

$$I_t \propto |\Psi(d)|^2 \propto \exp(-2 d \kappa) \quad (2.5)$$

Equation 2.5 shows that the tunneling current depends exponentially on the distance between the tip and the sample. Small changes in the distance therefore result in big changes in the tunneling current, which is the basic principle allowing atomic-scale imaging of surfaces by STM. By applying a bias voltage to the sample with respect to the tip [see Figure 2.5(b)], electrons either tunnel from occupied states of the tip into unoccupied states of the sample (positive bias), or *vice versa* (negative bias). It is therefore evident that the local density of states of the sample surface atoms will also modulate the tunneling current. In practice,

2. Experimental techniques and setups

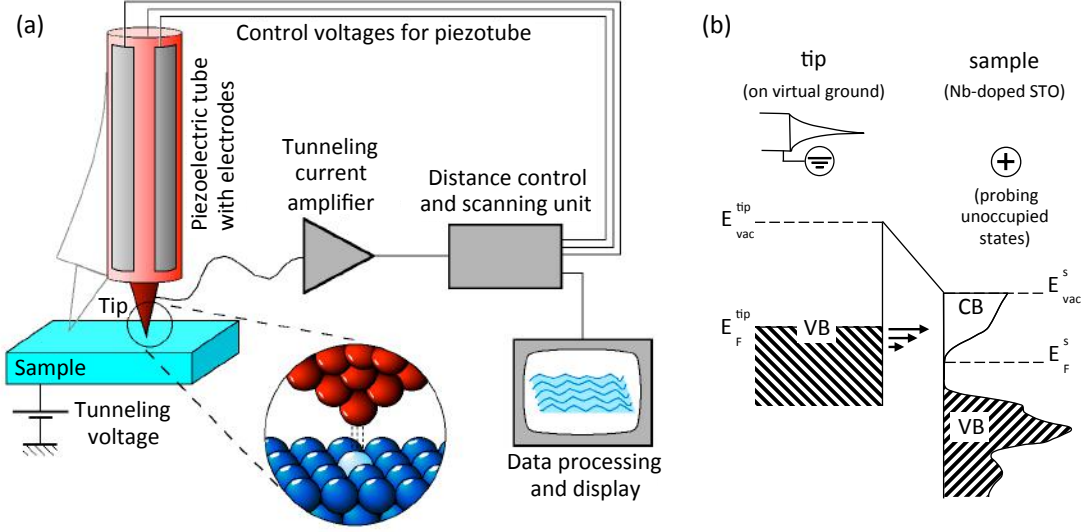


FIGURE 2.5.: (a) Schematic view of a scanning tunneling microscope (reprinted from ref. [60]). (b) Schematic representation of the energy bands of the tip in tunneling contact with the sample at positive bias (probing unoccupied states).

an electrochemically etched W tip is mounted on a piezoelectric scanner and is approached to the sample surface. When a tunnel contact is established, the tip is scanned across the surface and the z -position of the tip (constant current mode) is measured for each step (pixel). The resulting image is a convolution of the surface electronic and geometric structure. Often, the contrast in the STM images reflects the actual geometric structure of the surface, but a contrast inversion might occur due to electronic effects, *e.g.*, for $\text{TiO}_2(110)-(1 \times 1)$ [59]. All STM images presented here show filled-states images (positive bias).

2.5. Low-energy electron diffraction (LEED)

LEED is a non-destructive technique to probe the structure of a crystalline surface in reciprocal space. Electrons with a kinetic energy of around 100 eV are directed onto a conducting surface under normal incidence. This kinetic-energy range results in a short inelastic mean free path and renders LEED a surface sen-

2. *Experimental techniques and setups*

sitive technique. The electron beam is focused onto a crystalline sample surface, at which all surface atoms act as scattering sites. The electron wave is elastically back-scattered, which results in a diffraction pattern on the phosphor screen. The pattern is a representation of the crystal structure in reciprocal space and is commonly used to identify the symmetry and periodicities of a reconstructed surface.

2.6. Pulsed laser deposition (PLD)

Oxide thin films are typically grown by physical vapor deposition techniques, such as molecular beam epitaxy (MBE), or pulsed laser deposition (PLD). Among these techniques, PLD is probably the most versatile approach to thin film growth. In PLD, a pulsed ultra-violet (UV) laser is focused onto a target material inside a vacuum chamber. Above a certain threshold energy density, material is vaporized and forms a plasma, which expands away from the UV laser spot resulting in the so-called plasma plume. The plume moves towards the substrate and condenses as a thin film on the substrate surface (see Figure 2.10). Because PLD is a non-thermal technique, the energy of the ablated species is on the order of 10 to 100 eV per particle (compared to around 0.1 eV in MBE), and can be moderated by interaction with an ambient gas in the system. In addition to the typical growth parameters such as substrate temperature, gas pressure, and deposition rate, the energy of the deposited species can be varied, which is a unique parameter in non-thermal evaporation techniques [61]. Furthermore, the pulsed nature of PLD results in a growth regime dominated by a high instantaneous flux, which favors layer-by-layer growth over island growth, followed by a relatively long period with only surface diffusion and nucleation [62]. Although PLD has been reported to readily produce high-quality thin films, it was shown that only a precise control of the growth parameters (mainly UV laser fluence and deposition pressure) leads to stoichiometric transfer of material from the target to the substrate [63].

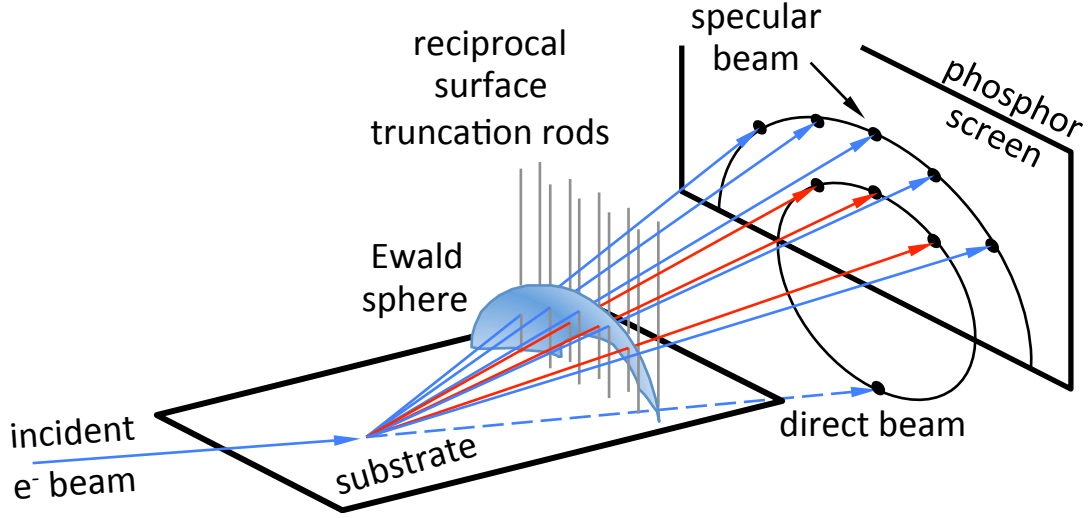


FIGURE 2.6.: Schematic view of RHEED, reprinted from ref. [64].

2.7. Reflection high-energy electron diffraction (RHEED)

In RHEED, a high-energy electron beam (in the order of 10–50 keV) is directed onto a sample surface under grazing incidence of a few degrees. A crystalline sample will cause the electron beam to diffract and produce a pattern on a screen positioned around the specular reflection of the diffracted beam. The grazing incidence geometry provides the advantage of simultaneous thin-film growth and RHEED analysis.

The formation of a RHEED pattern is typically illustrated in reciprocal space as an elastic scattering event. The incident and the scattered wave vectors therefore lie on a sphere called the Ewald sphere. Intersection of this sphere with the surface truncation rods of the sample surface determines the scattering geometries where the Bragg condition is fulfilled. These reflections are made apparent on the phosphor screen (see Figure 2.6).

By adjusting the tilt of the sample with respect to the incident electron beam, the intensity of the specular RHEED spot was maximized. This geometry is called

2. Experimental techniques and setups

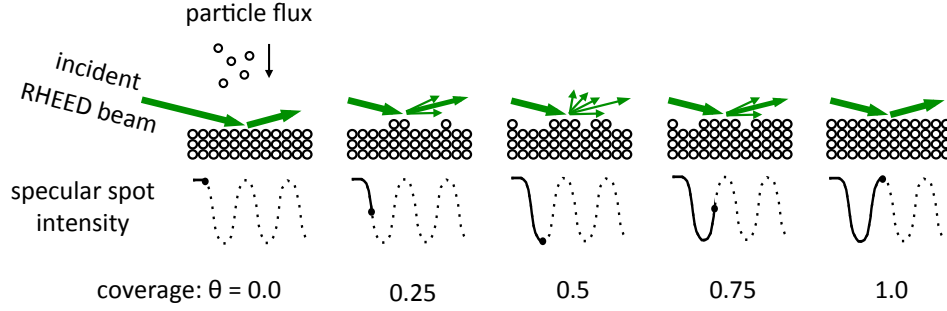


FIGURE 2.7.: Schematic illustration of oscillations in the RHEED specular spot intensity corresponding to layer-by-layer growth mode.

the in-phase condition where neighboring terraces constructively interfere. In this RHEED geometry, the highest intensity of the specular spot can be expected for an infinitely large surface. The introduction of surface steps results in a decrease of the specular spot intensity due to the formation of diffuse scattering sites [65]. Monitoring the intensity of the specular RHEED spot during growth therefore provides information on the growth behavior of the surface; an ideal layer-by-layer growth results in oscillations of the RHEED intensity, see Figure 2.7.

2.8. X-ray diffraction (XRD)

X-ray diffraction (XRD) is a method to probe the crystal structure of a sample. X-rays impinging on a crystalline sample can be elastically scattered. Constructive interference only occurs if the Bragg condition is fulfilled:

$$n \lambda = 2 d \sin(\theta) \quad (2.6)$$

With n indicating the diffraction order, λ is the wavelength of the incoming X-rays, d is the interlayer spacing, and θ being the angle of incidence with respect to the sample surface. In this thesis the X-ray diffraction experiments were performed with a parallel-beam setup in a θ - θ geometry, where the source and the detector are rotated towards each other by the same amount in each step. The resulting scans are of the form intensity versus 2θ . XRD results presented in Section 3.6.7 show the (330) Bragg reflection using Cu $K\alpha$ radiation. We applied XRD on

2. Experimental techniques and setups

homoepitaxially grown thin films on STO(110). We were interested in the relative position of Bragg peaks, as this could indicate an expanded lattice of the film with respect to the substrate.

2.9. SPECS setup

The main experimental setup used was the so-called SPECS setup, see Figure 2.8 for a schematic view. The system consists of a preparation chamber equipped with Ar^+ sputtering, electron beam annealing, leak valves for gas dosing, metal evaporators, and a load lock. Ti metal has been deposited from an electron-beam evaporator (EFM 3, FOCUS GmbH) and Sr metal has been deposited from a low-temperature effusion cell at 420 °C (LTC-40-10-284-WK-SHM, CreaTec Fischer & Co. GmbH). The flux was calibrated via a home-built quartz crystal microbalance (QCM) operating at elevated temperature ($\sim 90\text{--}100$ °C). The base pressure of the preparation chamber was below 4×10^{-10} mbar. The analysis chamber is equipped with low-energy electron diffraction (LEED; Omicron SpectraLEED), X-ray photoemission spectroscopy, low-energy ion scattering spectroscopy (LEIS; SPECS IQE 12/38 ion source with Wien filter; scattering angle $\sim 127^\circ$), residual gas analysis (RGA; SRS100), and a SPECS Aarhus 150 STM operated at room temperature. XPS was obtained mainly from a commercial XPS setup using an X-ray source (Omicron DAR400) with dual anode to produce Al and Mg K_α radiation (300 W, 15 keV; $h\nu_{K\alpha_1}^{\text{Al}} = 1486.7$ eV, $h\nu_{K\alpha_1}^{\text{Mg}} = 1253.7$ eV [66]), and a hemispherical energy analyzer (HSA; SPECS Phoibos100) with 5-channel detector (sample current 120 nA). Photoelectrons were detected in normal emission. The base pressure of the analysis chamber was below 1×10^{-10} mbar. Samples were transferred between the chambers using magnetically coupled transfer rods and gases were introduced to the chambers through high-precision leak valves. In the SPECS setup, samples were annealed by electron beam heating (900 V, 15 mA, ~ 1000 °C) and the temperature was monitored by an infra-red (IR) pyrometer. Water (H_2^{16}O and H_2^{18}O) has been cleaned by several freeze-pump-thaw cycles, and has been dosed through high precision leak vales.

2. Experimental techniques and setups

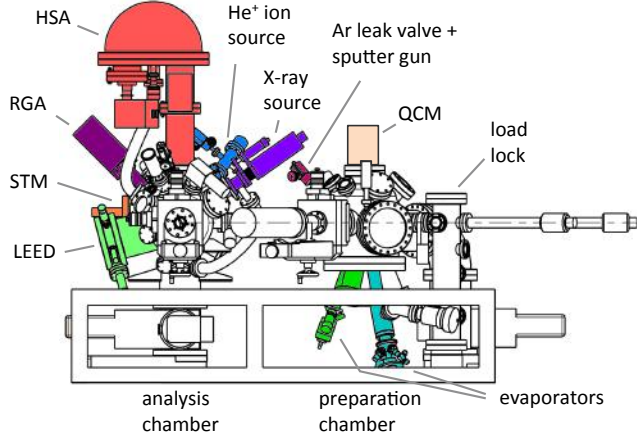


FIGURE 2.8.: Schematic view of the SPECS setup highlighting the sample preparation and analysis techniques. Adapted from a technical drawing by SPECS GmbH.

2.10. Pulsed laser deposition (PLD): Chamber and Procedures

The surface analysis system was expanded with a pulsed laser deposition (PLD) chamber in the years 2014–2015. The PLD system combines pulsed laser deposition with *in-vacuo* growth analysis by RHEED. Figure 2.9 shows a photograph of the new experimental apparatus built by Twente Solid State Technology B.V. with the basic components highlighted. The PLD chamber with a base pressure after bake-out of around 4×10^{-10} mbar is connected via a transfer chamber (base pressure below 1×10^{-10} mbar) to the surface analysis system described above. The transfer chamber also hosts a sample storage system. The setup allows for rapid (~ 30 s) *in-vacuo* transfer of samples from the PLD chamber to the surface analysis chamber.

Figure 2.10 shows a schematic of the PLD process with *in-situ* RHEED analysis and the different connected UHV chambers. Pulsed UV laser light (Coherent COMPexPro 205F; wavelength 248 nm, pulse duration 20–50 ns, pulse-to-pulse standard deviation of the beam energy better than 0.6 %) is passing through an attenuator module (Coherent MicroLas), which allows setting of the UV pulse energy. A mask is placed in the central part of the beam to cut out the inhomogeneous part of the beam profile and the distance between mask and UV focusing lens is optimized for a certain demagnification of the UV beam (by a factor of ~ 10).

2. Experimental techniques and setups

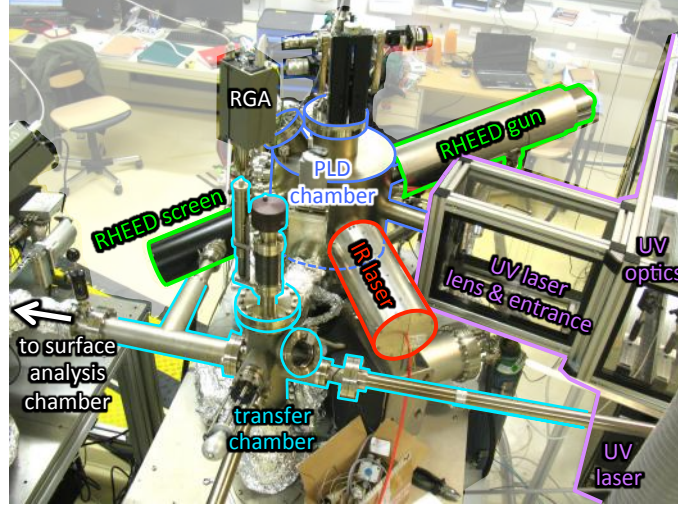


FIGURE 2.9.: Photograph of the PLD chamber with the RHEED gun and phosphor screen (green), the IR laser heating (red), and the UV optics and lens system (purple) highlighted.

Single-crystalline Nb-doped SrTiO_3 has been used as a target for the homoepitaxial growth studies (see section 3.5 and 3.6 below). The target-to-substrate distance is fixed to about 60 mm. In the PLD chamber, samples were annealed by shining an IR laser (DILAS compact evolution; wavelength 980 nm, 50 W $\hat{=}$ 1000 °C) through the hole in the sample plate onto the backside of the sample. The temperature was monitored by an IR pyrometer.

The PLD chamber is equipped with a differentially pumped RHEED system from Staib Instruments GmbH (TorrRHEEDTM) that allows monitoring RHEED oscillations in up to 1 mbar oxygen pressure. The RHEED pattern and the intensity of the specular spot are recorded from a phosphorous screen with a kSA400 acquisition system (camera integration time 16 ms).

Surface-science measurements impose stringent requirements of chemical purity to all involved processes in sample preparation. We therefore improved the typical sample mounting by Ag paint, and UV spot size determination with thermal paper to be compatible with the purity requirements of ultra-high vacuum surface science. Samples were mounted by spot-welding clips onto the sample holder (see below). For a clean, UHV compatible way of determining the size and shape of the

2. Experimental techniques and setups

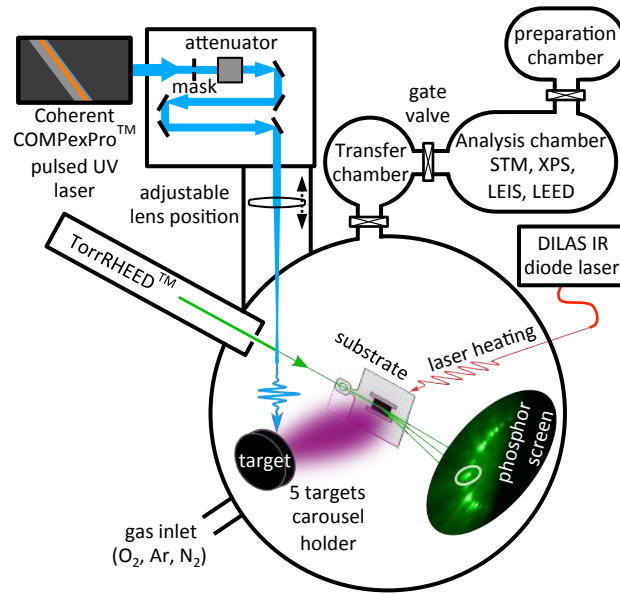


FIGURE 2.10.: (a) Schematic view of the pulsed laser deposition process with *in situ* RHEED analysis and the connected UHV chambers. Pulsed ultra-violet laser, continuous infra-red laser, RHEED beam, and plasma plume are highlighted in pale blue, red, green, and purple, respectively.

2. Experimental techniques and setups

UV laser spot, the laser was directed onto a polished, polycrystalline Cu target inside vacuum. The spot size was measured outside of vacuum via an optical microscope (see Appendix Section A.1 for details). For the experiments presented in Section 3.5 and in Section 3.6, the spot-size was set to $1.05 \times 2.35 \text{ mm}^2 = 2.47 \text{ mm}^2$ or $0.67 \times 1.53 \text{ mm}^2 = 1.03 \text{ mm}^2$. In addition, heating the substrate by an IR laser ensures that only the substrate and the sample plate is heated to high temperatures, again keeping contaminations through outgassing at a minimum. These consideration of purity are found to be good ways to combine the usually disparate approaches of PLD growth and surface analysis.

A typical deposition was performed as follows:

- First, the target and the substrate were centered within the red pilot laser of the heating laser, and the UV laser was focused onto the center of the Cu alignment target (see Appendix Section A.2 for details).
- The pulse energy of the UV laser was adjusted to obtain the required fluence; the deposition pressure was set in the chamber.
- The target was pre-ablated with ~ 150 laser shots to remove all unwanted adsorbates and residues from grinding. Initially we kept the substrate in front of the target with the shutter in closed position (covering the substrate from the pre-ablation). After we found out that this geometry leads to some deposition onto the substrate during pre-ablation, we kept the substrate in the transfer chamber during pre-ablation.
- After the substrate was heated to the deposition temperature (ramp rate 1 K/s), the RHEED beam was aligned with the substrate.
- After this, the deposition took place while the variations of the RHEED intensity were recorded.
- The substrate was then kept at deposition temperature for 10 min before cool-down (1 K/s), pumping of the chamber, and transferring of the substrate to the surface analysis chamber.

2.11. Strontium titanate samples

Single-crystalline SrTiO_3 samples, cut and polished parallel to the (110) surface, have been purchased from commercial crystal vendors MaTecK GmbH and CrysTec GmbH. The specifications submitted to the crystal vendors are shown in Table 2.1. Due to the Nb doping, the crystals appear black and exhibit a Hall carrier concentration of $\sim 1.4 \times 10^{20}$ per cm^3 , as measured with a Van der Pauw setup. The resulting conductivity is sufficient for surface analysis and for sample heating. The applicability of IR laser heating has been confirmed by estimating the absorption of IR light in Nb-doped STO. Taking into account the refractive index ($n_{\text{STO}} \approx 2.32$) [67] and the optical conductance ($\sigma_c^{\text{STO}} \approx 300$) [68] of 0.5 wt% Nb-doped STO, it is estimated that the intensity of IR light with a wavelength of 980 nm drops to $1/e$ after penetrating less than 0.05 mm.

SrTiO ₃ (110) sample specifications	
Orientation	(110)
Tolerance surface vicinal angle	< 0.3 °
Edges parallel to	[001] and [$\bar{1}\bar{1}0$]
Niobium content	0.5 wt %
Dimensions	$5 \times 5 \times 0.5 \text{ mm}^3$

TABLE 2.1.: Specifications of SrTiO_3 sample orientation, miscut, doping, and size, as submitted to the crystal producers.

Sample mounting

Ultra-high vacuum (UHV), *i.e.*, $p < 10^{-9}$ mbar, is the key to surface science and all experiments have been performed in different UHV chambers. In order to manipulate and move the single-crystals in UHV, the samples have been mounted onto sample holders of Omicron design with spot-welded clips, see Figure 2.11. The clips are shaped in order to apply a spring force onto the sample after spot-welding them onto the sample plates. The sample plates were machined with a pocket to fit the sample and have a through hole for direct heating with an electron beam or with

2. Experimental techniques and setups

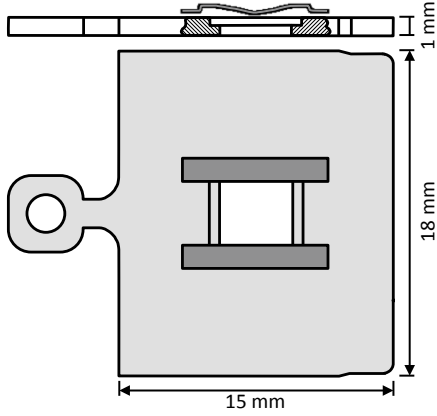


FIGURE 2.11.: SPECS sample holder design with pocket and through-hole, and spot-welded clips for sample mounting.

an IR laser. For the low oxygen partial pressure experiments ($p_{\text{O}_2} < 10^{-5}$ mbar), sample holders from Ta or Mo with clips made from Ta have been used. Ta and Mo provide good stability against high temperatures and the clips maintain the spring force on the sample after annealing multiple times to 1000 °C. For high- p_{O_2} pulsed laser deposition experiments ($p_{\text{O}_2} > 10^{-5}$ mbar) the samples were mounted onto sample holders made from a Ni-Cr-Fe, high oxidation resistant alloy (NiCroFerTM, NCF). The oxidation resistance of NCF has been tested successfully by annealing an STO sample mounted onto a NCF sample holder to 1000 °C in 50 mbar O₂ pressure. In contrast to Ta or Mo, NCF does not degrade in a highly oxidizing environment. However, compared to Ta or Mo it does not maintain the spring force of the clips when heated multiple times to high temperatures and samples can become loose.

Sample preparation

Samples were prepared by cycles of sputtering (Ar⁺, 1 keV, $\sim 5 \mu\text{A}$, 10 min) and annealing (1000 °C, 3×10^{-6} mbar O₂). After annealing, the oxygen inlet was closed after the sample was cooled down ($\sim 1\text{--}5$ K/sec) to about 300 °C. Two to three sputter/anneal cycles were typically used for new samples. The resulting surface exhibited predominantly the (4×1) reconstruction. Adjustment of the surface reconstruction was done by deposition of Ti or Sr metal in UHV at RT, and subsequent annealing at 1000 °C in 3×10^{-6} mbar O₂ [52]. Adsorbed Ni or NiO clusters were removed by one or two sputter/anneal cycles.

3. Results

3.1. $\text{SrTiO}_3(110)$ surface reconstructions

As already mentioned in the introduction, the $\text{STO}(110)$ surface shows a variety of surface reconstructions. Wang and coworkers revealed the driving force behind the formation of a series of reconstructions on this surface. By systematically altering the near-surface stoichiometry of $\text{STO}(110)$ single crystals through evaporation of Ti metal at elevated temperatures, they found the surface to gradually evolve from the initial (6×1) reconstructed surface via the (5×1) -, and the (4×1) -, to the (2×4) -reconstructed surface. This process was fully reversible by depositing Sr metal in similar conditions. STM images and corresponding RHEED patterns published in the study by Wang *et al.* are shown in Figure 3.1, reprinted from ref. [52]. This study exemplifies that the near-surface stoichiometry determines the formation of reconstructions on the $\text{STO}(110)$ surface. This behavior is advantageous to the experimentalist, as it provides a straight-forward procedure for surface preparation. Figure 3.2 shows the $\text{STO}(110)$ surface phase diagram reproduced at the lab at TU Wien. The upper panels show STM images ($13.7 \times 13.7 \text{ nm}^2$) of the different surface reconstructions. The lower panels show the corresponding LEED patterns (90 eV).

3.1.1. $\text{SrTiO}_3(110)$ -(4×1) surface reconstruction

(4×1) structure model

The homologous series of $(n \times 1)$ ($n=3-6$) structures has been solved recently. By combining transmission electron diffraction techniques with density functional

3. Results

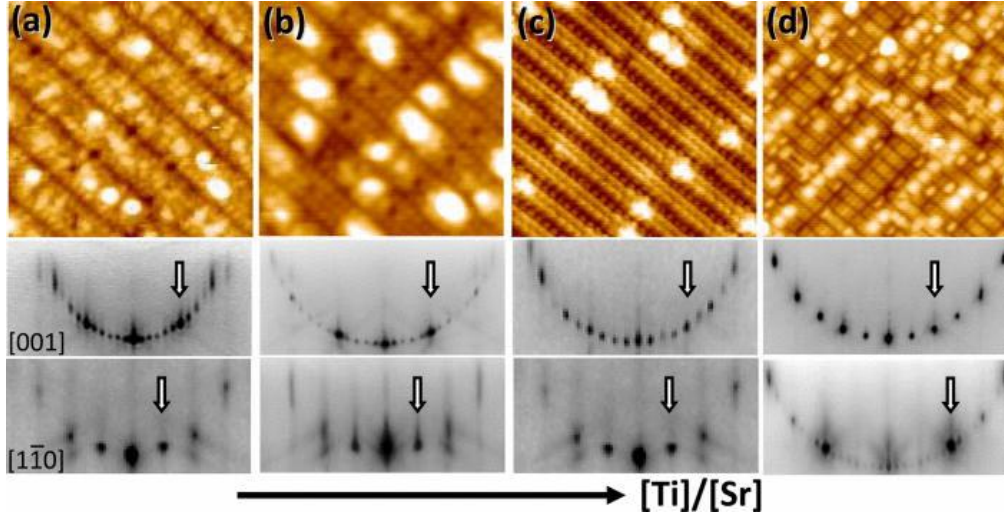


FIGURE 3.1.: Phase diagram of the STO(110) surface showing STM images (upper panels; image size $\sim 14 \times 14 \text{ nm}^2$) and corresponding RHEED patterns (lower panels) of the (a) (6×1) , (b) (5×1) , (c) (4×1) , and (d) (2×4) reconstructed surface. The near-surface cation ratio (Ti/Sr) is increasing from left to right. Reprinted with permission from ref. [52]. © 2012 American Institute of Physics.

theory, Enterkin *et al.* were able to identify the surface structure and building block of the $(n \times 1)$ series [69]. The structure consists of a network of six- and ten-member rings of corner-sharing TiO_4 tetrahedra residing on a bulk-like $(\text{SrTiO})^{4+}$ plane. The tetrahedra share oxygen corners within the plane of the reconstruction, and are connected to the bulk $(\text{SrTiO})^{4+}$ plane by sharing either corners or edges (see Figure 3.3). By increasing the number of tetrahedra in the six-member ring, the structure can be changed into the (5×1) and the (6×1) reconstruction [70]. The stoichiometry per (1×1) unit cell of this homologous series yields $\text{Ti}_{(n+2)/n}\text{O}_{(3n+4)/n}^{2-}$ and therefore compensates the polarity of the STO(110) surface perfectly for $n = 4$.

Characterization of the (4×1) reconstruction

Samples introduced into the UHV have been cleaned and prepared by several sputtering and annealing cycles. The resulting surface typically exhibited predominantly the (4×1) reconstruction with a small fraction of the surface exhibit-

3. Results

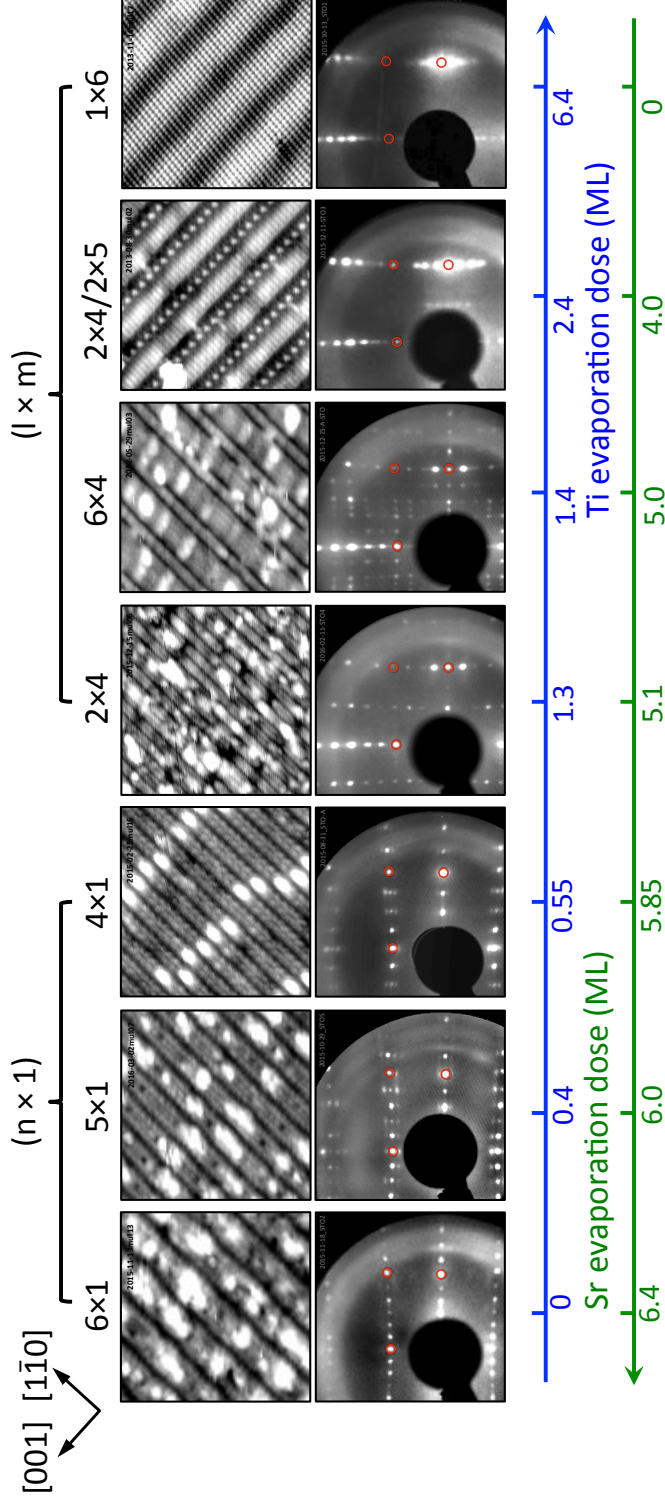


FIGURE 3.2.: The STO(110) surface phase diagram as reproduced at the lab at TU Wien. The upper panels shows STM images ($13.7 \times 13.7 \text{ nm}^2$) of the different surface reconstructions. The lower panels show the corresponding LEED patterns (90 eV; bulk-derived spots highlighted in red). The deposition amounts are adjusted on the basis of the phase diagram of Wang *et al.* [52]. Adapted from ref. [31].

3. Results

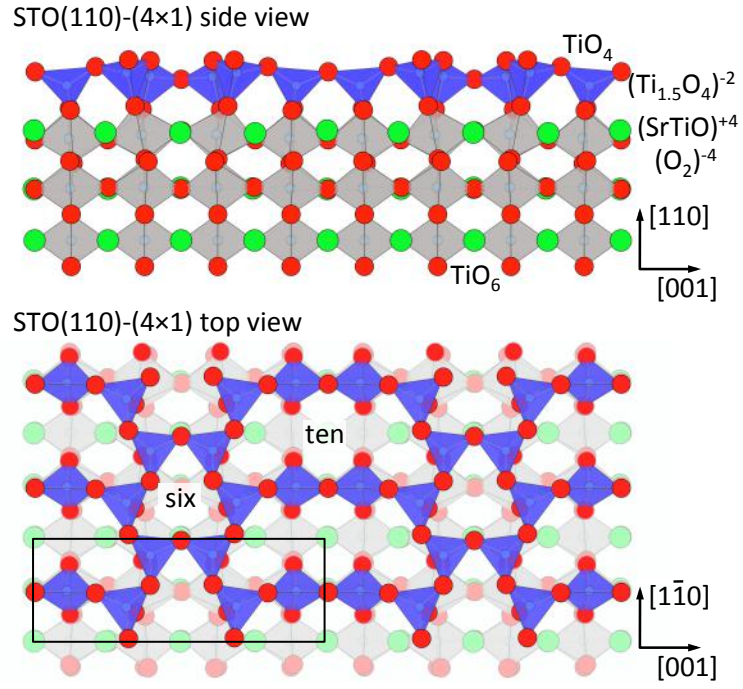


FIGURE 3.3.: $\text{SrTiO}_3(110)-(4 \times 1)$ structure model; side and top view. TiO_4 tetrahedra and TiO_6 octahedra are highlighted in dark blue and gray, respectively. Sr, Ti, and O atoms are colored in green, pale blue, and red, respectively. Crystallographic information file taken from ref. [70].

3. Results

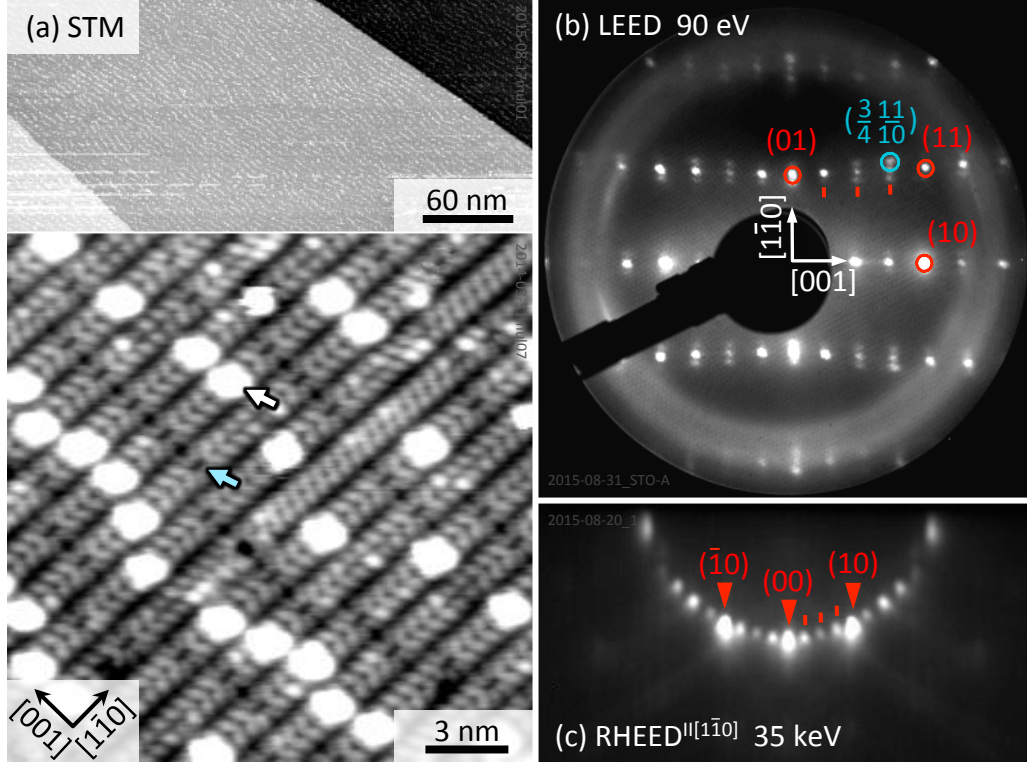


FIGURE 3.4.: STM image (a), LEED pattern (b), and RHEED pattern (c) of the $\text{SrTiO}_3(110)-(4 \times 1)$ surface. The lower panel in (a) shows a zoomed view of the (4×1) structure with anti-phase domain boundaries, such as Sr adatoms and Ti_2O_3 vacancy clusters, highlighted by a white and a green arrow, respectively. Tunneling parameters: $U_S = +2.2$ to $+2.3$ V, $I_t = 0.2$ to 0.5 nA.

3. Results

ing either the (5×1) , or the (2×4) reconstruction. As already mentioned above, fine tuning of the near-surface stoichiometry of STO(110) allows for preparing a surface with a single reconstruction only. By deposition of Sr or Ti metal with subsequent annealing in 3×10^{-6} mbar oxygen, the surface structure was adjusted to exhibit only the (4×1) reconstruction. Figure 3.4 shows the (4×1) -reconstructed surface as imaged by STM (a), and the corresponding diffraction patterns from LEED (b) and RHEED (c). The surface after annealing to 1000 °C exhibits terraces of several hundred nm width, separated by one- or two-unit-cell steps, see upper panel in Figure 3.4(a). A zoomed view of this surface (lower panel) shows bright rows oriented along $[1\bar{1}0]$ direction separated by dark trenches. The (4×1) unit cell breaks the mirror symmetry of the STO(110) surface and therefore introduces domain boundaries. Meandering bright dots and dark vacancies are aligned in $[001]$ direction and are found to be Sr-adatoms and Ti_2O_3 vacancy clusters at anti-phase domain boundaries (APDB), respectively [71]. The vacancy-type domain boundary is formed by one possible connection of two (4×1) mirror domains. Calculations showed that these vacancy clusters help to relief the strain that exists between the STO(110) bulk-truncated surface layer and the 'ideal' reconstruction overlayer without domain boundaries. For each $(\text{Ti}_2\text{O}_3)^{2+}$ complex removed at one type of domain boundary (cyan arrow in Fig. 3.4), a $(\text{Sr})^{2+}$ adatom is placed in the other type of domain boundary (white arrow in Fig. 3.4) restoring the charge balance in the surface layer. The LEED pattern (90 eV) and the RHEED pattern (acquired with the RHEED beam parallel to the $[1\bar{1}0]$ direction under a grazing incidence of $\sim 2^\circ$) also reveal a 4-fold periodicity along $[001]$.

Anti-phase domain boundaries on the (4×1) surface

We reported on two different types of vacancy-cluster domain boundaries. This study was published in ref. [72]. At low oxygen partial pressure during annealing, the surface only exhibits the type-I domain boundaries [indicated by the cyan arrows in Fig. 3.4(a) and Fig. 3.5(a)]. At higher O_2 pressure (p_{O_2}) during annealing, the surface exhibits exclusively the type-II domain boundaries, indicated by the red arrows in Figure 3.5(b). Intermediate pressures lead to surfaces with mixed type-I

3. Results

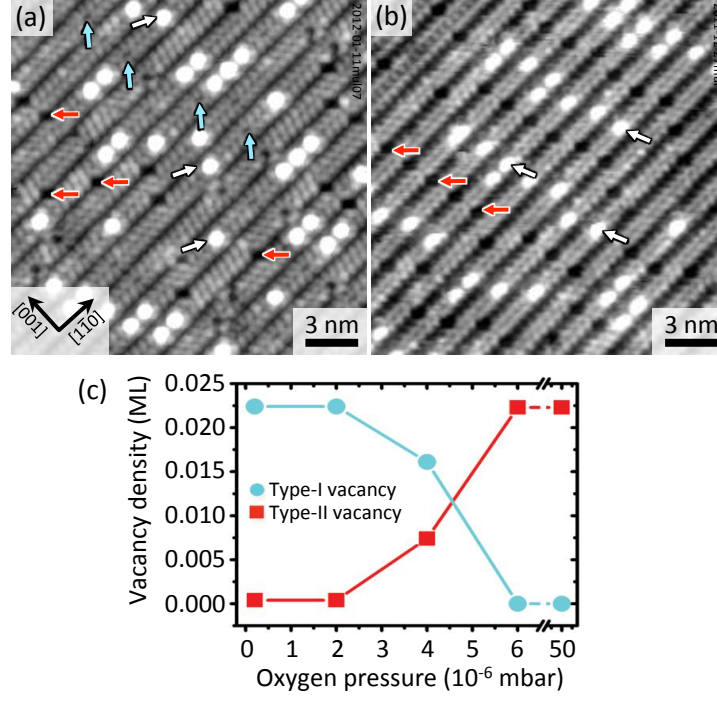


FIGURE 3.5.: Control of the two types of domain boundaries at the SrTiO₃(110)-(4×1) surface through annealing in different O₂ pressure. STM images of surfaces with mixed type-I and type-II (a), and only type-II boundaries (b). The surfaces in (a) and (b) were prepared by annealing in 4×10^{-6} mbar and 6×10^{-6} mbar O₂ pressure, respectively. Intrinsic Sr adatoms are indicated with white arrows. (c) Density of the vacancy clusters versus O₂ pressure during annealing at 1000 °C. Figure adapted with permission from ref. [72]. Tunneling parameters: $U_S = +2.3$ V, $I_t = 0.3$ nA.

3. Results

and type-II domain boundaries, see Fig. 3.5(a)]. Figure 3.5(c) shows statistics over a series of STM images after annealing the surface at different O_2 pressures, indicating that the p_{O_2} can be used to control the type of domain boundaries on the $SrTiO_3(110)-(4 \times 1)$ surface. Domain boundaries on the $SrTiO_3(110)-(4 \times 1)$ surface help to relieve the strain and lead to the formation of a (4×10) superstructure, as confirmed by analysis of STM images and density functional theory calculations [71]. The 10-fold symmetry of the (4×1) surface with the domain boundaries is also visible in the LEED pattern in Figure 3.4(b). In addition to the bulk-derived spots highlighted by the red circles, small side spots appear in a distance of $1/10$ of the reciprocal unit cell in $[1\bar{1}0]$ direction, supporting the 10-fold periodic arrangement of APDBs.

Interpretation of the LEED pattern of a mixed $(4 \times 1) + (5 \times 1)$ surface

After several sputtering and annealing cycles, the resulting surface typically exhibits a mix of two surface reconstructions, which depends on the actual near-surface stoichiometry (*cf.* phase diagram in Figures 3.1 and 3.2). In Section 3.6.5 below, STM images of surfaces exhibiting a mix of $(4 \times 1) + (2 \times 4)$ and $(4 \times 1) + (5 \times 1)$ reconstructions will be presented. The interpretation of the LEED patterns of such mixed surfaces will be discussed here shortly. The LEED pattern of a $(4 \times 1) + (2 \times 4)$ surface is interpreted in a straight-forward way, because of the opposed symmetries of the two reconstructions and a resulting minimal overlap of the spots in LEED, see Figure 3.40(a) in Section 3.6.5. The interpretation of the complex LEED pattern for a mixed $(4 \times 1) + (5 \times 1)$ surface, however, is not so simple. This is due to the partial overlap of LEED spots from the (4×1) and from the (5×1) reconstruction, combined with the superstructure that is formed by (5×1) lines embedded in the (4×1) -reconstructed surface. Figure 3.6(a) shows an STM image of a $(4 \times 1) + (5 \times 1)$ reconstructed surface and the corresponding fast Fourier transformation (FFT) of the STM image is shown in the inset. The STM image shows that the (5×1) rows are to some extent ordered along $[001]$ direction [(4×1) rows exhibit the Sr adatoms visible as bright protrusions]. Fig. 3.6(c) compares the LEED pattern of the surface shown in (a) with the LEED patterns of fully

3. Results

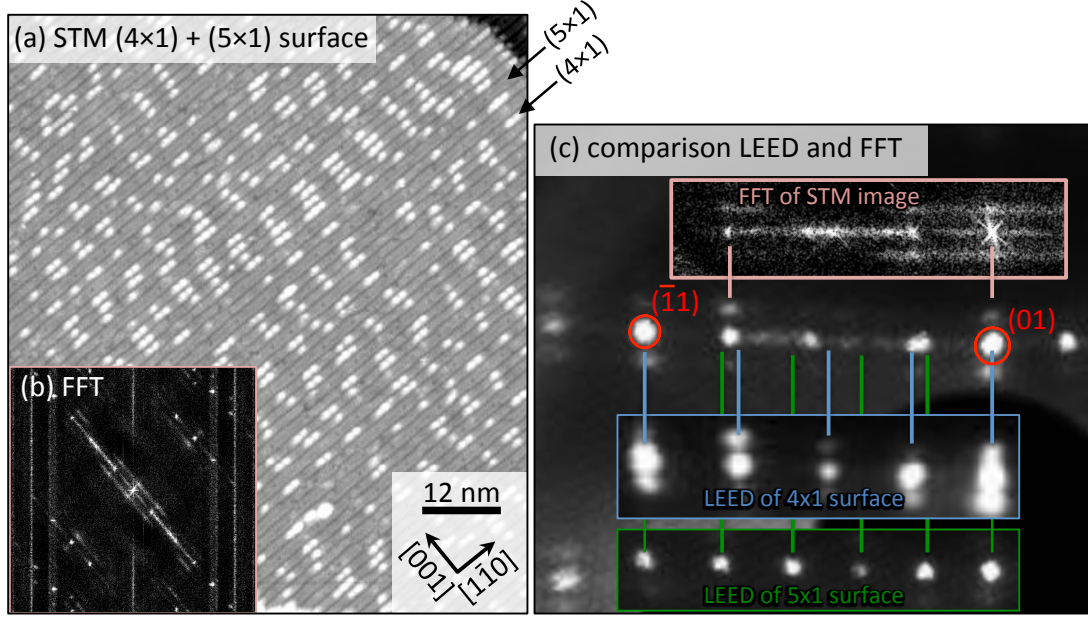


FIGURE 3.6.: (a) STM image and its fast Fourier transformation (FFT) (b) of a mixed $(4 \times 1) + (5 \times 1)$ reconstructed surface. (c) Comparison of the LEED pattern of the surface shown in (a) with the LEED patterns of fully (4×1) , and fully (5×1) -reconstructed surfaces, and with the FFT of the STM image in (a). All LEED patterns acquired with 90 eV electrons. Tunneling parameters: $U_S = +2.4$ V, $I_t = 0.4$ nA

3. Results

(4×1)-, and fully (5×1)-reconstructed surfaces, indicating that the pattern in (c) is not a simple superposition of (4×1) and (5×1) patterns. Bulk-derived spots are highlighted by red circles. The similarity of the FFT and the LEED pattern [see panel (c)] confirms the assignment of this LEED pattern to a mixed (4×1) + (5×1) reconstructed surface.

(4×1) Ti L-edge XAS: Experiment and simulation

To verify the structure model of the (4×1) reconstruction, we performed XAS (also called NEXAFS) measurements of the Ti L-edge on a SrTiO₃(110)-(4×1) sample. In NEXAFS, electrons from occupied states are excited into unoccupied conduction band states, *e.g.*, Ti 2*p*→Ti 3*d*. NEXAFS gives valuable insight into the local electronic and chemical structure, because these unoccupied states are strongly influenced by the chemical environment of the probed atoms. As presented above, the SrTiO₃(110)-(4×1) surface is built up by a network of TiO₄ tetrahedra residing on a bulk STO layer consisting of TiO₆ octahedra, thereby resulting in a system where Ti is in two different chemical environments. The (in STO unoccupied) Ti 3*d* states split into subsets of t_{2g}/e_g or t/e symmetry in an octahedral (Oh) or tetrahedral (Td) crystal field, respectively (see experimental Section 2.2). Figure 3.7 shows NEXAFS spectra of the Ti L_{2,3} absorption edge acquired in the surface sensitive Auger electron yield (AEY) mode, and the more bulk sensitive secondary-electron yield (SEY) mode (see experimental Section 2.2 for details). The spectra show an absorption peak at a photon energy of approximately 458.0 eV (Ti 2*p*_{3/2} → Ti 3*d* Oh-t_{2g}) followed by two overlapping peaks at 459.2 eV (Ti 2*p*_{3/2} → Ti 3*d* Td-e) and 460.1 eV (Ti 2*p*_{3/2} → Ti 3*d* Oh-e_g) and two broad overlapping features at 463.3 eV and 465.4 eV (Ti 2*p*_{1/2} → Ti 3*d* Oh-t_{2g} and Ti 2*p*_{1/2} → Ti 3*d* Oh-e_g). Note that the absorption feature at a photon energy of ~459 eV is considerably enhanced in the AEY spectrum. The assignment of these absorption peaks was determined by simulating L-edge spectra of Ti in octahedral (O_h) and tetrahedral (T_d) crystal fields. These crystal-field multiplet calculations were performed by our co-authors Robert Green and Alex Moewes with the CTM4XAS code [56], and the results were published in ref. [31]. The

3. Results

combination of simulated spectra of O_h and T_d agree very well with the experimental spectra [Fig. 3.7(b)]. The comparison of AEY and SEY spectra therefore confirms that the $\text{SrTiO}_3(110)-(4\times 1)$ surface exhibits tetrahedrally coordinated Ti in the surface layer. The oxygen K-edge NEXAFS spectrum of the pristine (4×1) surface is presented below in Section 3.26.

3.1.2. Transition from $(n\times 1)$ to $(2\times m)$ reconstructions

We have recently reported about the transition from the $(n\times 1)$ to the $(2\times m)$ reconstructions of $\text{SrTiO}_3(110)$ by reactive deposition of Ti. The corresponding study has been published in ref. [31]. In the following we will present experimental aspects about the preparation of $(2\times m)$ -reconstructed surfaces and their characterization by STM, LEED, and XAS.

Characterization of the $\text{STO}(110)-(2\times m)$ surfaces

The $(2\times m)$ ($m=4, 5$) reconstruction is formed upon deposition of Ti onto the $(n\times 1)$ surface at elevated temperature and pressure. A typical recipe to prepare such a surface starts with the preparation of a pristine surface exhibiting a mix of (4×1) and (5×1) reconstructions (see previous section for a characterization of these surfaces). The $(2\times m)$ reconstruction is then formed by reactively depositing $\sim 0.8 \text{ \AA}$ Ti (at $T = 600^\circ\text{C}$, and $5 \times 10^{-6} \text{ mbar O}_2$). A high-resolution STM image of this surface is presented in Figure 3.8(a). This structure appears as wide, bright rows oriented along $[001]$ direction. These rows are separated by dark troughs with bright dots [see white arrow in panel (a)]. Sometimes the rows of periodic bright dots are shifted by one bulk STO unit cell along $[001]$ direction, as indicated by the dashed red line. The bright dots are separated by $\sim 7.8 \text{ \AA}$ along the $[001]$, and $\sim 28.2 \text{ \AA}$ along $[1\bar{1}0]$ direction, see red rectangle in panel (a). The size of the reconstruction unit cell therefore corresponds to a (2×5) reconstruction with respect to $\text{STO}(110)-(1\times 1)$ unit cell. (It should be mentioned that the value of 28.2 \AA does not exactly fit the value of $5 \times \sqrt{2} \times 3.905 \text{ \AA} = \sim 27.6 \text{ \AA}$, probably due to inaccurate calibration of the STM.) Note that the orientation of the reconstruction rows is rotated by 90° as compared to the (4×1) reconstruction (see Section 3.1.1).

3. Results

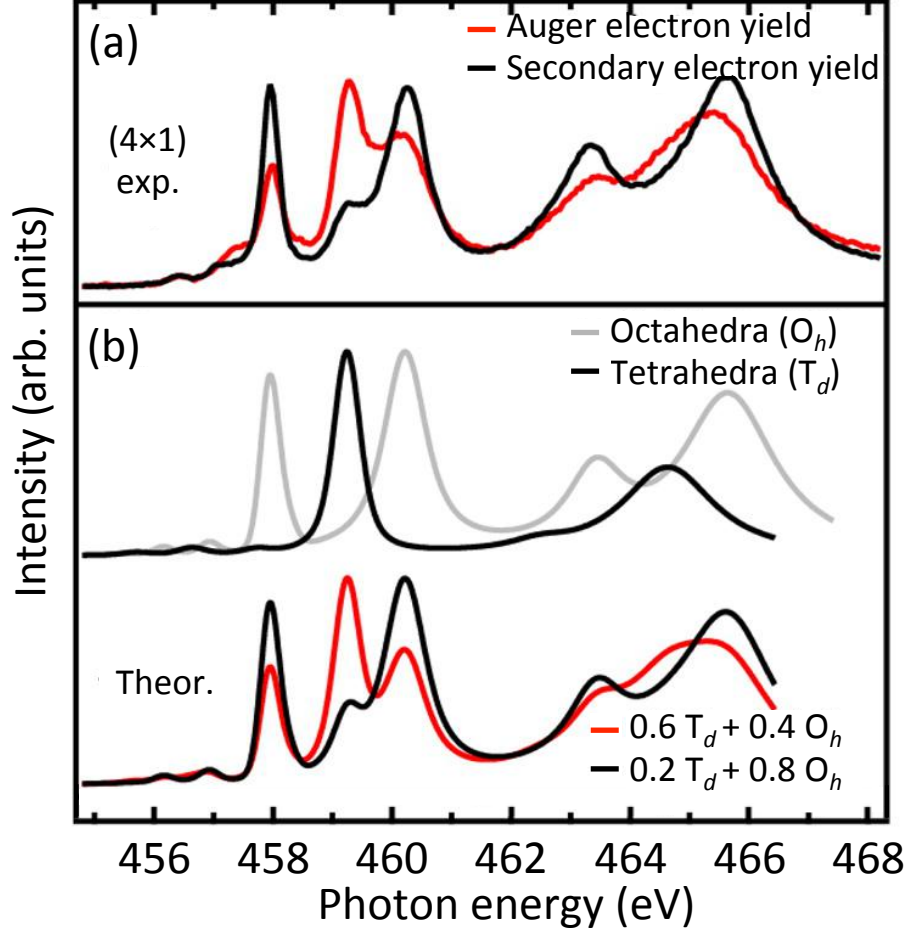


FIGURE 3.7.: (a) Ti $L_{2,3}$ NEXAFS spectra of the (4x1) surface acquired in surface sensitive Auger electron yield (AEY) mode (red curve), and in the more bulk sensitive secondary electron yield (SEY) mode (black curve). (b) Simulated Ti $L_{2,3}$ NEXAFS spectra of Ti ions in octahedral (O_h ; gray curve) and tetrahedral (T_d ; black curve) crystal field, and two combinations of the simulated O_h and T_d spectra. Image adapted from ref. [31].

3. Results

Figure 3.8(b) shows the LEED pattern (90 eV) of the (2×5) reconstructed surface. The bulk-derived spots (highlighted by red circles) were identified by comparing the (2×5) LEED pattern with the LEED pattern of the (4×1) -reconstructed surface shown in Figure 3.4(b). The white arrow in panel (b) verifies the “ $2 \times$ ” periodicity of the bright dots.

The structure model of the (2×5) reconstruction is presented in Figure 3.8(c) (DFT calculations to find the structure model were performed by Laurence Marks and coworkers; the crystallographic information file is available in the supporting information of ref. [31]). It consists of a double-layer of octahedrally coordinated TiO_6 units. To better distinguish the different polyhedra in the unit cell, we have applied different colors in Fig. 3.8(c). Dark blue and orange polyhedra indicate TiO_6 units. Pale blue, green, and purple polyhedra indicate TiO_6 units exhibiting one large Ti-O bond length. Therefore, these polyhedra are drawn as, and referred to, as TiO_5 units. Starting from the subsurface layer of the (2×5) structure, the dark blue TiO_6 octahedra share edges with the substrate $\text{STO}(110)$ layer, while they share corners in-plane. Pale blue TiO_5 units share either edges or corners with the $\text{STO}(110)$ layer, and corners within the plane. Green TiO_5 units share oxygen corners with the $\text{STO}(110)$ layer, and edges with the surface TiO_6 units. The top layer TiO_6 octahedra (orange) share edges with the subsurface units (dark blue, pale blue, and green) and with neighboring octahedra. Purple TiO_5 units share edges with orange octahedra and corners with pale blue TiO_5 units. Five-fold coordinated Sr atoms are centered within neighboring pairs of purple TiO_5 units in the surface layer. The ordering of the Sr atoms results in a “ $2 \times$ ” periodicity along the $[001]$ direction. It should be mentioned that the arrangement of the subsurface layer units also forms a “ $2 \times$ ” periodicity along the $[001]$ direction.

Fig. 3.8(d) shows a simulated STM image overlaid on a high-resolution STM image, verifying the structure model presented in Fig. 3.8(c). Note that the reactive growth of Ti has changed the $(n \times 1)$ surface, consisting of tetrahedral TiO_4 units, into the (2×5) structure, consisting of octahedral TiO_6 units. While the tetrahedral coordination of the $(n \times 1)$ surface is stabilized in spite of large tensile strain [69], which is partly relieved by the formation of anti-phase domain bound-

3. Results

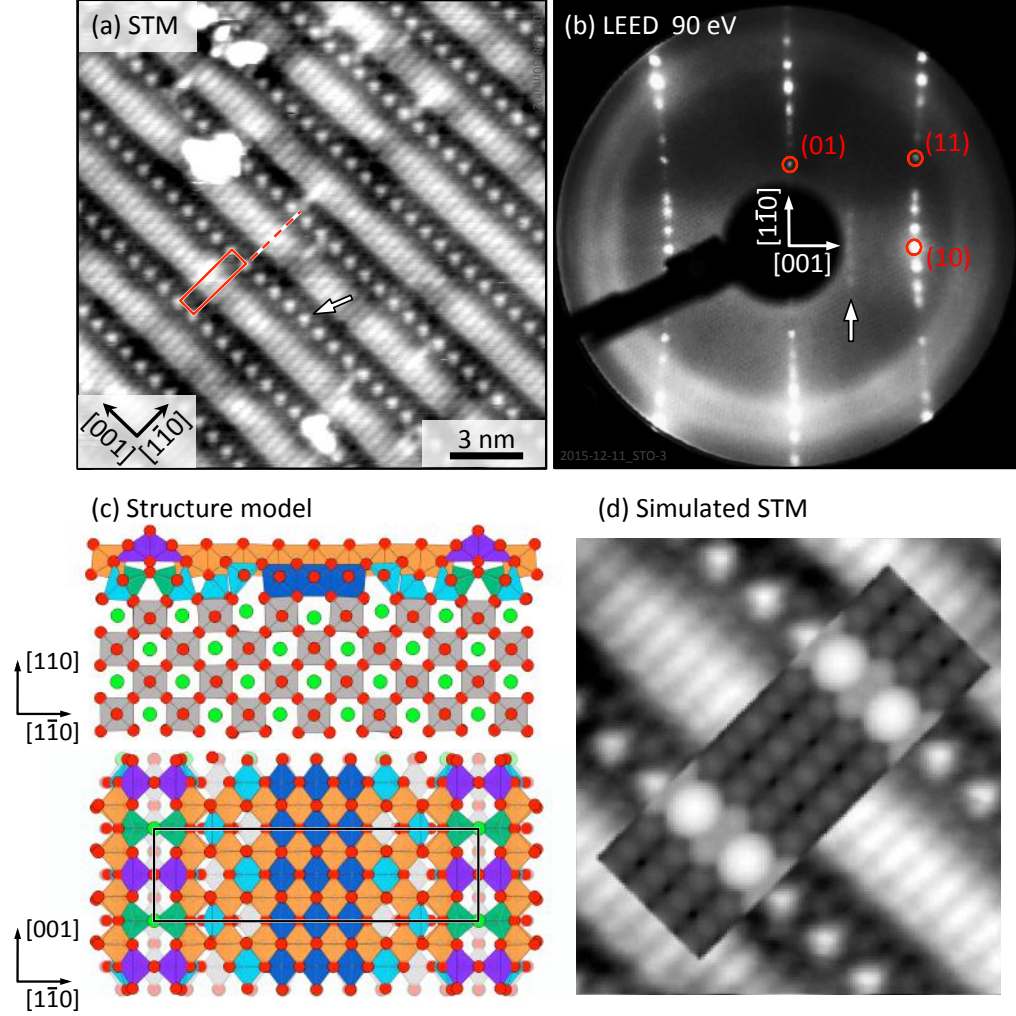


FIGURE 3.8.: Characterization of the $\text{SrTiO}_3(110)-(2 \times 5)$ reconstructed surface. (a) High-resolution STM image of the surface structure. The (2×5) unit cell is indicated in red. The white arrow in (a) indicates Sr atoms. (b) LEED pattern (90 eV) of the $(2 \times m)$ surface. Bulk-derived spots are highlighted by red circles. The white arrow in the LEED pattern confirms the “2 \times ” periodicity along $[001]$ direction. (c) Structure model (upper panel: side view, lower panel: top view). Ti, O, and Sr atoms appear in blue, red, and green, respectively. Outermost octahedra are orange, subsurface octahedra are dark blue. TiO_5 in top layer are purple, and light blue in the subsurface. (d) Simulated STM image overlaid with a high-resolution STM image of the (2×5) structure. Tunneling parameters for (a) and (d): $U_S = +2.2$ V, $I_t = 0.2$ nA. Panels (a,c,d) adapted from ref. [31].

3. Results

aries [71], it appears that at higher TiO_2 coverages this situation is unfavorable, resulting in the transition from TiO_4 to TiO_6 units on the surface [31].

Comparison of NEXAFS on $(n \times 1)$ and $(2 \times m)$ surfaces

To better understand the structural transition observed in STM, and to support the structure model presented above, we performed NEXAFS measurements on (4×1) - and (2×5) -reconstructed surfaces. Figure 3.9 shows the Ti $L_{2,3}$ absorption spectra acquired in AEY, SEY, and TEY mode (see experimental Section 2.2 for details). The Ti L-edge spectrum presented in Fig. 3.9(a) is discussed above in Section 3.1.1. It consists of peaks related to Ti in octahedral coordination (denoted as O_h at photon energies of ~ 458 eV and ~ 460 eV), as well as Ti in tetrahedral coordination (denoted as T_d at a photon energy of ~ 459 eV). As mentioned in Section 3.1.1, the strong T_d peak in the surface sensitive AEY spectrum of the (4×1) surface verifies the tetrahedrally coordinated surface reconstruction, and the T_d peak decreases in accordance with the surface sensitivity of the measurement (from AEY to SEY and to TEY). Fig. 3.9(b) shows the spectra of the (2×5) reconstruction. The spectra show a small difference between AEY and SEY, and the AEY spectrum differs considerably from that of the (4×1) surface. This indicates that the chemical environment of Ti has changed upon reactive Ti growth. As expected, the spectra measured in the bulk-sensitive total electron yield (TEY) mode appear similar for both surfaces, see Fig. 3.9. It should be mentioned that the AEY spectrum of the (2×5) surface resembles that of a lepidocrocite-like titania nanosheet [73], implying structural similarity. This similarity has been used to create the model for this structure.

Growth of $\text{STO}(110)$ - $(2 \times m)$ surfaces

Often, the resulting surface structure after reactive Ti deposition is defective. Figure 3.10 shows STM images of a non-optimal $(2 \times m)$ reconstructed layer [deposition of ~ 0.4 Å Ti, starting from a (6×4) surface (*cf.* phase diagram in Figure 3.1)]. Second-layer islands are observed whenever the amount of deposited Ti exceeds the “optimal” amount necessary to form the $(2 \times m)$ structure, see Figure 3.10(a).

3. Results

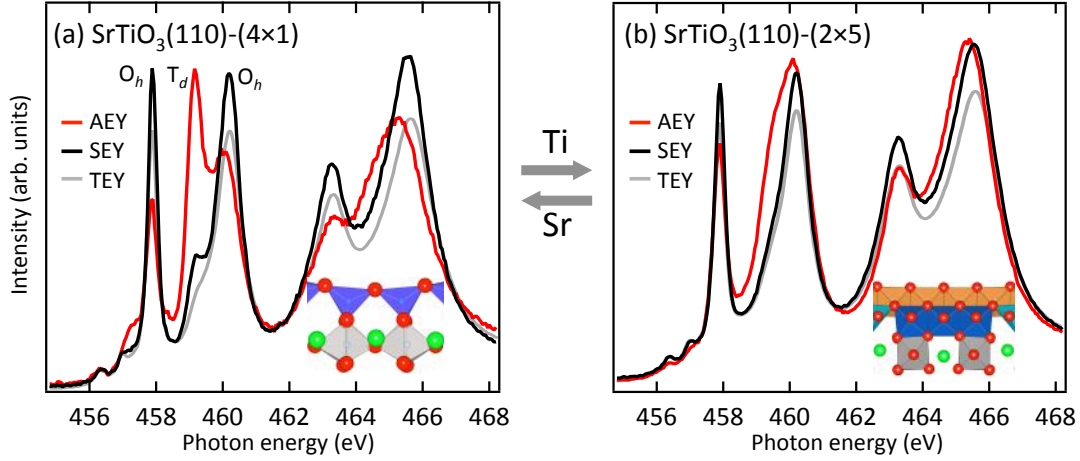


FIGURE 3.9.: Ti $L_{2,3}$ NEXAFS spectra of STO(110) (a) (4×1) - , and (b) (2×5) -reconstructed surfaces. The spectra were acquired in the surface sensitive Auger electron yield (AEY) mode (red curve), the more bulk sensitive secondary electron yield (SEY) mode (black curve), and the bulk sensitive total electron yield (TEY) mode (gray curve). Image adapted from ref. [31].

Such a second layer will be referred to as $(1 \times m)$ in the following, and its structural details are presented below. Figure 3.10(b) shows a high-resolution STM image of this surface. Dark defect lines (oriented along the $[1\bar{1}0]$ direction) were observed on the surface. The red lines in Fig. 3.10(b) indicate that the dark defect lines also act as a domain boundary between $(2 \times m)$ and $(2 \times l)$ reconstructed lines.

In order to obtain a well-ordered and uniformly-reconstructed (2×5) surface, it is of primary importance to perform the growth on a uniform substrate. As an example, Figure 3.11 shows the effect of reactively growing Ti on a $(4 \times 1) + (2 \times 4)$ reconstructed substrate, see Fig. 3.11(a). Note that there are two different structures with the same (2×4) symmetry on the STO(110) surface. One is slightly Ti-rich with respect to the (4×1) structure (see Fig. 3.39 in Section 3.6.5), while the other one [mentioned in Fig. 3.10(b)] belongs to the $(2 \times m)$ reconstructions with $m = 4$, which is more Ti-rich. As also mentioned later in Section 3.6.5, the (4×1) and (slightly Ti-rich) (2×4) reconstructions do separate on the surface. (2×4) areas are observed near step edges, see Fig. 3.11(a) [also compare Fig. 3.39(c)]. According to the phase diagram presented in Section 3.1 and Figure 3.1, the (2×4)

3. Results

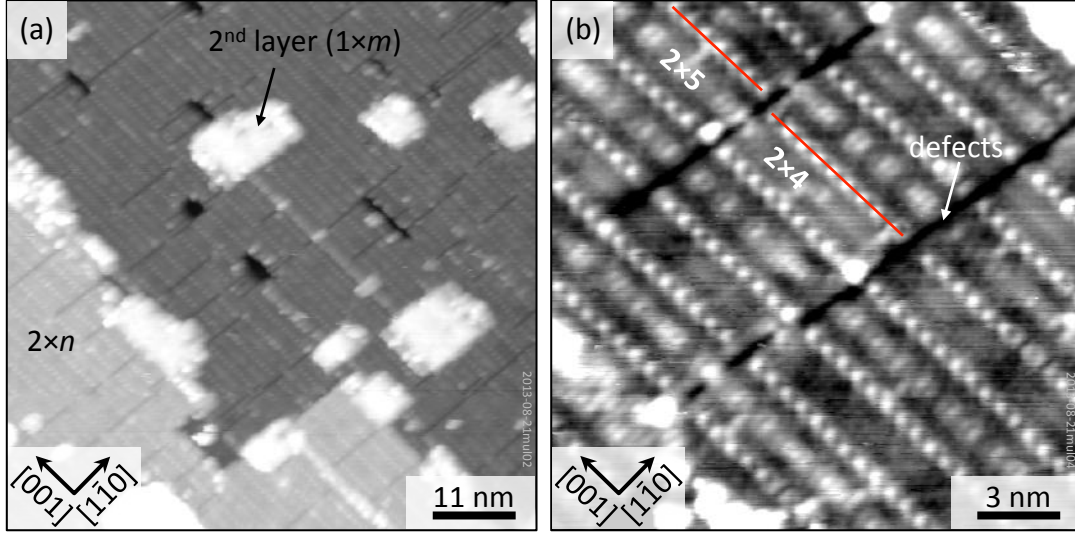


FIGURE 3.10.: STM images of $(2 \times m)$ reconstructed surface with defects and 2^{nd} -layer islands indicated. Tunneling parameters: (a) $U_S = +2.4$ V, $I_t = 0.22$ nA; (b) $U_S = +2.0$ V, $I_t = 0.15$ nA.

structure exhibits a higher Ti-content as compared to the (4×1) structure. Figure 3.11(b) shows the surface in (a) after reactive deposition of Ti (~ 1.6 Å Ti). Far from step edges, approximately 83 % of the surface exhibits the second-layer structure, while in the voids the (2×5) structure is visible [see inset of Fig. 3.11(b)]. (Because of the similarity of the LEED pattern and its appearance in STM (both shown below) with the (2×5) reconstruction, this second-layer structure is named $(1 \times m)$ in the following.) Close to step edges instead, the surface is fully covered by the $(1 \times m)$ structure. By comparing Fig. 3.11(a) and (b), we can conclude that, upon reactive Ti growth at 600 °C, the (relatively) low diffusivity of the deposited species does not allow for a large-area equilibration of the surface structures, so that former (2×4) areas are driven to a Ti-rich surface composition with respect to the former (4×1) terraces.

3. Results

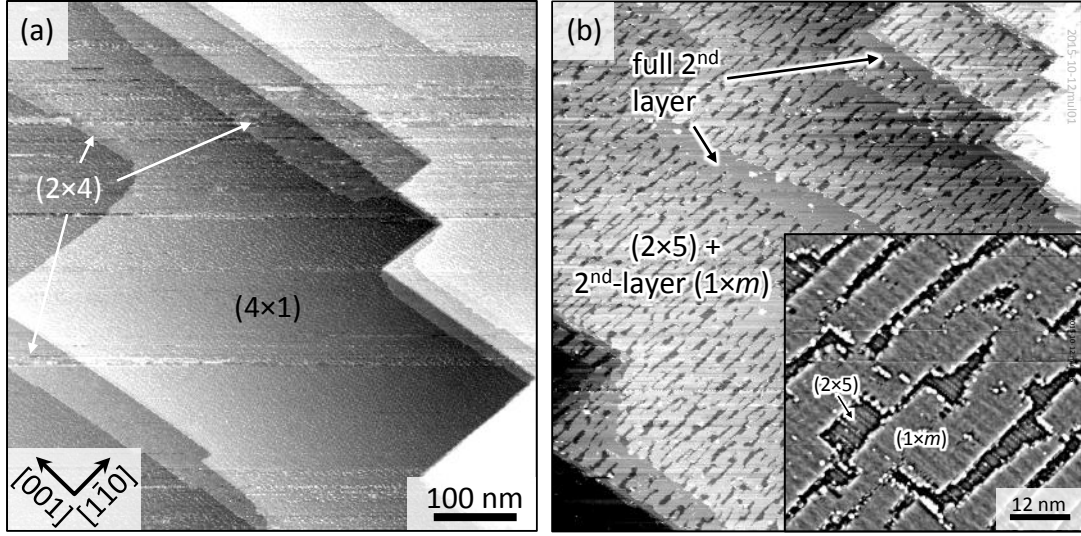


FIGURE 3.11.: STM images ($640 \times 640 \text{ nm}^2$) before (a) and after (b) deposition of Ti onto a non-uniform substrate surface (different positions on the sample). (a) Surface with mixed $(4 \times 1) + (2 \times 4)$ reconstructions. (b) Surface after Ti deposition. Areas with full 2^{nd} layer are indicated. The inset shows a zoomed, high-pass-filtered STM image of the surface in (b). Tunneling parameters: (a) $U_S = +1.8 \text{ V}$, $I_t = 0.37 \text{ nA}$; (b) $U_S = +2.2 \text{ V}$, $I_t = 0.96 \text{ nA}$, inset: $U_S = +2.2 \text{ V}$, $I_t = 0.21 \text{ nA}$.

3. Results

Characterization of the 2nd-layer ($1 \times m$) structure

In the following, we will briefly discuss the structure of the second-layer ($1 \times m$) structure. This structure is formed upon increasing the amount of deposited Ti, as compared to the optimal amount necessary to form the (2×5) structure. Figure 3.12 shows STM images of a surface fully covered by such a second-layer ($1 \times m$) structure. Fig. 3.12(a) shows a large-area STM image of this surface exhibiting ~ 30 nm wide terraces. Similar to the (2×5) reconstruction, this surface exhibits (faint) rows oriented along the $[001]$ direction. The inset shows the corresponding LEED pattern (90 eV). The bulk-derived spots (red circles) are determined by comparison with the LEED pattern of the (4×1)-reconstructed surface shown in Figure 3.4(b). The LEED pattern looks very similar to the one measured on the (2×5) surface. Note that the spots indicating the “ $2 \times$ ” periodicity along the $[001]$ direction are missing [*cf.* Fig. 3.8(b)]. Fig. 3.12(b) shows a high-resolution STM image of this surface structure. It shows a lattice of bright dots with a distinct modulation of the brightness along $[001]$ direction. The unit cell of the lattice (red rectangle) measures ($\sim 3.81 \text{ \AA}^{[001]} \times 3.00 \text{ \AA}^{[1\bar{1}0]}$). Note that while the size along $[001]$ direction is similar to the one of the STO(110) unit cell ($\sim 3.905 \text{ \AA}^{[001]} \times 5.552 \text{ \AA}^{[1\bar{1}0]}$), it is different along $[1\bar{1}0]$ direction. The red, dashed lines in Fig. 3.12(b) indicate the superstructure along the $[1\bar{1}0]$ direction, with a periodicity of 32.94 \AA , corresponding to $\sim 11 \times 3.00 \text{ \AA} = 33 \text{ \AA}$ or to $6 \times 5.552 \text{ \AA} = 33.31 \text{ \AA}$. Therefore this surface is referred to as (1×6) with respect to the STO(110)-(1×1) unit cell. The larger unit cell size of this structure along $[1\bar{1}0]$ direction, as compared to the (2×5) structure, is also visible in the comparison of the corresponding LEED patterns presented in Fig. 3.12(c) – side spots on the (1×6) surface are closer to the bulk spots (as compared to the (2×5) surface) indicating a larger unit cell in real-space.

It should be mentioned that the appearance of this surface structure and the modulation along $[1\bar{1}0]$ direction very much resemble that of lepidocrocite-like nanosheets on (1×2)-Pt(110), as presented in ref. [74].

3. Results

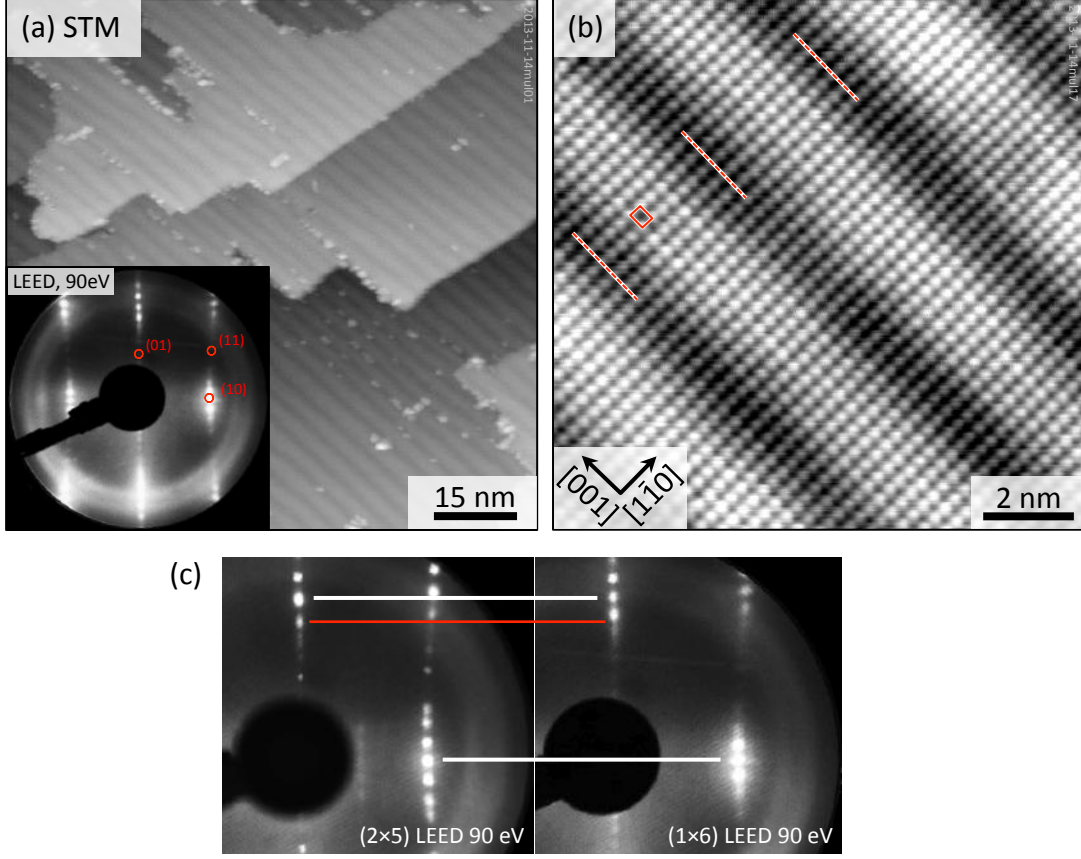


FIGURE 3.12.: (a) STM image of a surface fully covered with the (1×6) structure after reactive Ti deposition. The inset in (a) shows the corresponding LEED pattern (90 eV). (b) High-resolution STM image of this surface structure. The red rectangle indicates the smallest unit of the surface ($\sim 3.81 \text{ \AA} \times 3.00 \text{ \AA}$). The dashed, red lines indicate a superstructure along $[1\bar{1}0]$ direction (periodicity of $\sim 33 \text{ \AA}$). (c) Comparison of the LEED patterns of a (2×5) and a (1×6) surface, indicating a difference in the position of LEED spots. STM parameters: $U_s = +1.2\text{--}1.5 \text{ V}$, $I_t = 0.30 \text{ nA}$.

3.2. SrTiO₃(110)-(4×1) and its interaction with H₂O

The interaction of water with solid surfaces is of great interest not only due to the omnipresence of H₂O in nature. The adsorption of water at surfaces is important for corrosion, in the field of heterogeneous catalysis, and for solar energy conversion. Water can adsorb on metal-oxide surfaces either in a molecular, or a dissociative way. Preferential dissociation can be observed on surface oxygen vacancies (V_{OS}) or structural defects on the surface. Understanding the interaction of water with the pristine substrate surface is a prerequisite for systematically altering the surface properties and reactivity by adsorption of metal, or metal oxide particles or clusters. In this section, we present experimental (STM, XPS, UPS) and theoretical (DFT) results on the interaction of H₂O with the SrTiO₃(110)-(4×1) surface. We find that the tetrahedral surface layer of the (4×1) structure is relatively inert towards the adsorption of water at room temperature, and that water adsorbs molecularly only at low temperatures (LT), or dissociatively at surface oxygen vacancies. We identify surface hydroxyls in STM and verify their adsorption by means of photoemission spectroscopy and density functional theory. Most of the results presented in this section have been published in ref. [8]. Density functional theory calculations have been performed by Xianfeng Hao and Cesare Franchini.

3.2.1. Water adsorption in STM

Adsorbed water, or its dissociation products are normally easily detected by STM, but the identification and assignment of these features in STM images is often difficult. Several surface features are typically related to water adsorption, *i.e.*, molecularly adsorbed water, dissociatively adsorbed water or surface hydroxyls, and oxygen vacancies at which water preferentially adsorbs dissociatively. Surface hydroxyls can also be created by adsorption of atomic hydrogen, which provides a well-defined way of studying these features. Atomic hydrogen is known to preferentially adsorb on the surface oxygen atoms, forming hydroxyl groups, while

3. Results

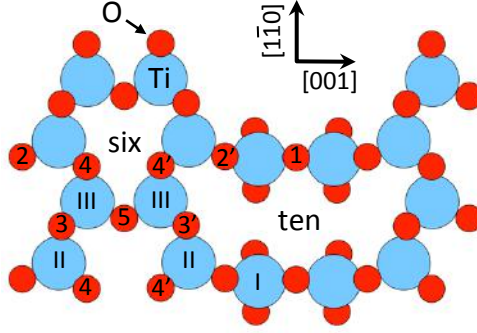


FIGURE 3.13.: Top view of the topmost layer of the $\text{SrTiO}_3(110)-(4 \times 1)$ surface. Different surface Ti and O atoms corresponding to different adsorption sites are labeled.

molecular water typically adsorbs at the cation sites [54]. The (4×1) surface provides several possible adsorption sites for hydrogen and water. Figure 3.13 shows a schematic of the (4×1) surface layer with the different surface Ti and O atoms labeled with Roman numerals and Arabic numbers, respectively. Figure 3.14(a) shows an empty-states STM image of the $\text{SrTiO}_3(110)$ surface after exposure to atomic hydrogen. The surface is (4×1) reconstructed with some lines of (5×1) reconstruction present. The bright rows of the reconstruction correspond to Ti_{III} and Ti_{II} atoms in the six-member ring of the reconstruction, *cf.* Figure 3.13. Intrinsic Sr adatoms centered within the (4×1) -reconstructed lines are labeled with white arrows.

Atomic hydrogen was dosed onto the surface by backfilling the chamber with a pressure of 1×10^{-6} mbar H_2 while keeping a hot tungsten filament in line of sight with the sample. The hydrogen cracking efficiency was estimated to be 5% with the W filament at a temperature of about 2000 °C, as determined by Sutoh *et al.* [75]. The adsorption of atomic hydrogen introduces new features in STM images. Bright protrusions appear on the surface, located preferentially at the sides of the (4×1) rows, see blue arrows in Figure 3.14(a). It has been confirmed by DFT calculations (see Table 3.1 below) that atomic hydrogen prefers to adsorb at the O3 site (*cf.* Figure 3.13) on the sides of the reconstruction lines. Additionally, simulated STM images of adsorbed atomic H by Li *et al.* agree well with the experimental ones, see ref. [70]. Therefore, these features are assigned to hydroxyl

3. Results

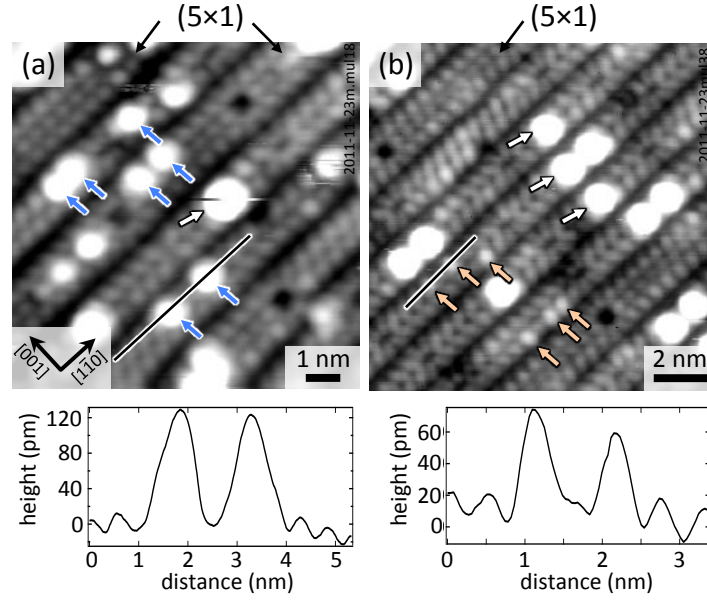


FIGURE 3.14.: STM images of the $\text{SrTiO}_3(110)-(4 \times 1)$ surface; locally a few (5×1) rows are present. (a) After exposure to atomic hydrogen and (b) after flashing the surface in panel (a) to $\sim 300^\circ\text{C}$. Sr adatoms, hydroxyls, and oxygen vacancies appear in various levels of brightness and are labeled by white, blue, and orange arrows, respectively. The line profiles in the lower panels were taken at the lines in the STM images. STM tunneling parameters: $U_S = +2.3$ V, $I_t = 0.1$ nA

3. Results

groups formed by a surface oxygen atom (O3) with an adsorbed hydrogen atom. The hydroxyls show an apparent height of ~ 130 pm, in contrast to the Sr adatoms, which show an apparent height of ~ 240 pm. It should also be mentioned that we observe interaction of H with Sr adatoms, as indicated by the streaky appearance of the Sr adatom highlighted with the white arrow in Figure 3.14(a).

Annealing the hydroxylated surface to $\sim 300^\circ\text{C}$ for 10 min in UHV changes the surface appearance considerably. The bright OH features have transformed into less bright features at approximately the same position, as indicated by the orange arrows in Figure 3.14(b). These features show an apparent height of ~ 70 pm and are assigned to surface oxygen vacancies (V_O) sitting also at the side of the (4×1) rows, similar to the hydroxyls. This assignment is supported by several reports in literature showing that flash-annealing of hydroxylated oxide surfaces leads to the desorption of molecular water [76–78]. Additionally, DFT calculations reveal the lowest formation energy for vacancies created at the O3 site, as shown below in Table 3.1 and in ref. [70].

Figure 3.15(a) shows an LT-STM image of the $\text{SrTiO}_3(110)$ surface after exposure to 0.3 Langmuir ($1\text{ L} = 1.33 \times 10^{-6}$ mbar s) water at 110 K. Bright protrusions appear in the dark trenches separating the reconstruction rows [features highlighted by cyan circles in Figure 3.15(a)]. These features show an apparent height of ~ 80 pm. A temperature programmed desorption study by Wang *et al.* on the $\text{STO}(001)$ surface revealed molecular water desorption starting from around 200–260 K at low exposures ($< 1\text{ L}$) [77]. We therefore attribute these features to molecularly adsorbed water located close to the Ti_I site. DFT calculations [8] confirm the preferential adsorption of water at Ti_I sites in the ten-member ring (*cf.* Figure 3.13) with an adsorption energy of -0.72 eV to -1.07 eV (depending on the functional used in the calculation).

Figure 3.15(b) shows an STM image after dosing 3 L water at RT. Features similar to the hydroxyls formed after dosing atomic hydrogen are found in pairs on the sides of the (4×1) and (5×1) rows. The features are highlighted by blue arrows in Figure 3.15(b), show an apparent height of around 90 pm, and are separated by two unit cells along the $[1\bar{1}0]$ direction. It is likely that these features

3. Results

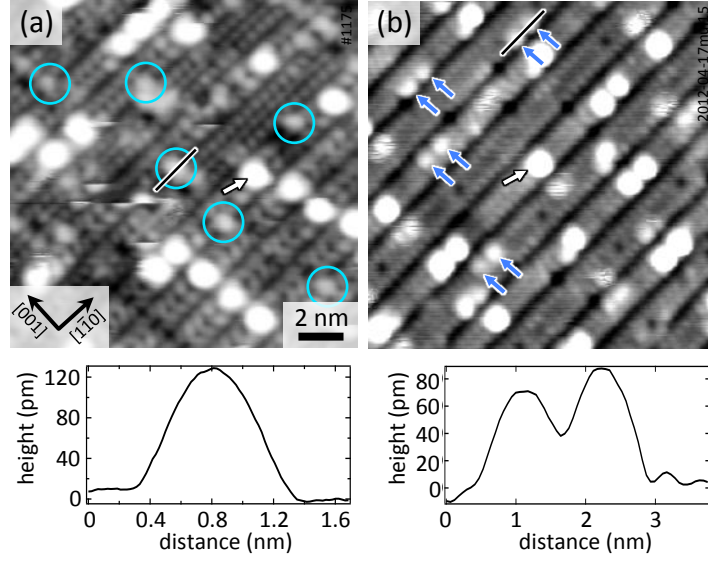


FIGURE 3.15.: STM images of the $\text{SrTiO}_3(110)-(4 \times 1)$ surface after exposure to (a) 0.3 Langmuir water at 110 K, imaged at 78 K; (b) 3 L water at RT, imaged at RT. Molecularly adsorbed water, hydroxyl pairs, and Sr adatoms are highlighted by cyan circles, blue arrows, and white arrows, respectively. The line profiles in the lower panels were taken at the lines in the STM images. The STM tunneling parameters: $U_S = +2.1$ V, $I_t = 0.1$ nA

3. Results

configurations	O1	O2	O3	O4	O5
V _O formation energy (eV)	6.43 (0.83)	5.95 (0.35)	5.60 (0.0)	5.68 (0.08)	5.76 (0.16)
H adsorption energy (eV)	1.79 (-0.40)	1.93 (-0.26)	2.19 (0.0)	2.16 (-0.03)	1.62 (-0.57)

TABLE 3.1.: Oxygen vacancy formation energy $E_f(V_O)$ and hydrogen adsorption energy $E_{\text{ads}}(H)$ for different oxygen sites obtained with the PBE functional. Oxygen sites names according to Figure 3.13. Numbers in parentheses refer to the relative energy with respect to the most stable configuration. See ref. [8] for details.

are formed by the dissociation of water molecules on surface oxygen vacancies. The density of these hydroxyl pairs is approximately 0.01 ML (1 ML = 4.64×10^{14} atoms/cm², 1 ML is defined as the density of STO(110)-(1 × 1) unit cells) and does not increase upon further water dosage, supporting the assignment to H₂O dissociating at V_Os.

3.2.2. Water adsorption in PES

In this section, photoemission spectroscopy results acquired at the Maxlab synchrotron facility are presented. The PES geometry (*i.e.*, 55° grazing emission w.r.t. the surface normal) and kinetic energy of photoelectrons were optimized for highest surface sensitivity. Figure 3.16 combines photoemission spectra of the valence band (a) with a zoom into the gap region (b), and the O 1s core level (c), of differently treated (4×1) surfaces. For comparison, the spectra have been aligned to the main spectral feature of the valence band of the pristine surface at $E_B \approx 7$ eV. As discussed in the Introduction (see Section 1.2), the valence band of SrTiO₃ is composed predominantly from O 2p states. In photoemission, the valence band of the pristine surface shows two prominent features at 7 eV and 5.2 eV binding energy, see black curve in Figure 3.16(a). The onset of the valence band was determined by linearly extrapolating the rising edge of the VB

3. Results

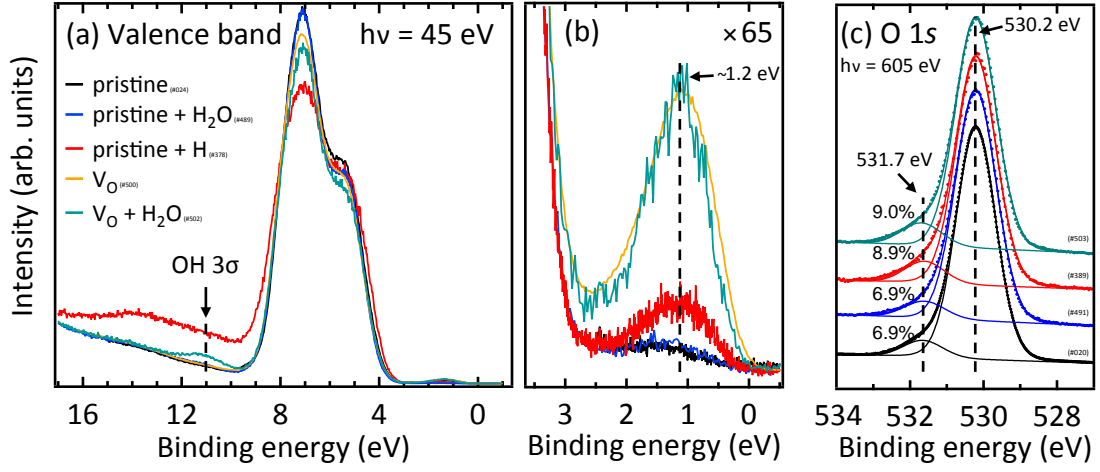


FIGURE 3.16.: Valence band (a), gap region (b), and O 1s (c) photoemission spectra of the pristine surface (black), after exposure to water (blue), atomic hydrogen adsorption (red), after creation of oxygen vacancies (orange), and after dosing water onto the reduced surface (cyan). All spectra were acquired at RT.

and amounts to $E_g \approx 3.2$ eV. This value is in agreement with values of the band gap mentioned in the literature [28], and with the n-type doping of the single crystals and an expected Fermi level close to the conduction band. No states are observed in the band gap, indicating that the Nb dopants do not induce in-gap states (IGS). The O 1s spectral feature is shown in Figure 3.16(c). The O 1s spectrum of the pristine surface shows a main peak at $E_B = 530.2$ eV with a small high-binding-energy shoulder at $E_B = 531.7$ eV. Dosing up to 240 L water at RT onto the pristine surface does not introduce any additional features, nor any changes in either the valence band or the O 1s spectra. This indicates that water does not adsorb on the pristine surface at RT, well in line with the STM results presented above. After dosing atomic hydrogen on the (4×1) surface, an in-gap state with a binding energy of around 1.2 eV is formed [see red curve in Figure 3.16(b)], as well as a broad feature directly below the valence band. The O 1s spectrum shows an increased high-binding-energy shoulder, as expected for surface hydroxyls. According to the STM study presented above, water only adsorbs at the (4×1) surface at low temperature, and interaction of atomic hydrogen

3. Results

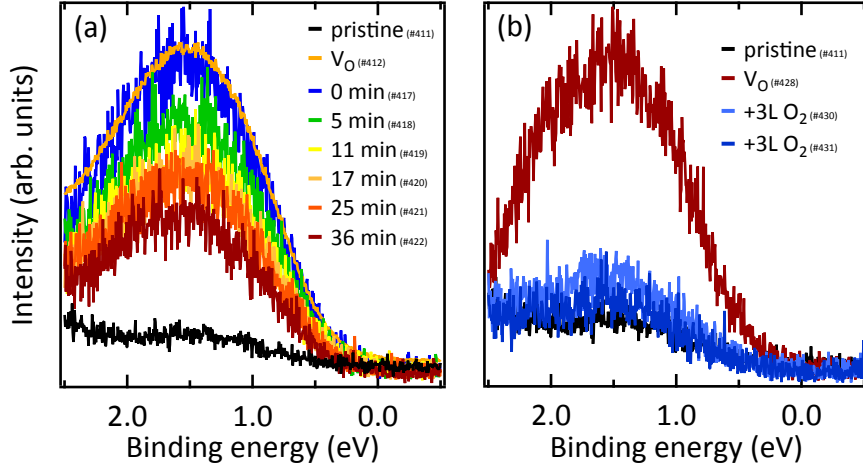


FIGURE 3.17.: Photoemission spectra of the gap region acquired at RT. (a) Spectra of the gap-region of the pristine surface (black), of the in-gap state formed after 42 scans (~ 28 min, orange curve), and after different time intervals with no illumination (green to dark red). (b) In-gap state spectra of the pristine surface (black), the surface after creation of V_O s by exposure to synchrotron light (red), and after dosing 3 Langmuir (pale blue) and 6 L (dark blue) of oxygen.

with intrinsic Sr adatoms is observed. We therefore tentatively assign the broad feature below the valence band to Sr-OH species on the surface. Sr-OH formation has been reported upon dosing water onto SrO and TiO_2 -terminated STO(001) surfaces [79].

Oxygen vacancies have been created by exposing the sample to intense synchrotron radiation. An IGS similar to the one after hydrogen adsorption is formed. Figure 3.17(a) shows the creation of the IGS. We exposed the pristine surface (black curve) to the synchrotron radiation for about 28 min by repeating the gap-region scan 42 times. A clear state is formed after this treatment (orange), whose intensity decreases with time – spectra were acquired after different time intervals with no synchrotron illumination in between. The pressure in the synchrotron beamline analysis chamber was below 10^{-10} mbar, suggesting that the decrease of the IGS is due to diffusion of V_O s away from the very surface towards the bulk, rather than from adsorption of residual gas molecules. In order to verify the correspondence of the IGS with V_O s, we dosed O_2 onto the reduced surface. Following this treatment, the IGS was quenched considerably, thus verifying that the IGS originates

3. Results

from oxygen vacancies, see Figure 3.17(b).

Dosing water onto the reduced surface does not change the IGS, which formed upon creation of V_{OS} , while a peak at $E_B = 11$ eV appears [see Fig. 3.16(a) and (b)]. This peak is indicative for surface hydroxyls (compare experimental Section 2.1) and suggests that the oxygen vacancies have transformed into surface hydroxyl species, which is also evident in the O 1s spectra, see Figure 3.16(c). Dosing water onto the reduced surface induces an increase of the high binding energy shoulder of the O 1s spectra, similar to the one with adsorbed atomic hydrogen.

3.2.3. Summary and discussion: H_2O adsorption on $SrTiO_3(110)-(4 \times 1)$

Experimental and theoretical results show that H_2O does not adsorb on the pristine, stoichiometric surface at RT, while it does adsorb molecularly at the Ti_I sites at LT. Dissociation occurs at surface oxygen vacancies, which preferentially form at the O3 sites (compare Figure 3.13 for adsorption sites). The resulting hydroxyl pair is located at two O3 sites, which are two unit cells apart. One proton from the dissociated H_2O molecule has obviously moved away from its original V_O adsorption site. Water-mediated proton hopping has already been observed previously. Merte *et al.* concluded from STM, TPD, and DFT calculations that the proton hopping on FeO thin film is facilitated by a water molecule that picks up the adsorbed proton, moves on as an H_3O^+ ion, and releases one of its protons somewhere else on the surface [80]. A different proton hopping mechanism has been observed by Wendt *et al.* on the $TiO_2(110)$ surface. The proton hopping is facilitated by pseudo-dissociated H_2O molecules on neighboring undercoordinated Ti^{4+} sites, *i.e.*, by dissociation and reforming of H_2O molecules [81]. Since water does not adsorb on the stoichiometric (4×1) surface at RT, the latter possibility is unlikely. It could be speculated that the OH pair after dissociation of H_2O on V_{OS} enhances the adsorption energy of molecular water until the OH group is driven apart and the H_2O molecule desorbs again.

The preferred site for creation of an V_O (O3) is also the most stable site for hydrogen adsorption. In addition, hydrogen interacts with intrinsic Sr adatoms, as

3. Results

indicated by STM and PES results. In order to discuss the results presented here, we compare the $\text{SrTiO}_3(110)-(4\times 1)$ surface with the anatase $\text{TiO}_2(001)-(1\times 4)$ surface [82], which was found to dissociate H_2O on the stoichiometric surface [83]. Similar to the $\text{STO}(110)-(4\times 1)$ surface, the (1×4) reconstruction on anatase (001) consists of tetrahedral TiO_4 units. Active sites on oxide surfaces are typically related to excess electrons with energies near the band gap [84]. However, there is no indication of Ti^{3+} or states inside the band gap on both stoichiometric surfaces; on both surfaces, Ti is in $4+$ valence state. The biggest difference between the two reconstructions lies in their geometric structure. The $\text{SrTiO}_3(110)-(4\times 1)$ surface consists of a 2D network of quite regular tetrahedra. According to DFT calculations, the TiO_4 tetrahedra on $\text{STO}(110)$ show a Ti-O bond length ranging from 1.83–1.90 Å and an O-Ti-O bond angle in the range of 92.8–123.1°. The anatase (001)- (1×4) , on the other hand, consists of 1D rows of distorted tetrahedra. The Ti-O bond lengths along these rows alternate between 2.13 Å and 1.83 Å, while the bonds perpendicular to the rows are 1.81 Å. Interaction of H_2O with oxide surfaces is typically facilitated by metal cation sites (Lewis acid sites, *i.e.*, electron pair acceptors) combined with a near-by O atom (Brønsted base, *i.e.*, proton acceptor). In case of the STO and the anatase surface, Ti acts as the acidic sites on the surface.

From the geometric considerations above it is evident that the distorted tetrahedron on the anatase (001) surface exposes the Ti cation more to its surrounding than the regular tetrahedron on the $\text{STO}(110)$ surface. We therefore propose that the flexible network on the anatase surface facilitates the water dissociation. At the $\text{SrTiO}_3(110)-(4\times 1)$ surface, the 2D network is more rigid, which contributes to its inertness. Similar behavior was found for V_2O_3 films on $\text{Au}(111)$ [85, 86], and TiO_x films on $\text{Au}(111)$ [87, 88]. Both surfaces feature metal cations coordinated in a quasi-tetrahedral arrangement. In case of the TiO_x , Ti is adsorbed in a honeycomb arrangement on the $\text{Au}(111)$ surface, and the oxygen atoms sit in bridge sites between Ti atoms, resulting in three-fold coordinated Ti. On the V_2O_3 surface, V atoms sit in three-fold hollow sites of oxygen atoms without (reduced), or with one additional oxygen atom above the V atom (vanadyl surface).

3. Results

Both groups reported on weak interaction of water with these surfaces. In case of the V_2O_3 film, only the reduced surface exhibits reactivity toward water, *i.e.*, the surface after removal of the terminal O, and therefore with full exposure of the V atom [86]. In case of the TiO_x films, only the so-called pinwheel structure exhibits reactivity towards H_2O , in which Ti is in a mixed 3-, and 4-fold coordination on the surface [88].

3.3. Single Ni adatoms on the $\text{SrTiO}_3(110)-(4\times 1)$ surface

Single metal adatoms on oxide support have attracted great interest in the catalysis community because of a high activity in heterogeneous catalysis, and a high efficiency and therefore low cost [89]. Approaches to produce single metal adatoms include mass-selected soft-landing, wet-chemistry approaches, as well as vapor deposition in ultra-high vacuum (UHV) conditions [89–91]. However, stabilizing single atoms on oxide supports has remained a significant challenge because sintering occurs under realistic reaction conditions [92]. Single adatoms are typically stabilized by surface defects, moiré patterns, or surface reconstructions with strong modulation of the surface potential. Here we show results of single Ni adatoms adsorbed on the $\text{SrTiO}_3(110)-(4\times 1)$ surface. With STM, we observe the adsorption of single Ni adatoms at different sites in the reconstruction unit cell at room temperature (RT), which was confirmed by density functional (DFT) theory calculations. Clustering is only observed at higher substrate temperatures. PES results show the formation of a state inside the band gap. Combining PES and DFT calculations, we discuss the charge state of the Ni adatoms. Most of the results presented here have been published in ref. [93]. DFT calculations have been performed by Xianfeng Hao and Cesare Franchini.

3. Results

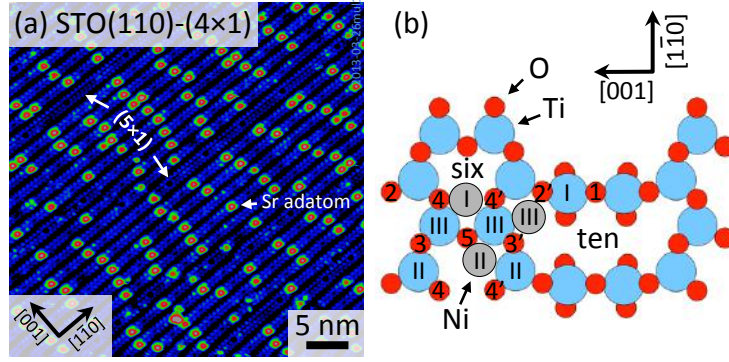


FIGURE 3.18.: (a) STM image of the SrTiO₃(110)-(4×1) surface. Labeled are Sr adatoms as well as a few lines of (5×1) reconstruction. (b) Top view of the SrTiO₃(110)-(4×1) surface. Ti and O atoms are shown in blue and red, respectively. Ni adatoms (grey) adsorbed at bridging sites between surface oxygen atoms are indicated by labels (I)-(III). STM tunneling parameters: $U_S = +2.0$ V, $I_t = 0.3$ nA

3.3.1. Adsorption of Ni adatoms in STM

The (4×1) reconstruction of SrTiO₃(110) serves as an adsorption template. Figure 3.18(a) shows an STM image of the pristine surface. The surface is mostly (4×1) reconstructed with some lines of (5×1). As discussed above in Section 3.1.1, the protrusions (red) on the surface are intrinsic Sr adatoms. Figure 3.18(b) shows the (4×1) structure model with different surface O atoms (red) indicated by Arabic numbers. Surface Ti atoms (blue) and most favorable Ni adsorption sites (gray) are labeled with Roman numerals. The six- and ten-member rings of corner-sharing TiO₄ tetrahedra on this surface act as nano-pores, which help to stabilize single Ni adatoms. The 6-member ring has a diameter of around 5.5 Å and also acts as an adsorption site for single Sr adatoms [71]. Nickel metal was deposited from an electron beam evaporator with a typical growth rate of 0.1 Å per minute. The growth rate was measured *in-situ* with a home-built quartz-crystal microbalance.

Figure 3.19(a) shows the surface after deposition of 0.01 Å Ni at RT. In addition to the intrinsic Sr adatoms (white arrows), bright features are observed either centered within the (4×1) rows (blue arrows), or at the side of the rows (red arrows). These features occupy exclusively these center (side) positions, and exhibit an apparent height of approximately 136 ± 17 pm (157 ± 16 pm). In contrast, the

3. Results

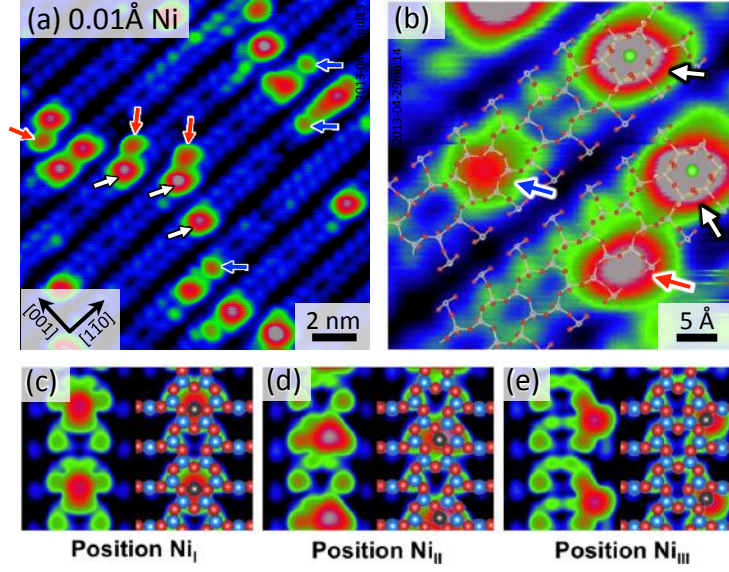


FIGURE 3.19.: (a) STM image of 0.01 Å Ni deposited on the SrTiO₃(110) surface at RT. Marked with arrows are Sr atoms (white), and Ni atoms at the center (blue) and side (red) positions. (b) High-resolution STM image with a structural model superimposed. (c)-(e) DFT-simulated STM images of single Ni adatoms adsorbed at the centered Ni_I (c), off-center Ni_{II} at the side of the six-member ring (d), and at Ni_{III} at the side of the row in a ten-member ring (e). STM tunneling parameters: $U_S = +2.0$ V, $I_t = 0.3$ nA

intrinsic Sr adatoms have an apparent height of ~ 240 pm. We therefore conclude that each of these protrusions contains only one Ni atom. In addition, Ni adatoms prefer to adsorb close to the Sr adatoms, see Figure 3.19(a).

By superimposing a structural model on a high-resolution STM image, we can identify the possible adsorption sites of Ni adatoms within the nano-pores of the (4×1) reconstruction. The center position is close to the bridge site between O4 and O4', indicated by the blue arrow in Figure 3.19(b), whereas the side position is close to the bridge site between O3 and O2 (red arrow).

DFT calculations were performed in order to verify the adsorption of Ni at different sites in the (4×1) unit cell and to determine the corresponding adsorption energies. Ni adsorbed at the centered Ni_I site [Figure 3.19(c)] represents the most stable adsorption configuration, followed by the Ni_{III} and Ni_{II} positions. The corresponding energies of the adsorbed Ni referenced to a Ni atom in the bulk fcc

3. Results

configurations	I	II	III
$E - E_{\text{Ni}}^{\text{bulk}}$ (eV/Ni atom)	1.11	1.49	1.38
$E - E_{\text{Ni}}^{\text{gas}}$ (eV/Ni atom)	-3.38	-3.0	-3.1
Ni-O bonding length (Å)	1.790, 1.790	1.828, 1.839	1.819, 1.832
bonding angle (°)	172	162	168
height (Å)	0.801	0.468	0.596
magnetic moments (μ_{B})	0.484	0.927	0.21
Bader charge	+0.30	+0.60	+0.20

TABLE 3.2.: Characterization of adsorption configurations of Ni adatom on the $\text{SrTiO}_3(110)$ -(4×1) surface. Listed are the energy of the adsorbed Ni E_{ads} , referenced to bulk Ni and Ni in the gas phase, respectively, Ni-O bond length and O-Ni-O bond angles, the height of the Ni atom compared to the plane of the Ti_{I} atoms of the pristine surface, the magnetic moment, as well as the Bader charge analysis for Ni adatoms in the three configurations shown in Figure 3.18. Details about the calculation can be found in ref. [93].

lattice (or in the gas phase) are 1.1 (-3.4) eV for Ni_{I} , and ~ 0.3 eV less favorable at Ni_{III} and Ni_{II} sites (see Table 3.2). Figures 3.19(c)-(e) show STM simulations of Ni at the most favorable sites. Simulated STM images agree very well with the experimental ones thus verifying the assignment of center and side positions to Ni_{I} and Ni_{III} sites, respectively.

Figure 3.20(a) shows the surface after deposition of 0.05 Å Ni. Still, single adatoms (blue and red arrows) are found on the surface near intrinsic Sr adatoms (white arrows). Statistics over a series of STM images shows that the preferential adsorption site has changed from the center position (blue arrows) at low coverages to the side position (red arrows) at higher coverage, see Figure 3.20(c). In addition, features with an apparent height ranging from 350 to 650 pm are present on the surface. These features appear along the meandering lines of intrinsic Sr adatoms

3. Results

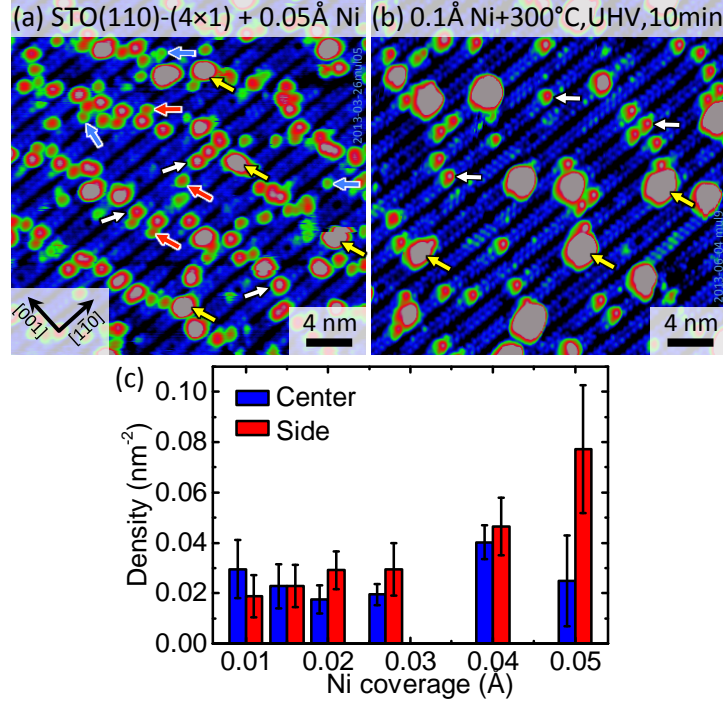


FIGURE 3.20.: (a) STM image ($U_S = +1.6 \text{ V}$, $I_t = 0.4 \text{ nA}$) of 0.05 \AA Ni deposited on the $\text{SrTiO}_3(110)-(4 \times 1)$ surface at RT. (b) The surface after mild post-annealing of 0.1 \AA Ni deposited at RT. Marked with arrows are intrinsic Sr adatoms (white), Ni adatoms adsorbed at centered Ni_I (blue) and side Ni_{III} (red) positions, and Ni clusters (yellow). (c) Histogram of the density of Ni adatoms adsorbed at center and side positions for various Ni coverages. Error bars correspond to 1σ standard deviation.

3. Results

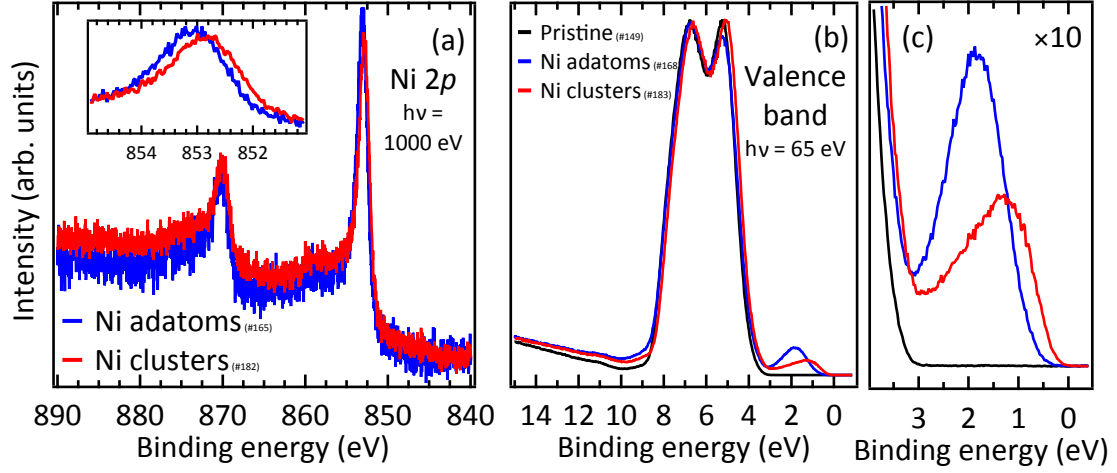


FIGURE 3.21.: (a) Ni 2p core-level photoemission spectra after deposition of 0.1 Å Ni (red) onto the SrTiO₃(110)-(4×1) surface, and after mild annealing (~300°C, UHV, 10 min) to form clusters (blue). The inset shows the Ni 2p_{3/2} feature to emphasize the shift of ~0.2 eV. (b) Valence-band photoemission spectra of the clean surface (black) and the surface with 0.1 Å Ni (blue) and Ni clusters (red). Panel (c) shows the in-gap states located at 1.9 eV (adatoms) and 1.3 eV (clusters) below E_F . All spectra were taken at RT.

and are therefore attributed to Ni atoms or small Ni clusters adsorbed on the Sr adatoms (yellow arrows). Similar clusters appear after mild annealing of a surface with 0.1 Å Ni to 300 °C in UHV for 10 min. This treatment leads to sintering of all Ni adatoms on the surface into clusters with an apparent height of ~600 pm, see Figure 3.20(b). Apart from the clusters, the remaining surface very much resembles the pristine surface prior to deposition.

3.3.2. Adsorption of Ni adatoms in PES

Figure 3.21(a) shows Ni 2p core-level photoemission spectra after deposition of 0.1 Å Ni on the SrTiO₃(110)-(4×1) surface. The blue spectrum originated from Ni adatoms and some Ni clusters, while the red spectrum was acquired after mild annealing the sample (~300°C, UHV, 10 min) and therefore sintering of the adatoms into clusters. Both spectra resemble the typical Ni 2p line shape of

3. Results

metallic Ni [94]. The Ni $2p$ core-level spectrum exhibits a binding energy of the $j=3/2$ component of 853.1 ± 0.3 eV and a 17.3 eV spin-orbit-split (SOS) $2p_{1/2}$ peak. These values are close to the ones reported for pure metallic Ni with $E_B=852.7$ eV of the $2p_{3/2}$ peak and a SOS of 17.3 eV [95]. The main Ni $2p_{3/2}$ spectral feature is shifted by ~ 0.2 eV to lower binding energies for the clusters, see inset of Figure 3.21(a). Note, however, that the uncertainty of these binding energies is in the same order of magnitude.

Figure 3.21(b) shows valence-band photoemission spectra of the pristine (4×1) surface (black), the surface after deposition of 0.1 Å Ni adatoms (blue), and after sintering of the 0.1 Å Ni into clusters (red). The spectrum of the pristine surface shows the O $2p$ -derived valence band in the binding energy range of 4–8 eV. The onset of the VB is located approximately 3.2 eV below the Fermi level, similar to what we reported in Section 3.2.2. In addition, the pristine surface does not show any density of states inside the band gap [see Figure 3.21(c)]. Upon deposition of 0.1 Å Ni, the whole valence band spectrum shifts to lower binding energies, and an in-gap state with a binding energy of 1.9 eV is formed (blue curve). Interestingly, this in-gap state changes in position and intensity when the Ni adatoms are sintered into clusters. For the Ni clusters, the IGS is located at a binding energy of ~ 1.2 eV.

3.3.3. Summary and discussion: Ni adatoms and clusters on $\text{SrTiO}_3(110)-(4 \times 1)$ surface

The adsorption of Ni adatoms, and Ni clusters on the $\text{SrTiO}_3(110)-(4 \times 1)$ surface has been investigated with STM, PES, and DFT. Single Ni adatoms are stabilized on the reconstruction network with two distinct adsorption configurations observed in STM (centered within the (4×1) rows, and on their sides). The preferential adsorption at these sites has been confirmed by DFT. Mild annealing ($\sim 300^\circ\text{C}$, UHV, 10 min) results in sintering of the adatoms into clusters.

PES of the valence band reveals a state at $E_B = 1.9$ eV in the band gap formed upon adsorption of Ni adatoms (+ a few clusters), which shifts to about 1.2 eV upon sintering of the Ni adatoms into clusters. In addition, adsorption of Ni adatoms is associated with a rigid shift of all spectral features to lower binding

3. Results

energies, *i.e.*, upward band bending. DFT predicts a higher adsorption energy for the center position (Ni_I) compared to the side position (Ni_III). This behavior is also observed at the lowest deposition amounts analyzed (0.01 \AA Ni), while at higher coverages, the side position is more often occupied. A simple explanation for this behavior can be rationalized by the fact that within the (4×1) unit cell, two side positions are available, but only one center position.

Interestingly, the measured apparent heights for Ni adatoms adsorbed at Ni_I ($136 \pm 17 \text{ pm}$) and Ni_III ($157 \pm 16 \text{ pm}$) sites are in contrast to the calculated heights (with respect to the Ti_I atoms in the (4×1) troughs) of Ni atoms in Ni_I ($\sim 0.8 \text{ \AA}$) and Ni_III ($\sim 0.6 \text{ \AA}$) positions. This could indicate a different electronic structure of the two adsorption configurations. It is also interesting that all calculated adsorption energies are positive with respect to a Ni atom in its bulk fcc lattice. This implies that it is thermodynamically more favorable for Ni to form clusters on the $\text{SrTiO}_3(110)$ surface, which is also observed in STM – Ni adatoms sinter into clusters upon mild annealing. Still it is remarkable that Ni adsorbs as single adatoms, and the reconstruction network kinetically hinders the formation of clusters at RT. Therefore we conclude that the nano-pores of the $\text{SrTiO}_3(110)$ - (4×1) surface play an important role for anchoring and stabilizing single adatoms.

The origin of in-gap states (IGS) in valence-band photoemission spectra of SrTiO_3 is still under debate. Often these states appear at a binding energy of $\sim 1.3 \text{ eV}$ (compare IGS presented in Section 3.2.2, which were formed through electron doping with atomic hydrogen or oxygen vacancies). In these cases, the IGS is accompanied by a downward band bending indicating electron confinement in the near-surface region [33]. However, the IGS observed upon adsorption of Ni adatoms is different from the ones mentioned above. On the surface with Ni adatoms, the IGS is located at $\sim 1.9 \text{ eV}$ instead of 1.3 eV binding energy. The energy bands appear to bend upward upon the adsorption of Ni, as seen in the valence band (Figure 3.21) and O $1s$ spectra (Figure 3.22). In addition, the position and shape of the IGS is clearly different for Ni adatoms and Ni clusters, indicating that the IGS originates from the deposited Ni on the surface. However, it should be mentioned that the photon energies at the synchrotron experiments (due to a

3. Results

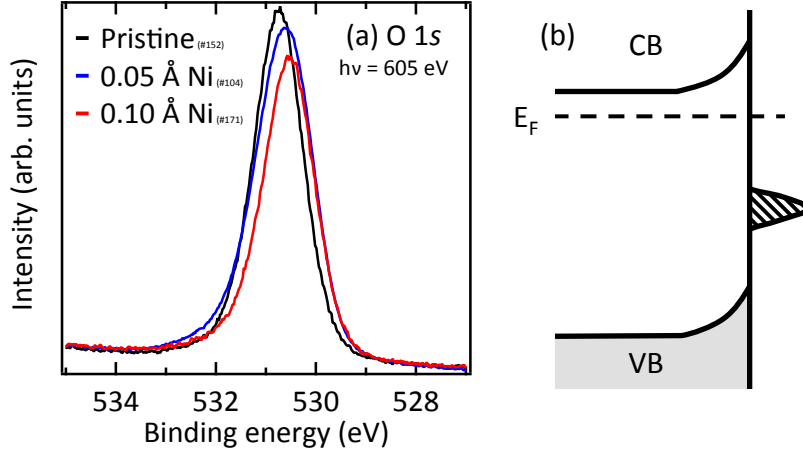


FIGURE 3.22.: (a) Comparison of O 1s core-level photoemission spectra of the clean surface (black) and the surface with 0.05 Å (blue) and 0.1 Å (red) Ni adatoms. The spectra are shifted by 0.2 eV to lower binding energy after deposition of Ni. (b) Schematic energy diagram showing the upward band bending and the in-gap state induced by the adsorption of Ni adatoms.

lack of systematic calibration) are not as well-defined as the photon energy of the lab source. Absolute positions of photoemission features are therefore not fully reliable.

To further understand the origin of the IGS and the associated band bending, we have calculated the density of states (DOS) for the most stable Ni_I configuration, see Figure 3.23. In line with photoemission data, DFT predicts states just above the valence band within the band gap. These states mainly originate from Ni 3d orbitals and are located at the surface. Because they lie below the Fermi level (dashed line in Figure 3.23), electrons from Nb dopant atoms in the SrTiO₃ layers can occupy these surface states, and an upward band bending occurs [as visible in the shift of the VB and O 1s in Figures 3.21(b) and 3.22(a), respectively].

Regarding the reactivity of single adatoms on oxide supports, the charge state of the adatoms plays an important role. In the case of Au metal adatoms, it was shown theoretically that charging of the Au adatoms reduces the adsorption energy of small molecules as well as activation barriers for selected reactions [96].

The results presented above might suggest that Ni adatoms are negatively

3. Results

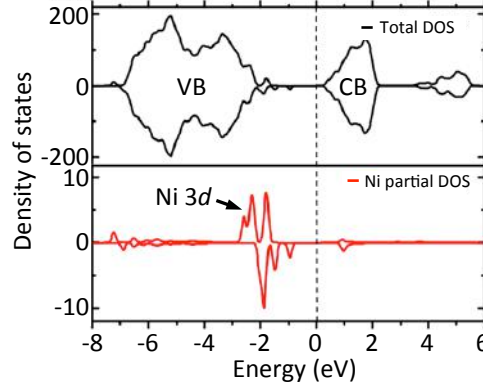


FIGURE 3.23.: Valence and conduction band density of states of the Ni_I adatom on the $\text{SrTiO}_3(110)-(4\times 1)$ surface. The upper and lower panels show the total and Ni partial density of states, respectively. More information on computational details are found in ref. [93].

charged. However, the Ni $2p$ spectrum for the adatoms is shifted to higher binding energies, as compared to the spectrum for the clusters. This would suggest a positive charge on the Ni adatoms. Note that final state effects in core-level PES could as well lead to such a shift [97]. In addition, the Bader charge analysis for the Ni atom in the preferred configurations Ni_I - Ni_III reveals positively charged Ni adatoms. The calculated Bader charges of Ni adatoms at positions Ni_I and Ni_III amount to +0.3 and +0.2, respectively, therefore supporting the assignment of positive charge to Ni adatoms. However, it should be mentioned that the DFT calculations did not consider the n-type doping of the STO crystals.

3.4. NiO clusters on the $\text{SrTiO}_3(110)-(4\times 1)$ surface

This section presents results about the adsorption of NiO clusters on the (4×1) surface, and the dissociation of water on the NiO-modified surface. Water dissociation at surfaces is especially relevant in the field of solar energy conversion. H_2 is a clean fuel, which can be transformed into electrical power by electrochemical devices such as solid oxide fuel cells. However, large-scale H_2 production is

3. Results

often realized by reforming of natural gas, although molecular hydrogen can be produced by water splitting reactions (electrolysis). By utilizing solar light for this reaction, *i.e.*, in heterogeneous photo-electrolysis, the production of H₂ fuel becomes a clean alternative to natural gas and oil [98]. Fujishima and Honda were the first to report the electrochemical photolysis of water over a TiO₂ electrode [99], and Mavroides *et al.* reported on the photoelectrolysis of water in cells with SrTiO₃ [26]. After the first discovery of the photocatalytically active system NiO-SrTiO₃ [100], only recently there has been progress in understanding the role of the co-catalyst NiO [101]. In their study, Townsend *et al.* explain the activity of the system in terms of a three-component catalysis, “in which STO absorbs the light, Ni reduces protons, and NiO oxidized water”. In order to gain additional information on the system from a surface-science perspective, we performed experiments on the system NiO-STO, and studied the adsorption of NiO clusters on the SrTiO₃(110)-(4×1) surface and their interaction with H₂O by means of LEED, STM, XPS, UPS, NEXAFS, and LEIS. The results of this study have been published in ref. [102].

3.4.1. NiO cluster on (4×1) in XPS/UPS

Ni metal has been oxidized into NiO clusters in two ways. In the experiments carried out at the Maxlab synchrotron facility (XPS, UPS, and NEXAFS), Ni metal has been deposited in UHV (from an electron-beam evaporator) and has subsequently been post-oxidized (PO) in 5×10^{-6} mbar of O₂ slightly below the onset of the infra-red (IR) pyrometer ($T \sim 300^\circ\text{C}$). The resulting Ni 2*p* core level was used as a measure of the oxidation state of the deposited Ni, see Figure 3.24(c). For the STM, XPS, and LEIS experiments in the lab at TU Wien, NiO clusters have been created by reactively depositing sub-monolayer amounts of Ni metal in an O₂ pressure of 5×10^{-6} mbar at different temperatures (RT, $\sim 300^\circ\text{C}$, and 355°C). All thicknesses stated below are referred to the total amount of Ni metal deposited before oxidation.

As discussed in Section 3.3, the (4×1) surface supports the adsorption of single Ni adatoms. We studied the electronic structure of Ni adatoms (+ some clusters)

3. Results

and NiO clusters adsorbed on the SrTiO₃(110)-(4×1) surface. Figure 3.24 shows valence-band and core-level photoemission spectra (acquired at RT) of the pristine SrTiO₃(110)-(4×1) surface (black), the surface with 0.1 Å Ni deposited at RT (red), and after post-oxidizing the Ni into NiO at 300 °C (blue). For comparison, the zoomed VB-spectra in Figure 3.24(b) were aligned to the O 2s peak at $E_B \approx 22$ eV (not shown). For the spectra in the insets of panel (d) and (e), the main spectral features of O 1s and Ti 2p, respectively, were aligned. The onset of the valence band was determined from the intersection of the x -axis with a straight tangent to the leading edge of the valence band feature, as indicated by the dashed lines in the Figure 3.24(b). Similar to the findings in Section 3.3.2, the onset of the valence band for the pristine surface is located ~ 3.2 eV below the Fermi level, and there are no states in the band gap.

As reported in Section 3.3, the evaporation of Ni results in a rigid shift of all spectra features to lower binding energies (upward band bending), and the formation of an in-gap state located at a binding energy of ~ 1.9 eV. The Ni 2p_{3/2} core-level feature exhibits a binding energy of 853.6 ± 0.3 eV (SOS = 17.3 eV), see Figure 3.24(c). Post-oxidation of the adsorbed Ni considerably changes the core-level photoemission spectrum. The Ni 2p feature changes to the typical NiO line shape, with a binding energy of the $j = 3/2$ component of 855.9 ± 0.3 eV and a SOS of 17.6 eV, see Figure 3.24(c). These values are in good agreement with literature values of $E_B = 853.8$ eV of the 2p_{3/2} peak and a SOS of 17.5 eV for bulk NiO [95]. Upon post-oxidation, the valence band shifts to even lower binding energies, as compared to the surface after adsorption of Ni adatoms. In addition, the in-gap state (IGS) of Ni adatoms at ~ 1.9 eV binding energy transforms into a shoulder of the valence band. This shoulder results in an apparent change of the onset of the valence band to binding energies of around 1.7 eV below the Fermi level, see Figure 3.24(b).

The O 1s core-level shows only a very weak change. The adsorption of Ni adatoms causes the main O 1s spectral feature to be damped and a small shoulder at higher binding energy is formed. This shoulder is slightly diminished upon oxidation, see inset of Figure 3.24(d).

3. Results

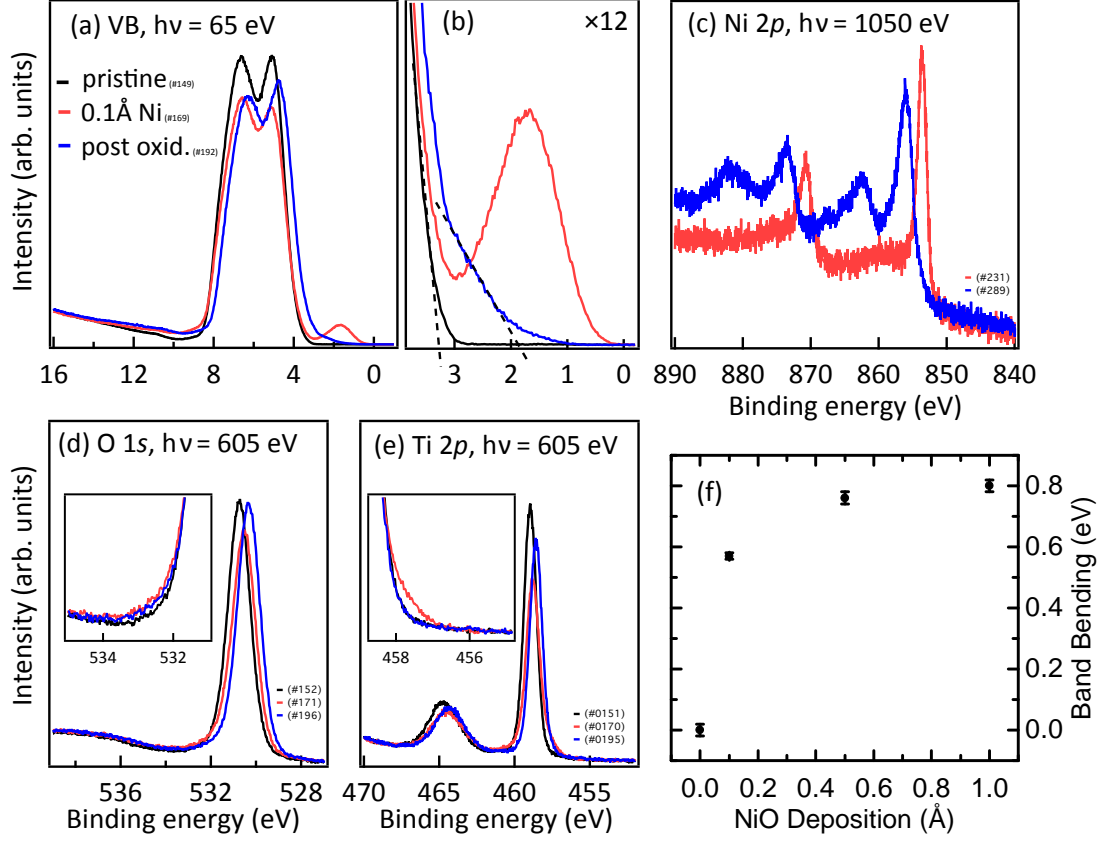


FIGURE 3.24.: Photoemission spectra of differently treated SrTiO₃(110)-(4×1) surfaces. Black, red, and blue spectra correspond to the pristine surface, the surface after deposition of 0.1 Å Ni, and after postoxidizing the same amount of Ni at 300 °C, respectively. (a) Valence band (VB) spectra. (b) A zoom into the gap region with the spectra aligned to the O 2s feature at $E_B = 22$ eV. Dotted lines are used to evaluate the onset of the VB. (c) Ni 2p core levels before and after oxidizing 0.1 Å Ni. (d) O 1s and (e) Ti 2p core-level features. The insets show the O 1s high binding-energy region (d) and the Ti 2p_{3/2} low binding-energy region (e) after aligning the spectra to the corresponding main peak. (f) Band bending as determined from the O 1s and Ti 2p peak positions with Al K α radiation as a function of the amount of NiO deposited by RD at 355 °C. Error bars represent 99% confidence intervals on the fitted peak positions.

3. Results

The Ti 2*p* core-level shows for the pristine surface the commonly observed Ti 2*p* feature of Ti⁴⁺ ions (Ti 2*p*_{3/2} $E_B = 459 \pm 0.15$ eV with SOS of 5.7 eV). Adsorption of Ni adatoms (+ clusters) results in the formation of a small shoulder at lower binding energies, see inset of panel (e). This shoulder indicates charge transfer from the Ni to the Ti to form Ti³⁺, indicating a positive charge state of the adsorbed Ni (compare discussion in Section 3.3.3). Upon oxidation, this shoulder vanishes, and the spectrum resembles the pristine surface, except for a rigid shift of 0.2 ± 0.15 eV.

Because photon energies have not been calibrated thoroughly at synchrotron experiments, the absolute positions of PES features are not fully reliable. We therefore repeated the XPS measurements at the lab at TU Wien utilizing an Al K α X-ray source producing photons with a constant, reliable energy. Figure 3.24(f) shows the values of band bending, as determined from the shift of core-level features (O 1*s* and Ti 2*p*), depending on the NiO deposition amount. The energy bands progressively bend with increasing NiO deposition amount to lower binding energies (upward band bending), with a saturation value of ~ 0.8 eV at deposited amounts of 1 Å NiO.

3.4.2. NiO clusters on the (4×1) surface in STM

Figure 3.25 shows STM images of the pristine SrTiO₃(110)-(4×1) surface (a), the surface after adsorption of 0.05 Å Ni adatoms (+ a few clusters) (b), and the surface with differently prepared NiO clusters (c)-(f). Intrinsic Sr adatoms, and Ni adatoms are indicated by white, and blue and red arrows, respectively. NiO clusters are highlighted by dashed blue lines, and defects are indicated by orange lines and orange arrows.

As already reported above, Ni adsorbs as single adatoms and small clusters on this surface [see Section 3.3 and Figure 3.25(b)]. Upon post-oxidation of 0.1 Å Ni in 5×10^{-6} mbar O₂ at 375 °C, the Ni forms irregularly shaped clusters [dashed blue lines in panels (c)-(f)]. These clusters extend over several adjacent (4×1) lines, and do not exhibit any preferential adsorption site. In addition, these patches do not show any ordering on the atomic scale, likely indicating a locally defective NiO

3. Results

or a mixed $\text{Sr}_x\text{Ti}_y\text{Ni}_z$ structure. Similar morphological features are observed when the growth is carried out by reactively depositing Ni in a pressure of 5×10^{-6} mbar O_2 at 325 °C (d).

Increasing the amount of NiO on the surface does not improve the atomic-scale ordering of the NiO patches, see Fig. 3.25(e). Increasing the amount of NiO on the surface only increases the areal coverage of NiO patches. Upon deposition of 0.3 Å NiO (not shown), the surface is nearly fully covered, with only little of the original (4×1) surface visible in STM. LEED images acquired on the sample at different NiO coverages (not shown) do not exhibit any additional features in the diffraction pattern. Only an overall increase of the inelastic background in LEED is observed for increasing deposition amounts.

Note that local distortion of the (4×1) rows in close proximity to the NiO clusters is observed in STM images. This is mostly evident wherever NiO patches extend up to the dark trenches separating adjacent (4×1) rows [orange arrows in Figures 3.25(c) and (d)]. In such regions the dark trenches appear wider in the in-plane direction, and exhibit a deeper corrugation by 10–20 pm, as measured with STM.

Fig. 3.25(f) shows the surface with 0.1 Å NiO post-oxidized at 600 °C. The NiO clusters coalesced into rectangularly shaped islands, along with several defects being introduced in the STO substrate (orange lines). One type of defect appears as periodic, bright dots centered within the (4×1) rows. Another type of defect appears as cross-shaped vacancies centered on one of the two rows of periodic dots that build up the (4×1) structure. The third obvious defect appears in STM images as depressions next to NiO patches and could indicate locally missing units of the surface reconstruction. It should be mentioned that despite the relatively high annealing temperature of 600 °C during post-oxidation, the XPS intensity ($\text{Al K}\alpha$) of the Ni 2*p* core-level decreases by less than 6 %. Therefore, extended inter-diffusion of Ni into the STO surface layer or bulk can be excluded.

3. Results

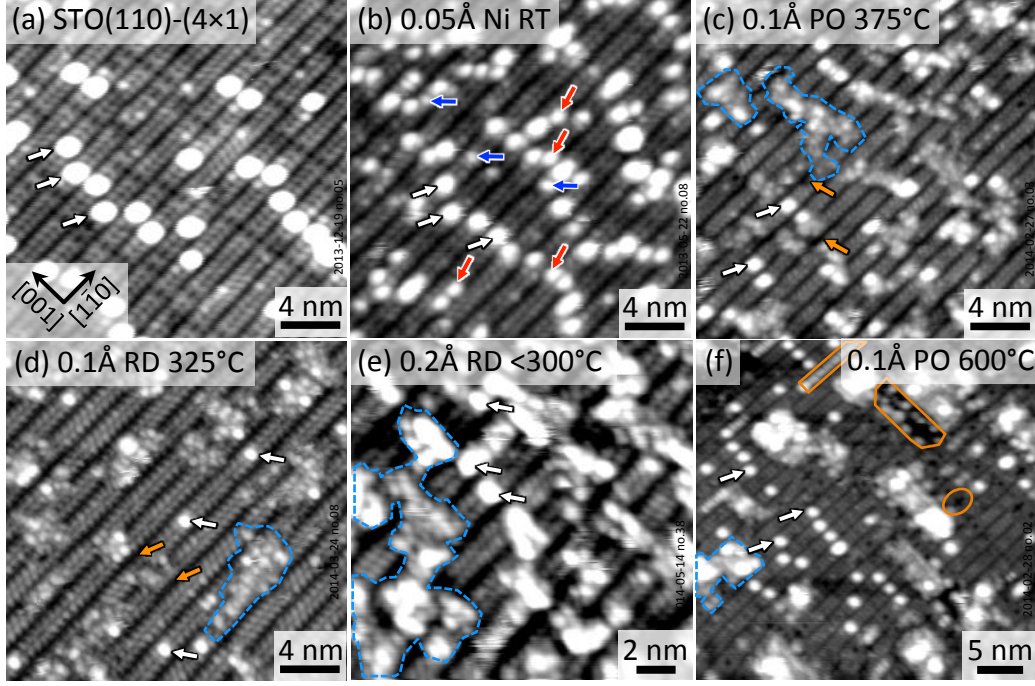


FIGURE 3.25.: STM images of differently treated $\text{SrTiO}_3(110)-(4\times 1)$ surfaces. White arrows indicate Sr adatoms. Blue and red arrows indicate Ni adatoms adsorbed at center and side positions, respectively (*cf.* Section 3.3). Dashed blue curves highlight selected NiO regions. Orange solid lines and orange arrows indicate defects. (a) Pristine (4×1) surface. (b) Pristine surface after deposition of 0.05 \AA Ni. [93] Panels (c) and (d) show 0.1 \AA Ni postoxidized (PO) and reactively deposited (RD), respectively. (e) Reactively deposited 0.2 \AA Ni. (f) 0.1 \AA Ni after postoxidation at 600°C . Tunneling parameters for panels (a)-(f): $U_S = +2.0$ to $+2.5 \text{ V}$, $I_t = 0.02$ to 0.3 nA .

3.4.3. NiO cluster on (4×1) in NEXAFS

To obtain further insight into the adsorption of NiO cluster on the $\text{SrTiO}_3(110)-(4\times 1)$ surface, we performed near-edge X-ray absorption fine structure (NEXAFS) measurements. As discussed in the experimental Section 2.2 and in Section 3.7, NEXAFS probes the unoccupied conduction band states (Ti $3d$) and gives valuable information about the local coordination of the probed atoms. We performed NEXAFS in the surface sensitive Auger electron yield (AEY) mode, and in the more bulk sensitive secondary electron yield (SEY) mode. Figure 3.26(a) shows the NEXAFS spectra of the Ti $L_{2,3}$ absorption edged of differently treated $\text{SrTiO}_3(110)-(4\times 1)$ surfaces.

The assignment of absorption features in Ti L-edge spectra of the (4×1) surface, and the differences between L-edge spectra acquired in AEY and SEY mode have been presented above in Section 3.1.1. The absorption peaks at photon energies of ~ 458 eV and ~ 460 eV correspond to Ti ions in octahedral (O_h) coordination, and the peak at ~ 459 eV corresponds to Ti ions in tetrahedral coordination (T_d). Small shifts of the Ti $L_{2,3}$ peak at 458 eV occur for different treatments of the surface. These shifts cannot be explained by band bending (BB) since BB originates from a local difference in electrostatic potential and should therefore affect all core levels, and valence-band, and conduction-band states equally. The shifts are therefore attributed to changes in the conduction band, *i.e.*, in the Ti $3d$ levels. Overall, however, these shifts are below 0.2 eV, indicating that the conduction band states are only minimally altered upon adsorption. Compared to the spectrum of the pristine surface (black curve), the tetrahedral signature in the spectra is considerably decreased upon adsorption of Ni and NiO, see Figure 3.26(a). This could indicate that the signal from the surface TiO_4 gets damped by the adsorbates, or that the adsorbates effectively distort the TiO_4 tetrahedra. The latter possibility is consistent with the distortion and disruption of the surface structure, which was observed in STM on a surface with NiO annealed at 325–375 °C [see Figs. 3.25(c) and (d)] and 600 °C [see Fig. 3.25(f)], respectively. Ti $L_{2,3}$ NEXAFS spectra acquired in the bulk-sensitive secondary electron yield (SEY) mode [see gray spectrum in Figure 3.26(a)] show the same absorption peaks as in AEY with

3. Results

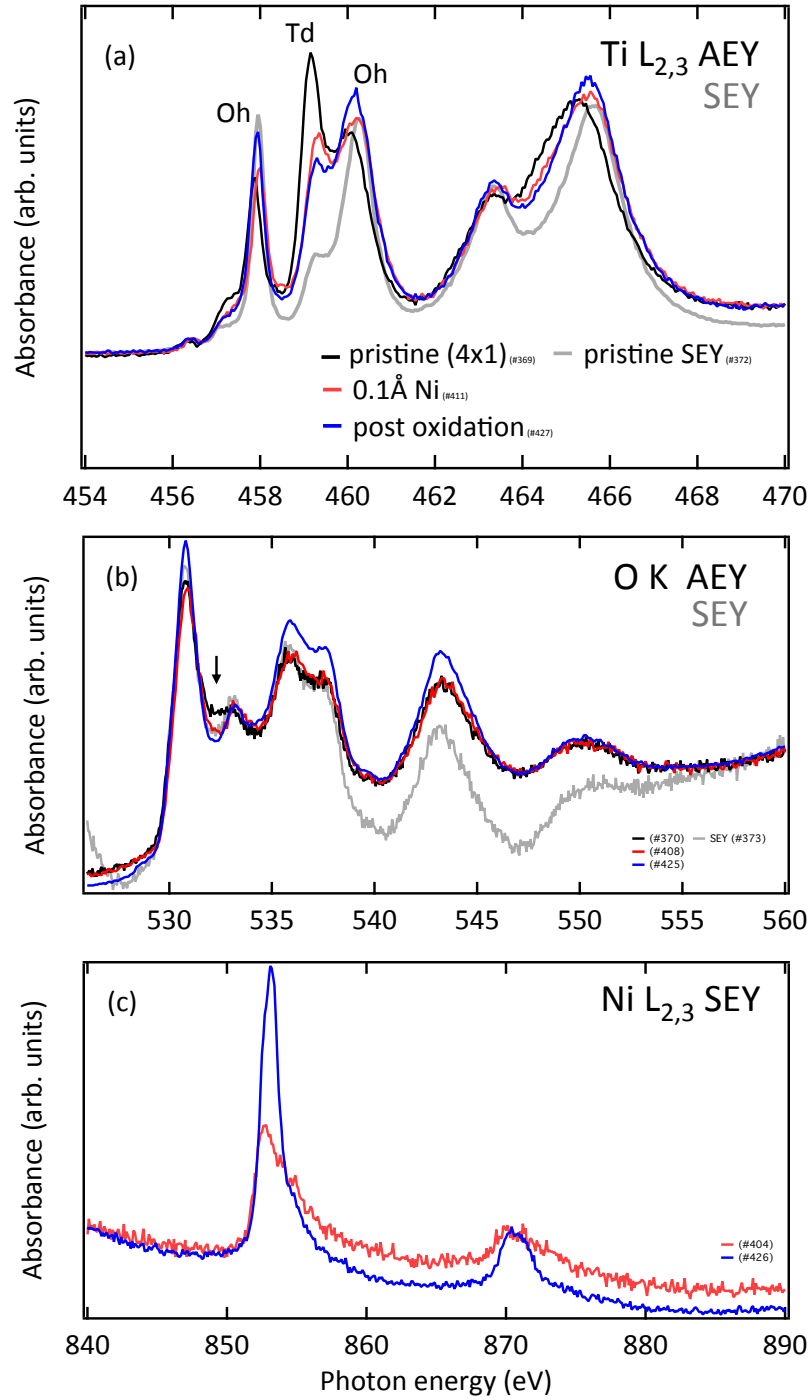


FIGURE 3.26.: X-ray absorption spectra of the pristine surface (black), the surface with 0.1 Å Ni (red), and after postoxidation to NiO (blue curve). (a) Ti $L_{2,3}$ absorption edge in Auger electron yield (AEY) mode and secondary electron yield (SEY) mode. Features related to Ti coordinated in tetrahedral or octahedral environment are indicated by Td and Oh, respectively. (b) O K edge in AEY and SEY. (c) Ni $L_{2,3}$ edge in SEY mode.

3. Results

the relative peak ratios dominated by the octahedral features, as expected for Ti in bulk STO.

Figure 3.26(b) shows the NEXAFS spectra of the O K edge. The spectrum appears similar for all surface treatments. De Groot *et al.* were able to relate the absorption spectrum of the O K edge of SrTiO₃ directly with the density of empty states [103]. According to their study, the first two absorption features at photon energies of ~530.8 eV and ~533.2 eV correspond to transitions from the O 1s into O 2p states hybridized with Ti 3d t_{2g} and e_g, respectively. At higher photon energies, the features relate to unoccupied states of Sr [103]. The spectrum of the pristine surface does show additional spectral weight at photon energies of ~532.2 eV. The separation of this additional peak [marked by the black arrow in Fig. 3.26(b)] from the main absorption feature at ~530.8 eV is comparable to the crystal field splitting observed in the Ti L_{2,3} edge absorption spectrum. We therefore conclude that this peak reflects the tetrahedral crystal field splitting of Ti 3d states for the pristine surface. The O K edge spectrum acquired in secondary electron yield exhibits the same features as the spectra acquired in AEY mode but with a different intensity for the peaks at photon energies of ~543.2 eV and ~550.6 eV.

The Ni L_{2,3} NEXAFS spectra for Ni adatoms and NiO clusters are shown in Figure 3.26(c). Due to a low signal related to the small amount of Ni or NiO on the surface, this spectrum was acquired in secondary electron yield (SEY). However, STM and XPS experiments revealed Ni to stay exclusively on the surface. Therefore, the use of SEY mode for the Ni L_{2,3} edge is not limiting the surface sensitivity of the measurement. The spectrum consists of two peaks at photon energies of ~853 eV and ~871 eV, corresponding to absorption of light by electrons in Ni 2p states. The position of these peaks and the shape of the spectrum is similar to the ones reported by May *et al.* for both metallic Ni and NiO samples [104]. In case of the post-oxidized samples typical features of the characteristic line shape of NiO are observed. The intensity of the L_{2,3} white lines with respect to the background is increased due to the oxidation of the metallic Ni, resulting in an increased number of empty d states for the oxidized Ni species [104].

3.4.4. Water interaction with NiO-modified SrTiO₃(110)-(4×1)

We have studied the interaction of H₂O with the NiO-loaded SrTiO₃(110)-(4×1) surface by means of UPS, XPS, and LEIS. As already mentioned in the experimental chapter, photoemission features allow us to identify whether water is adsorbed on the surface in a molecular or dissociative fashion. Figure 3.27 shows valence band and O 1s core level photoemission spectra before (blue) and after (green) dosing 50 Langmuir of H₂O on a (4×1) surface with 0.1 Å NiO. Increased spectral weight was observed in regions typically assigned to dissociatively adsorbed H₂O. In the valence band spectrum in Figure 3.27(a), a state at a binding energy of ~11 eV appears upon dosage of water. This peak is attributed to the OH 3σ state, indicating dissociated water on the surface, see Figure 3.27(b). In addition, Figure 3.27(c) shows a small increase of spectral weight inside the band gap, in line with the results presented in Section 3.2.2 for surface hydroxyls. Furthermore, the observation of an increased high-binding-energy shoulder of the O 1s core-level supports this conclusion, see inset of Figure 3.27(d). Although the photon energies (and therefore absolute binding energy values) were not well calibrated, all spectra exhibit a rigid shift to higher binding energies upon water dosing.

The adsorption of water has been further studied by means of low-energy ion scattering (LEIS). In addition to its high surface sensitivity, LEIS is able to resolve small mass differences of the surface atoms. By using He⁺ ions as the primary ions in LEIS, oxygen isotopes ¹⁶O and ¹⁸O can be discriminated in the resulting spectra. Figure 3.28 shows ion scattering spectra of differently treated SrTiO₃(110)-(4×1) surfaces. The spectrum of the pristine (4×1) surface (black curve) shows peaks related to He⁺ ions scattered at ¹⁶O (~400 eV), Ti (~710 eV), and Sr (~795 eV) atoms.

To investigate the adsorption of water on the NiO-loaded (4×1) surface, we performed LEIS after dosing up to 100 L isotopically labeled water (H₂¹⁸O). (H₂¹⁸O was dosed onto the samples in the preparation chamber to preserve the clean conditions in the analysis chamber.) Dosing up to 100 L H₂¹⁸O onto the pristine surface does not introduce any additional features in the LEIS spectrum (not shown),

3. Results

consistent with the inert nature of this surface, see chapter 3.2. We successively deposited increasing amounts of NiO onto the surface and subsequently dosed up to 100 L of H₂¹⁸O. (Each spectrum corresponds to a freshly prepared and treated surface.) Nickel introduces a peak in LEIS spectra at a kinetic energy of approximately 770 eV. This peak is partially overlapping with the corresponding peak of Sr and can only be distinguished from the Sr peak at higher NiO coverages ($> 0.2 \text{ \AA}$ NiO). In addition, a peak at a kinetic energy of $\sim 450 \text{ eV}$ is evolving in the spectra. This peak is assigned to He⁺ ions scattered at ¹⁸O belonging to adsorbed water. The spectra acquired on samples with different amounts of NiO clearly show that water binds to the NiO-loaded surface, in agreement with the photoemission data in Figure 3.27.

The ¹⁸O peak is larger for the case of 0.2 \AA NiO ($^{18}\text{O}/^{16}\text{O} = 12.3 \%$) compared to the case of 0.3 \AA NiO (8.5 %). Because 0.3 \AA NiO represents a nearly fully covered surface with only little (4×1) visible in STM, the larger peak at 0.2 \AA possibly indicates that H₂O either adsorbs or dissociates preferentially at the boundary of the NiO clusters with the (4×1) surface.

3.4.5. Summary and discussion: NiO and H₂O on SrTiO₃(110)-(4×1) surface

By combining various spectroscopic techniques with direct-space imaging, we have investigated the adsorption of NiO clusters on the SrTiO₃(110)-(4×1) surface and their interaction with water. The oxidation of Ni adatoms into NiO clusters has been achieved by either post-oxidizing adsorbed Ni, or by reactively depositing Ni in an oxygen atmosphere, and has been verified by XPS. UPS results revealed the formation of a shoulder of the valence band maximum (VBM) upon NiO adsorption. In addition, NEXAFS results showed relatively stable positions of the Ti L_{2,3} absorption peaks for the surface with and without NiO, indicating that the conduction band minimum (CBM) is not considerably changed. Assuming that the states contributing to this VBM shoulder are hybridized with O 2*p* states of the valence band, the shifted onset of the VBM combined with the stable position of the CBM indicates an effective decrease of the band gap of the system. The

3. Results

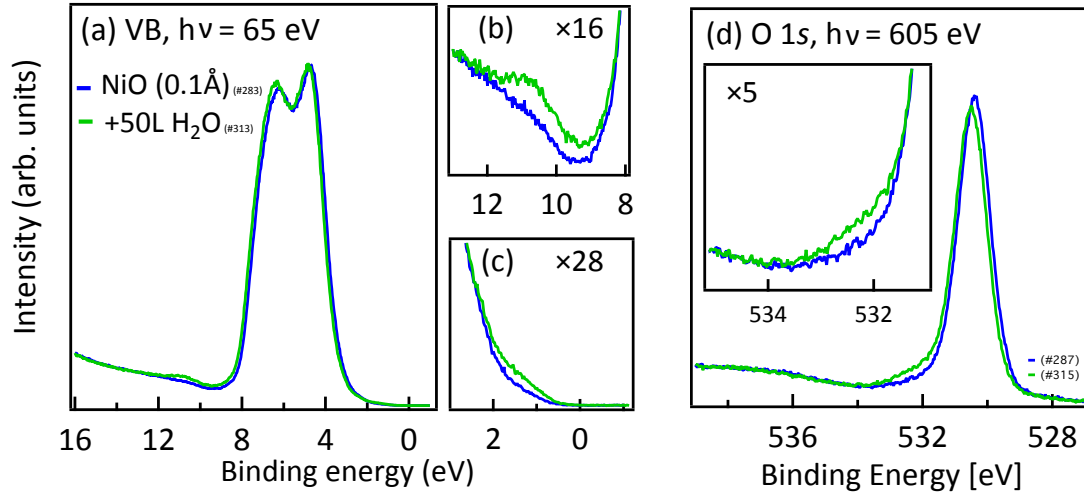


FIGURE 3.27.: (a) Valence band and (b) O 1s photoemission spectra of NiO-loaded surfaces before (blue) and after (green) dosing 50 L of water at RT. Panel (b) and (c) show a zoom into the OH 3σ and band-gap regions, respectively (spectra aligned to the O 2s peak at 22 eV). Inset of (d) shows the O 1s high binding-energy region after aligning the spectra to the main peak feature.

3. Results

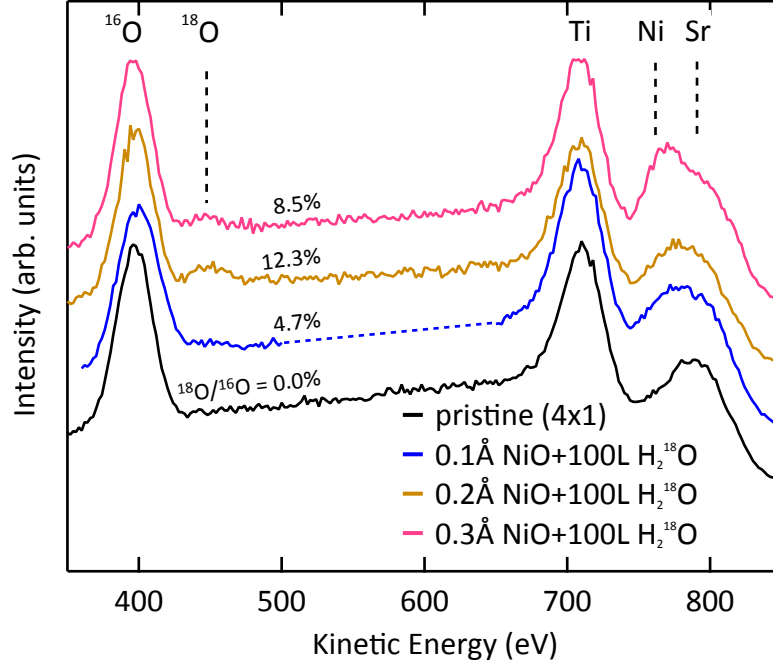


FIGURE 3.28.: Low-energy He^+ ion scattering spectra acquired on the pristine $\text{SrTiO}_3(110)-(4 \times 1)$ and after deposition of different amounts of NiO with subsequent dosing of 100 Langmuir H_2^{18}O . $^{18}\text{O}/^{16}\text{O}$ ratios were determined from peak fitting (Gaussian) after subtracting a linear background.

3. Results

bandgap decreases from 3.2 eV (photons with ~ 390 nm) to ~ 1.7 eV (~ 730 nm), allowing harvesting of visible light. It should be noted that the present data do not provide information on hybridization of these states. However, it is known from experiments with N-doped TiO_2 that such VBM shoulders can considerably enhance the visible-light response in photocatalysis experiments [105]. In addition, a considerable shift of PES features to lower binding energies by as high as 0.8 eV is observed for the NiO-modified surface. Such an upward band bending supports the dissociation of photogenerated excitons driving excited electrons toward the bulk of the substrate and holes to the very surface. It should be noted, however, that this process requires the existence of extended states necessary to allow charge transport before electron-hole recombination occurs.

The combination of STM and NEXAFS results indicates the disruption of the reconstruction network upon adsorption of NiO. Most likely the resulting defects represent favorable adsorption sites for water, which is also consistent with ion scattering results. LEIS shows a higher ^{18}O signal for the surface with 0.2 \AA NiO compared to the nearly fully covered surface with 0.3 \AA . This indicates that the adsorption may take place at the circumference of the NiO clusters, *i.e.*, at the triple phase boundary NiO/STO/UHV. XPS results indicated no interdiffusion of Ni, *i.e.*, the two oxide phases are well separated. It should be noted that the amount of reactively deposited Ni to form a nearly fully covered surface (0.3 \AA) approximately corresponds to 33 % of a single NiO(110) layer. This could indicate that the patches observed in STM are of a mixed Ni-Ti oxide phase. Such a mixed phase would change the local coordination of Ti in the surface layer, which is also observed in NEXAFS spectra. In Section 3.2, we discussed the idea about the inertness of the pristine surface being due to the regular nature of TiO_4 tetrahedra of the reconstruction. Therefore, the distortion or disruption of these tetrahedra could be a reason for the enhanced reactivity of the surface toward water adsorption.

3.5. Homoepitaxial growth of $\text{STO}(110)-(4\times 1)$ with PLD: Early stages of growth

In this section we present results from our pulsed laser deposition system with *in-vacuo* transfer of as-grown samples to the surface analysis chamber.

As already mentioned in Section 1.2, SrTiO_3 has evolved as a prototype for the class of complex oxides and we followed the homoepitaxial growth of STO on the (110) surface. Homoepitaxy provides the advantage of performing growth studies unaffected by misfit strain between substrate and film. In the following, we present results on the early stages of the homoepitaxial growth of the $\text{SrTiO}_3(110)-(4\times 1)$ surface. We show how the growth is influenced by the substrate temperature and pulse repetition rate. In addition, by combining highly resolved STM with RHEED-assisted PLD growth, we were able to test and expand the step density model that explains the variation of the RHEED specular spot intensity during growth.

Prior to growth we freshly prepared and characterized the substrate surface and ensured surface conditions for the pristine surfaces that are consistent for all depositions. A characterization of the pristine (4×1) surface by STM, LEED, and RHEED is presented above in Section 3.1.1. Details about the PLD setup are shown in Section 2.10. If not stated otherwise, all depositions were carried out in a background pressure of 3×10^{-2} mbar O_2 , with a UV laser (248 nm) fluence of 2 J/cm^2 , a target-to-substrate distance of ~ 60 mm, and a UV laser repetition rate of 1 Hz. Most of the results presented in this section have been published in ref. [106].

3.5.1. Island nucleation on the $\text{SrTiO}_3(110)-(4\times 1)$ surface

Figure 3.29(a) shows an STM image of ~ 0.1 ML grown on a (4×1) -reconstructed surface (substrate temperature = 850°C). The line profile shows an island height of ~ 276 pm, corresponding to the height of one ML. Intrinsic Sr adatoms are indicated by the white arrow in panel (a). Due to the relatively high O_2 pressure during deposition, the surface exhibits exclusively the type-II domain boundaries

3. Results

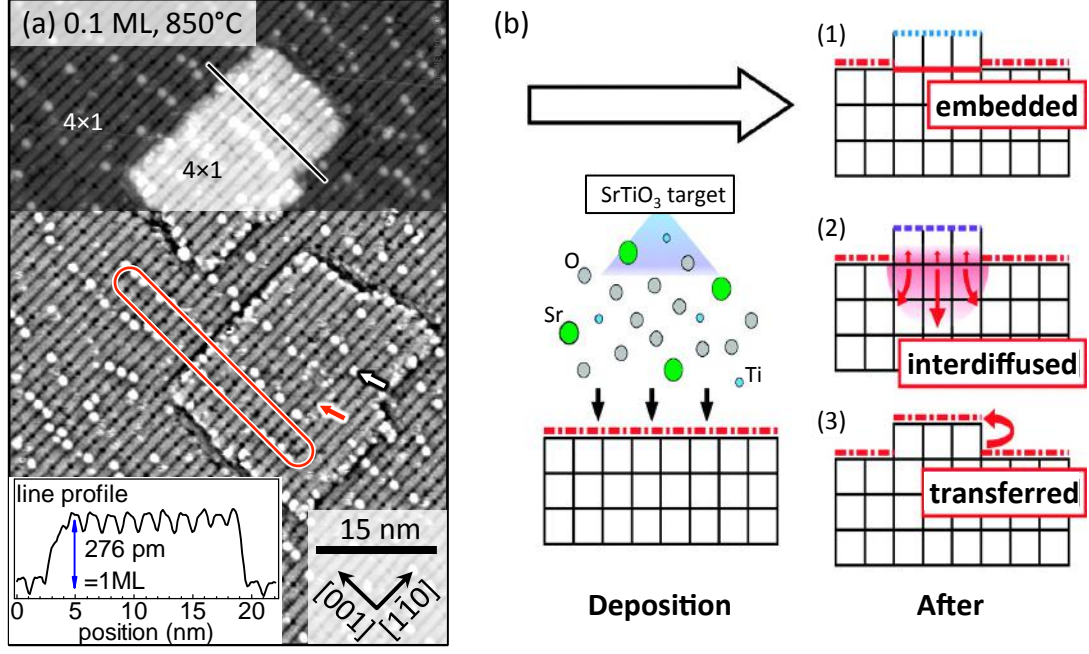


FIGURE 3.29.: (a) STM image of 0.1 ML on a (4×1) -reconstructed surface. The inset shows the height profile along the line. Intrinsic antiphase domain boundaries are highlighted by a white (Sr adatoms) and a red (type-II vacancy clusters) arrow. The lower part is high-pass filtered to emphasize the unperturbed arrangement of domain boundaries across the step edge (red line). (b) Schematic representation of different growth scenarios. (1) The surface reconstruction (red line) is buried underneath the film, which exhibits a different surface structure. (2) The initial surface structure intermixes with the film to form an interdiffusion region, again with the film exhibiting a different surface structure. (3) The film grows as a stoichiometric bulk layer and the surface structure is transferred to the top. Schematic adapted with permission from ref. [21]. © 2011 American Chemical Society. Deposition and STM parameters: (a) 2 J/cm^2 , $3 \times 10^{-2} \text{ mbar O}_2$; $U_S=3.3 \text{ V}$, $I_t=0.7 \text{ nA}$.

3. Results

(*cf.* Section 3.1.1), as indicated by the red arrow in panel (a). A high-pass filter is applied to the lower part of Fig. 3.29(a) highlighting the unperturbed arrangement of domain boundaries on the islands with respect to the substrate surface [highlighted by the red line in (a)]. The balance between compulsive interaction of anti-phase domain boundary (APDB) pairs along $[1\bar{1}0]$ direction, *i.e.*, between Sr adatoms and type-II vacancy clusters, and the attractive interaction between type-II vacancy APDBs along $[001]$ direction is therefore also continued across the step edges [71].

The islands exhibit the same reconstruction as the substrate layer. It has already been pointed out by Shimizu *et al.* that there are in general three scenarios to be considered regarding how a film grows on a reconstructed surface, see Figure 3.29(b) [21]. For example, the surface reconstruction can get completely buried underneath the deposited film, which then exhibits a different surface structure [panel (b1)]. Another possibility is that the deposited material effectively grows as subsurface stoichiometric bulk layers with the initial reconstruction floating to the topmost layer [panel (b3)]. An intermediate scenario might be possible as well, where the buried surface reconstruction intermixes with the film to form a different reconstruction at the top [panel (b2)].

The $\text{SrTiO}_3(110)-(4\times 1)$ in its equilibrium (4×10) superstructure (including both types of APDBs) exhibits a formal stoichiometry of $(\text{Sr}_{1/40}\text{Ti}_{58/40}\text{O}_{157/40})^{2-}$ [71]. It is therefore evident that the scenario shown in Fig. 3.29(b1) is not very probable as it would require the incoming flux of laser-ablated particles to be strongly Ti-rich. Additionally, the situation of having a double layer of (4×1) reconstruction seems to be very unlikely. We therefore expect that the existence of $\text{STO}(110)$ islands having the same reconstruction as the substrate layer indicates that deposited material, when having SrTiO_3 stoichiometry, effectively grows as bulk-like subsurface islands, as shown in Fig. 3.29(b3).

3. Results

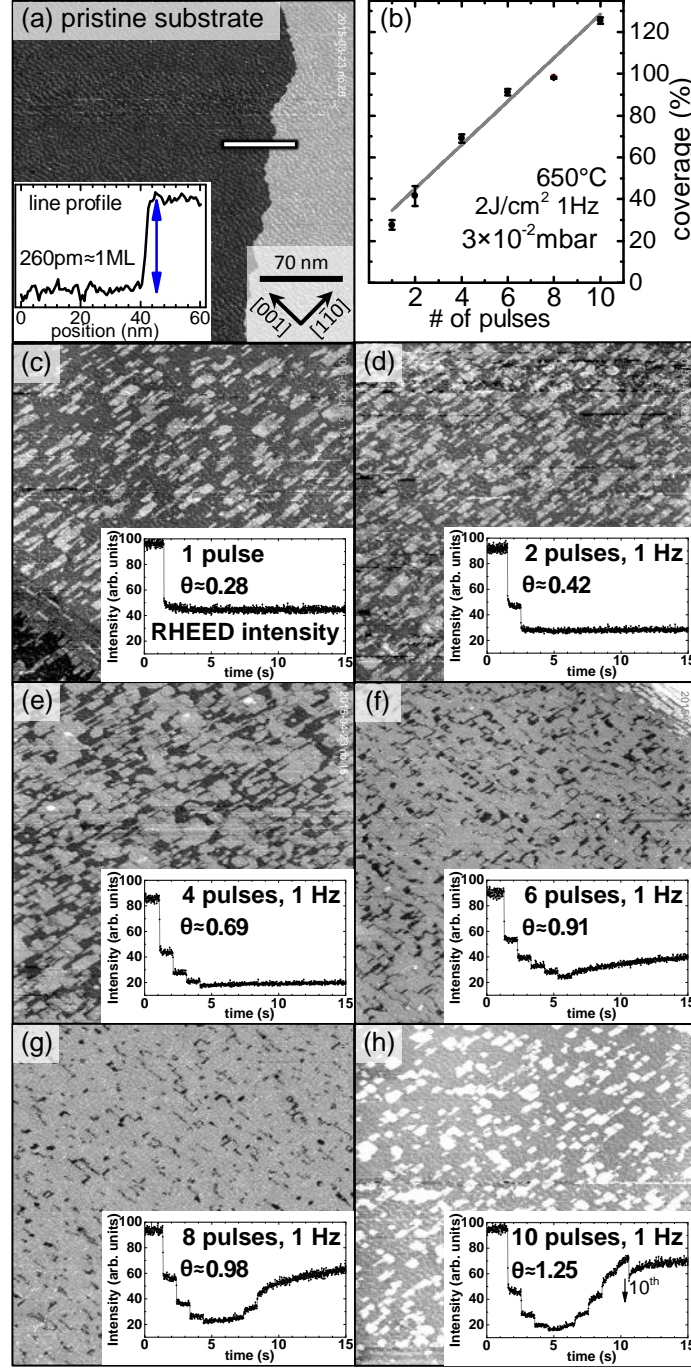


FIGURE 3.30.: (a) Large-area STM image of the pristine surface prior to deposition. The inset in (a) shows the profile across the white line. (c)-(h) Series of STM images and corresponding RHEED intensity variations during the homoepitaxial growth of one monolayer on the SrTiO₃(110)-(4 \times 1) surface. A freshly-prepared substrate was used each time. (b) Area coverage derived from an analysis of STM images and a linear fit to the data.

3.5.2. RHEED oscillations corresponding to layer-by-layer growth

Figure 3.30 shows STM images and the corresponding RHEED intensity variations during the growth of the first monolayer (ML). Panel (a) shows the pristine surface; a similar surface was prepared prior to each deposition. The surface consists of terraces of several hundred nm in width, and the line profile indicates unit-cell step heights. Figures 3.30(c)-(h) show the surface in STM after deposition of sub-ML amounts of STO at 650 °C substrate temperature with 1 Hz repetition rate. Variations of the RHEED specular spot intensity, recorded during deposition, are shown in the insets of Figures 3.30(c)-(h). The number of pulses stated in the insets was applied consecutively, and the substrate was kept at the deposition temperature for an additional 10 min before cool-down and transfer to the surface analysis chamber and STM measurements.

After deposition of one pulse [see panel (c)], single-layer high islands appear on the surface. The considerable drop in the RHEED intensity is consistent with an increased step density at the surface. Note that we aligned the RHEED beam parallel to the $[1\bar{1}0]$ direction, therefore only steps parallel to the $[001]$ direction are strongly influencing the RHEED intensity. The islands tend to grow elongated in $[1\bar{1}0]$ direction indicating either anisotropic sticking to the island edges or anisotropic diffusion of adspecies with the fast diffusion direction along $[1\bar{1}0]$, *i.e.*, parallel to the bright (4×1) rows [*cf.* lower panel of Figure 3.4(a)]. Similarly elongated islands have been reported by Feng *et al.* during homoepitaxial MBE growth on the STO(110)- (4×1) surface [107].

As the number of laser pulses increases, the number and size of the islands on the surface increase and the RHEED intensity decreases accordingly [panels (d) and (e)]. Upon increasing the number of pulses from 4 to 8 [panels (f) and (g)], the percolation network is progressively filled, leaving only a few open areas on the surface, and the RHEED intensity increases with each pulse. Note that no second-layer islands have formed yet, *i.e.*, the growth follows an ideal layer-by-layer mechanism. The RHEED intensity profile in Figure 3.30(h) shows that the 10th pulse reduces the RHEED intensity again. This is in line with the STM images

3. Results

showing a completely filled first layer and nucleation of 2nd layer islands. Thus the amount necessary for the growth of one ML under these conditions lies between 8 and 9 pulses, and one oscillation of the RHEED intensity indeed corresponds to the growth of one ML.

Analysis of STM images shows that the island-coverage linearly increases with the number of UV laser pulses, see Figure 3.30(b). However, it should be mentioned that the linear fit in panel (b) does not intercept the vertical axis at zero, indicating an apparent initial coverage of around 25% prior to deposition. This issue is related to the shutter of PLD system not entirely shadowing the particle flux created during pre-ablation in 3×10^{-2} mbar oxygen pressure. Indeed, STM images acquired after pre-ablation with the shutter in front of the substrate (not shown) reveal that the terraces are covered by single-layer thick islands with a coverage of approximately 0.25 ML. Because the relatively large shutter (9×7 cm²) completely obstructs the sample from the target, ablated particles can only bypass the shutter by scattering multiple times in the background atmosphere. Because lighter plasma constituents scatter more strongly [108], this leads to a Ti enrichment of the impinging flux and the first islands nucleating on the surface will exhibit a slightly different stoichiometry. This was also observed in STM - some of the islands exhibit the (2×4) structure [whose stoichiometry is Ti-rich with respect to the ($n \times 1$) structures], surrounded by (4×1)-reconstructed terraces (see below in Section 3.6 for implications of the coexistence of multiple surface structures on the diffusion and growth). This indicates that the flux originated from the pre-ablation process was indeed Ti-enriched. In order to minimize the actual deposition amount during pre-ablation, we designed a new, bigger shutter for the system that has been mounted recently.

3.5.3. Verification and extension of the step density model

Figure 3.30 follows the completion of one ML by means of STM and RHEED. The STM images indicate the coalescence of the islands starting between the 2nd and the 4th pulse, where the RHEED intensity reaches its minimum. We analyzed high-resolution STM images to derive the density of steps parallel to the [001] direction

3. Results

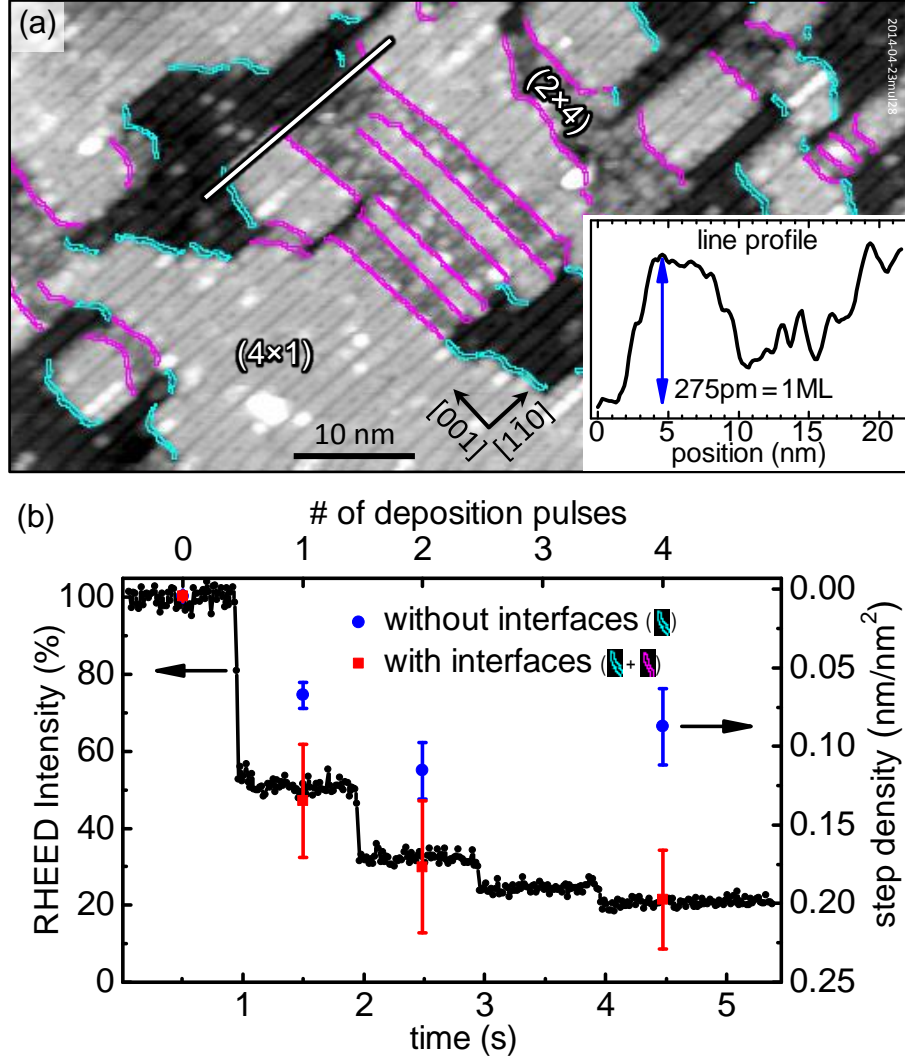


FIGURE 3.31.: (a) STM image showing islands after the growth of 4 pulses at 650 °C substrate temperature in 3×10^{-2} mbar oxygen. The border of the islands and the interfaces between $(n \times 1)$ and (2×4) regions, all parallel to the $[001]$ direction, are highlighted in cyan and magenta, respectively. The inset shows the profile along the line in (a). (b) RHEED intensity overlaid with the step density (analyzed from STM images) with (red squares) and without (blue circles) considering the interfaces between the different reconstructions, respectively. Note that the step density axis is inverted.

3. Results

on the surface. Interestingly, this analysis revealed a *lower* step density after the 4th pulse compared to the 2nd pulse [*cf.* blue circles in Figure 3.31(b); note that the step density axis is inverted]. According to the step density model [62], this would cause an *increased* RHEED specular spot intensity after the 4th pulse, compared to after the 2nd pulse. However, the RHEED specular spot intensity decreases after the 4th pulse. This comparison shows that the steps introduced by the border of the islands alone do not represent a reliable measure of the step density on the surface.

High-resolution STM images of the islands nucleated on the surface show that the islands often consist of two inherently different reconstructions. While the larger portion of the island exhibits the same reconstruction as the substrate layer, *i.e.*, a mix of (4×1) and (5×1) reconstructions, parts of the islands exhibit the (2×4) structure, see Figure 3.31(a). (We identified the (2×4) structure through its appearance in STM and LEED, *cf.* Fig. 3.2.) The line profile in Figure 3.31(a) shows that the (2×4) reconstruction has an apparent height of around half a ML. Because (2×4) regions appear as depressions with respect to $(n\times 1)$ areas in a wide range of tunneling conditions (1.4 V–6.9 V; 0.05 nA–1.9 nA), we conclude that the depressed appearance originates from a topographic height difference, rather than from purely electronic effects. Therefore the linear boundaries between $(n\times 1)$ and (2×4) domains [highlighted by magenta lines in Figure 3.31(a)] have to be counted as steps when analyzing the step density from STM images. Indeed the step density and the RHEED intensity fit very well after considering also the step density introduced by these interfaces [see Fig. 3.31(b), red squares]. Note that the axis of the step density in Fig. 3.31(b) has been adjusted to overlay the minimum (0.0046 ± 0.009 nm/nm²) and the maximum (0.1977 ± 0.0314 nm/nm²) step densities (with interfaces considered) with the maximum and the minimum RHEED intensities, respectively. This is a reasonable representation because the maximum RHEED intensity is expected at the minimum step density, and *vice versa*. With this overlay, the scaling of the normalized RHEED intensity $I(t)$ follows quantitatively the well-known relation to the step density as $I(t) = 1 - S(t)/S_{\max}$, where $S(t)$ is the step density at a given time (or laser pulse) and S_{\max}

3. Results

is the maximum step density, at which the RHEED intensity is a minimum [62].

3.5.4. Substrate temperature versus island density and shape

Figures 3.32(a)-(c) show STM images acquired after deposition of one laser pulse at different substrate temperatures. Prior to each deposition, the substrate was again prepared to exhibit a predominantly (4×1) -reconstructed surface. The insets show the RHEED intensity after growth – the sample was still kept at the deposition temperature for 10 min total before cool-down and STM measurements. The STM images show a considerable reduction of the island density when the temperature during growth and annealing is increased first from 650 °C to 750 °C and then to 850 °C. The increase of the substrate temperature has also a prominent influence on the relaxation of the RHEED intensity, which recovers considerably faster at higher temperatures. After deposition at 650 °C, the RHEED intensity stays almost constant, meaning that island nucleation takes place much faster than the integration time of the camera (~ 16 ms), and that the 10 min post-annealing only causes a negligible change in the surface morphology. The magnitude of the initial drop of the RHEED intensity is comparable for all sample temperatures indicating a similar step density right after deposition. The long-term relaxations visible at higher temperatures therefore indicate a coarsening of the islands, which, at 850 °C, predominantly ends with the attachment of these islands into the terrace steps.

Comparing the deposition after one pulse at 650 °C and 850 °C [see Figures 3.32(a) and (c)], the size, the amount, and the aspect ratio of the islands have changed considerably. Fig. 3.32 also provides a quantitative evaluation of the island dimensions [panel (d), wider circles indicate higher counts] and the island densities [panel (e)]. Figures 3.32(d) shows that at 650 °C growth temperature, islands preferentially grow elongated along $[1\bar{1}0]$ direction with typical dimensions of around 3.5×10 nm². At 750 °C, two maxima appear in this plot, *i.e.*, part of the island population exhibits the same aspect ratio (7×23 nm², $AR \approx 3.0$, solid line) as islands nucleated at 650 °C, while another part of the population has grown elon-

3. Results

gated along $[1\bar{1}0]$ ($7 \times 38 \text{ nm}^2$, $\text{AR} \approx 4.6$, dashed line). This indicates that 750°C can be considered a critical temperature, at which ripening during the 10 min post-anneal partly leads to the coalescence of the islands. At 850°C , the aspect ratio of the islands almost approaches unity ($\text{AR} \approx 1.5$, dot-dashed line). The AR values of 3–4.6 at $650\text{--}750^\circ\text{C}$ indicate preferential diffusion (or preferential sticking) of adspecies along $[1\bar{1}0]$ direction, while at 850°C the diffusion (or sticking) in both directions on the surface is comparable giving rise to $\text{AR} \approx 1.5$.

The number of islands per unit surface area, derived from a quantitative analysis of STM images, shows an exponential increase with the inverse of the growth temperature, as shown in the Arrhenius plot in Figures 3.32(e). If the critical nucleus size and the amount of material attached to the steps at higher temperatures were known [109, 110], it would be possible to derive diffusion barriers from this plot.

3.5.5. Using the UV laser repetition rate to tune the growth mode

Figure 3.33 exemplifies the dependence of the growth mode on the UV laser repetition rate in the homoepitaxial deposition of STO at 850°C . At 1 Hz repetition rate, layer-by-layer growth is obtained, see panel (a). STM images show the gradual formation of one ML and the corresponding RHEED intensity variation shows nearly one full oscillation after 8 pulses at 1 Hz. A drastic decrease of the growth speed to one pulse every 10 min leads to a predominantly step-flow growth regime, see Figure 3.33(b). RHEED intensity profiles show nearly full relaxation after each laser pulse and STM images reveal an essentially unchanged island density of $(1.3 \pm 0.3 \times 10^{-4} \text{ islands/nm}^2)$ for different number of pulses.

3.5.6. Summary: Early stages of $\text{STO}(110)\text{--}(4 \times 1)$ homoepitaxial growth

We have followed the early stages of homoepitaxial PLD growth of the $\text{SrTiO}_3(110)\text{--}(4 \times 1)$ surface by means of STM and RHEED, and we have shown that well-defined (4×1) surfaces can be prepared by PLD with the exception of (2×4) patches at-

3. Results

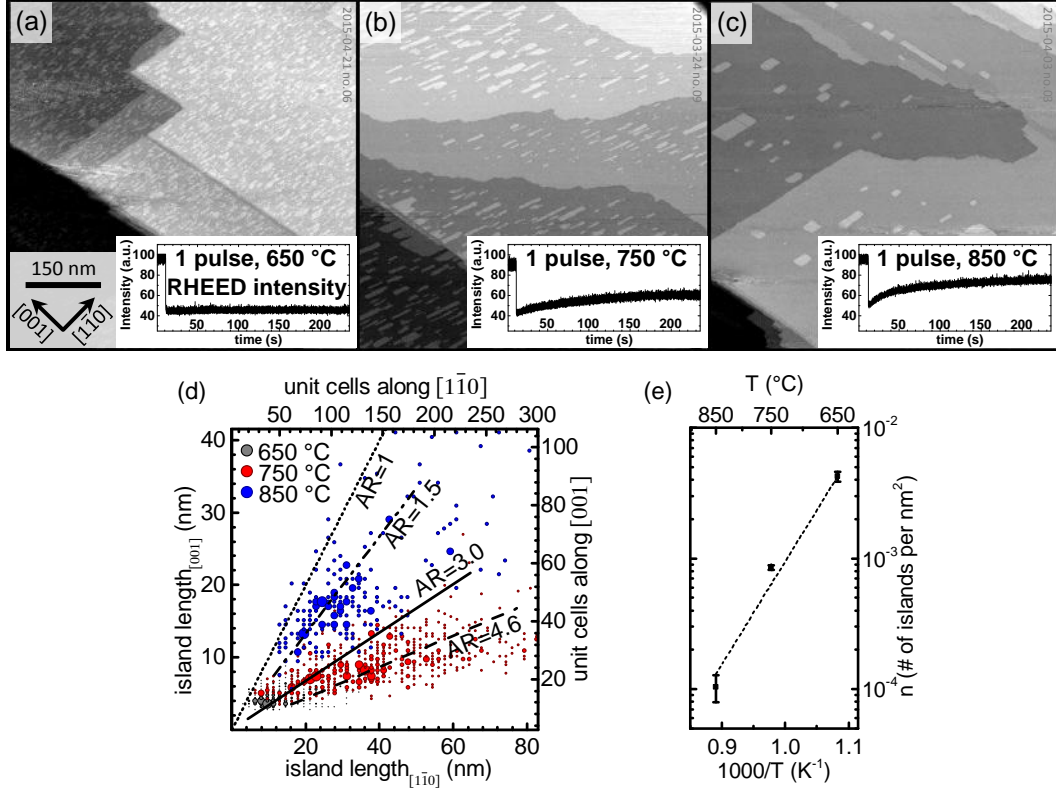


FIGURE 3.32.: STM images and corresponding RHEED intensity relaxations of one pulse deposited at substrate temperatures of (a) 650 °C, (b) 750 °C, and (c) 850 °C. (d) Distribution of island dimensions after 1 pulse (+ post annealing) at different growth temperatures. Larger circles indicate higher number of counts. The lines indicate different aspect ratios (AR). Note that only rectangular-shaped islands are counted; coalesced islands with different shapes were neglected. (e) Island density derived from the analysis of STM images in an Arrhenius plot.

3. Results

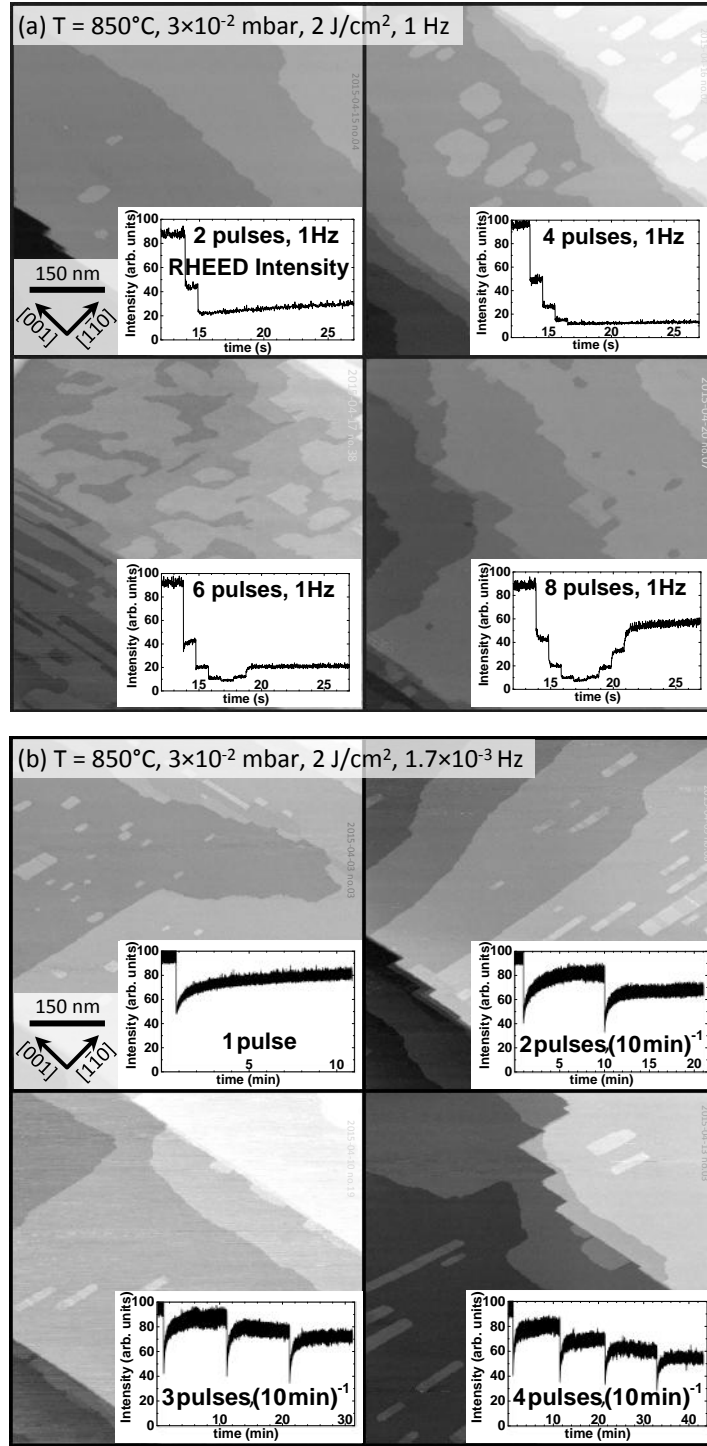


FIGURE 3.33.: Comparison of STM images (main panels) and RHEED intensity variations (insets) of sub-monolayer amounts deposited with (a) fast (1 Hz) and (b) slow (1 pulse per 10 min) repetition rate.

3. Results

tributed to non-stoichiometry. Islands nucleated on the STO(110) surface exhibit the same reconstruction as the substrate surface indicating that the deposited material grows as sub-surface bulk-like layers with the reconstruction floating to the top surface. We confirmed the correspondence of RHEED intensity oscillations with ideal layer-by-layer growth, and point to a problem occurring in probably all PLD systems. That is, during pre-ablation of the target, particles are able to reach the substrate surface even with the shutter in closed position. This can cause uncontrolled growth of the first layer, which might substantially change the properties of the interface. Although this might not be an issue if pre-ablation is done in ultra-high vacuum conditions, we assumed that pre-ablation should be carried out with the actual deposition pressure applied to the system.

We tested the step-density model for the RHEED intensity by interrupting the growth after deposition of sub-ML amounts and subsequent STM analysis. The step-density model explains variations in the RHEED intensity by oscillations of the density of steps introduced by islands on the surface during growth. We analyzed the actual step density from high-resolution STM images and compared it with the drop in RHEED intensity for the first few laser pulses. We conclude that not only the steps introduced by the islands' circumference add to the step density. Also the interfaces formed between two inherently different surface reconstructions have to be counted as steps as well. It should be noted that this is still a simplified model, which entirely neglects possible differences in electron reflectivity of the two different reconstructions on the islands. Furthermore, the topographic difference between (2×4) and (4×1) areas is expected to cause out-of-phase diffraction that will in addition cause a decrease in the RHEED intensity. However, given the successful match between the RHEED intensity and the step density including the interfaces, we believe that the steps are the dominant factor behind the RHEED oscillations also on this surface with two different reconstructions.

Variations of the PLD parameters, in particular growth temperature and deposition rate were used to tune the island density and the morphology of the surface. The strong dependence of the island density and morphology on the substrate temperature highlights the need for a uniform temperature across the surface. The IR

3. Results

laser directly shone onto the back of the sample ensures a uniform heating with differences in the temperature across the sample of less than 5 °C. The control of the film structure and morphology should facilitate research on the interaction of chemical species with this surface, and allows studies of the relation of step edges in promoting chemical reactions. The growth mode can be tuned by variation of the temperature, or by large changes in the UV laser repetition rate, corresponding to a different time-averaged flux. This dependence can be used when growing materials sensitive to high temperature or when strong intermixing is expected at elevated temperatures.

3.6. Homoepitaxial growth of STO(110) surfaces with PLD: Growth of multi-layer films

In addition to the results presented in the previous section about the early stages of growth on the $\text{SrTiO}_3(110)-(4\times 1)$ surface, we have investigated the homoepitaxial growth of thick films on different STO(110) surfaces by means of RHEED, LEED, XPS, and STM in our setup (see experimental Section 2.9), as well as *ex-situ* X-ray diffraction (XRD). The research has been conducted mainly by Stefan Gerhold and Michele Riva, with considerable input from Bilge Yildiz, Michael Schmid, and Ulrike Diebold. XRD has been performed at the X-ray center of the TU Wien by Klaudia Hradil and Werner Artner. The results should be considered tentative – a manuscript is in preparation.

All films have been deposited following the protocol described in the experimental Section 2.10, with a deposition rate of 1 Hz, and with a 10 min post-anneal right after deposition, until the RHEED intensity was fully relaxed.

3.6.1. Overview and Background

Off-stoichiometry in PLD of STO

Growing thick epitaxial films for surface-science experiments is a challenge for several reasons. Besides the requirements of the analysis techniques, *e.g.*, STM

3. Results

requires the films to grow atomically flat and well-defined, and to be free of adsorbates, the stoichiometric material transfer from the target to the substrate is an often reported problem for PLD grown films [63]. Several processes can lead to non-stoichiometric deposition, schematically shown in Figure 3.34(a) (reprinted from ref. [63]). The first process in a pulsed laser deposition experiment is the laser ablation of the target material. It has been reported for PLD of SrTiO_3 that preferential ablation leads to a Sr-rich plasma plume at low laser fluences [111]. Following the ablation, the plasma plume propagates through the background atmosphere towards the substrate. It was shown that preferential scattering of the light plasma constituents (Ti ions) leads to a Ti-depletion of the central part of the plasma plume [108]. This implies that both, a low UV laser fluence and a high deposition pressure increase the Sr/Ti ratio of the deposited flux. Furthermore, there is the possibility of preferential sputtering of the thin film due to high-energy ablated particles.

Off-stoichiometry and STO(110) surfaces

The STO(110) surface is very sensitive to changes in the stoichiometry. This is evident from the surface phase diagram, presented in Section 3.1. It describes the dependence of the STO(110) surface structure on the near-surface stoichiometry. Wang and coworkers have calibrated this phase diagram *in-situ* by following the evolution of the surface structures by RHEED while depositing Sr or Ti metal with a well-defined flux. According to their work, a change from (4×1) to (5×1) , and to (6×1) reconstruction can be induced by deposition of $0.15 + 0.40 = 0.55$ ML of Sr (1 ML corresponds to the density of STO(110) unit cells, *i.e.*, 4.64×10^{14} atoms/cm²) at elevated temperature and pressure (800 °C, 5×10^{-6} mbar O₂). The same amount (in ML) of Ti is necessary to induce a change back, *i.e.*, the process is fully reversible. Similarly, a change from the (4×1) to the (2×4) reconstruction is induced by deposition of 0.75 ML of Ti. Therefore, an apparent change of the surface structure after growth can be interpreted as a net enrichment of the near-surface region by either Sr or Ti metal.

3. Results

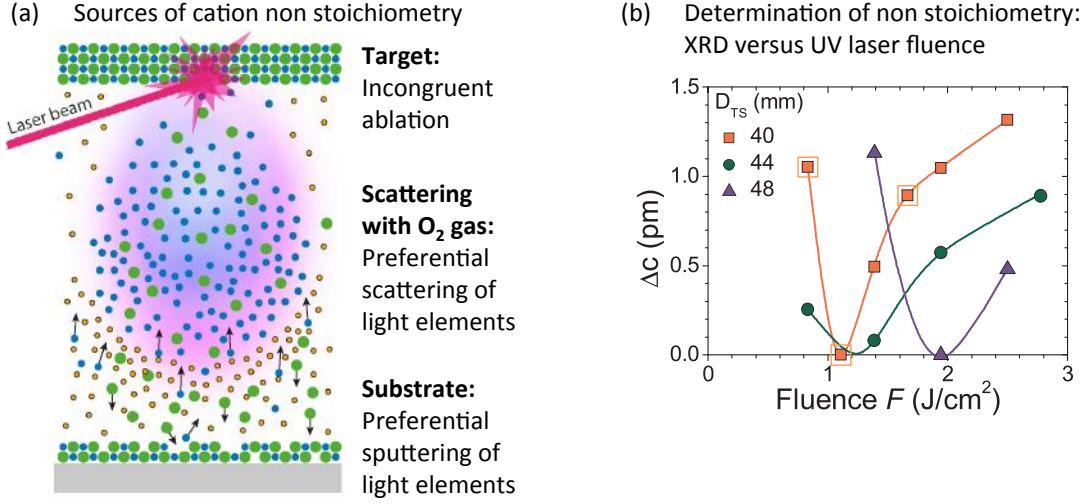


FIGURE 3.34.: (a) Schematic of PLD showing several processes during the different stages of PLD that may lead to non-stoichiometric deposition. Heavy and light cations are drawn as large green and small blue circles, respectively. Oxygen is not shown. Background gas atoms drawn as small orange circles. Image reprinted with permission from ref. [63]. (b) c-axis expansion (Δc) of homoepitaxial STO(001) thin films (≈ 200 nm) versus UV laser fluence (f) at different target-to-substrate distances (D_{TS}) grown at a substrate temperature $T_S = 720^\circ\text{C}$ in 0.2 mbar O₂ background pressure. Reprinted from ref. [108] with the permission of AIP Publishing.

3. Results

Detection of off-stoichiometric growth of STO(001): X-ray diffraction (XRD)

On the STO(001) surface, slightly off-stoichiometric deposition is typically associated with the creation of cation vacancies, and results in a tetragonal distortion of the film. This means that the film grows epitaxial in-plane with an expanded out-of-plane lattice parameter c [112]. A change of the latter can be detected by X-ray diffraction and it was shown that a deviation from the optimal $\text{Sr}/\text{Ti} = 1$ composition yields a $\Delta c > 0$. Figure 3.34(b) shows the XRD-derived expansion of the out-of-plane lattice parameter (Δc) dependent on the UV laser fluence (f) and target-to-substrate distance (D_{TS}). The figure shows that for a given target-to-substrate distance there is an optimal UV laser fluence at which the film grows essentially unstrained. A lower, or a higher fluence causes the film to expand. In addition, Figure 3.34(b) indicates that the optimal UV laser fluence depends on the target-to-substrate distance. Note that an increase in the value D_{TS} is similar to an increased background-gas pressure, as both parameters directly influence the probability of scattering of the plasma plume with the background gas. Out-of-plane lattice expansion has been observed for homoepitaxial films on STO(001) grown by both, molecular beam epitaxy (MBE) [113], and PLD [112]. It should be mentioned that for a similar deviation from the optimal stoichiometry, MBE-grown films exhibit a smaller lattice expansion, as compared to PLD-grown films [113]. This suggests that the PLD process is able to cause stoichiometric defects in the films. Strongly Sr-rich deposition may also result in the formation of interstitial SrO planes of Ruddlesden-Popper (RP) type, as has been reported by Tokuda *et al.* [114]. Because these RP-type planes are oriented parallel to (001) planes, such planes are not expected to form during the growth of the STO(110) surface. In addition, it should be mentioned that oxygen-deficient films do not show considerable strain in XRD, excluding the possibility that V_{O} s are the main cause for the c -lattice expansion [112].

3. Results

Outline of this chapter

As mentioned above, the stoichiometry of PLD-grown thin films mainly depends on two parameters, *i.e.*, the UV-laser fluence and the pressure during deposition [63]. We therefore tested the influence of these parameters on the stoichiometry and on the growth characteristics of thin homoepitaxial films on STO(110). We present results of *in-vacuo* XPS-measurements, and show that these measurements do not provide an accurate measure of the films' stoichiometry. We show that non-stoichiometric growth results in a change of the film surface structure. Following this, we report on the influence of different surface structures on the diffusion and island growth, and its implications for thick-film growth. We point out that the surface structure of the pristine substrate can have a strong influence on the morphology of the resulting film. Finally, we present our approach of determining the cation composition of thin films by using the stoichiometry-dependent evolution of surface structures on STO(110).

3.6.2. Stoichiometry measured by XPS

Since our PLD setup is connected to a surface analysis system equipped with XPS, we have routinely characterized STO(110) surfaces with this technique. We have measured 18 pristine samples, each exhibiting a well-defined surface structure with predominantly the (4×1) reconstruction, and computed the apparent Sr/Ti ratios from XPS spectra (see experimental Section 2.1 for details). We found that these ratios exhibit a standard deviation of 3.8 %. The present XPS results are therefore not an accurate measure of the film stoichiometry, but we were able to observe trends in the results. A possible reason for this spread might be the non-uniform surface structure across the substrate surface, as determined by LEED. When moving the focus of LEED across the sample, we typically observed a gradient from (2×4) to the (5×1) reconstruction. Because the electron analyzer exhibits a rather large acceptance area (ideally this would be ~ 0.7 mm in diameter, in reality probably larger), as compared to the size of STM images (~ 500 nm), this could result in differences in the apparent Sr/Ti ratio of the surface.

3. Results

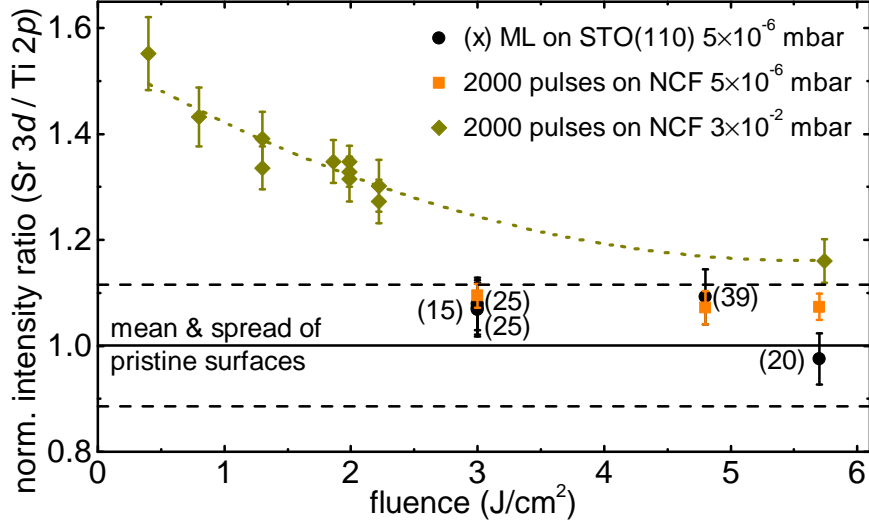


FIGURE 3.35.: Summary of normalized Sr 3d over Ti 2p XPS core-level intensity ratios. XPS intensities from films deposited onto NiCroFerTM (NCF) sample plates have been normalized to the mean value of the Sr/Ti ratios determined from several measurements of pristine surfaces. Homoepitaxial films on STO(110) substrates were normalized to the Sr/Ti ratio of their corresponding pristine surfaces before deposition. The labels stated in parentheses refer to the corresponding film thickness in monolayers. Pressures stated are total pressures of pure O₂. The dashed, black lines indicates three times the standard deviation of the Sr/Ti ratios for the pristine surfaces. The dotted, green line is a guide to the eye. See experimental Section 2.1 for details about Sr/Ti ratio determination.

Figure 3.35 shows the Sr 3d over Ti 2p XPS intensity ratios for several films deposited with different UV laser fluences and deposition pressures. We normalized the Sr/Ti ratios in order to compare the XPS results of thin films deposited onto sample plates with the results from homoepitaxially grown films. The ratios for films deposited onto NiCroFerTM (NCF) sample plates were normalized to the mean value for the different pristine STO(110) surfaces. For each homoepitaxial deposition, the final ratio of the film was normalized by the corresponding ratio of the pristine substrate prior to growth. The dashed line represent three times the standard deviation of the normalized Sr/Ti ratio for the pristine surfaces.

We deposited 2000 pulses onto polished and UHV-annealed (1000 °C) NCF sample plates at different UV laser fluences and pressures (see green diamonds and orange squares in Fig. 3.35). RHEED indicated that all films on NCF sample

3. Results

plates were polycrystalline. (Using a typical deposition rate of 23.5 pulses per monolayer (ML), as determined from RHEED oscillations of STO homoepitaxy at 5.7 J/cm^2 in 7×10^{-2} mbar O_2 , 2000 pulses correspond to a thickness of approximately 23.5 nm. Note that the deposited amount scales with the UV laser fluence – lower fluences therefore indicate less thick films.) Similar to what has been reported previously [112], the Sr/Ti ratio increases for films grown with lower UV laser fluences. At a pressure of 3×10^{-2} mbar only films deposited with fluences of as high as 5.7 J/cm^2 resemble the Sr/Ti ratio of the pristine STO(110) surfaces (the dotted green line provides a guide to the eye).

These results indicate that in the present setup, it is not possible to obtain stoichiometric growth in a background pressure on the order of 10^{-2} mbar. All films grown in this pressure range exhibited a normalized Sr/Ti ratio that lies outside of the spread of the values of the pristine surfaces. Only after reducing the pressure considerably to 5×10^{-6} mbar, the films exhibited a Sr/Ti ratio, which is similar to that of the pristine surfaces (see orange squares). In this pressure range, also films deposited with a laser fluence of about 3 J/cm^2 show a normalized Sr/Ti ratio close to that of the pristine surfaces. The black dots in Figure 3.35 show the normalized Sr/Ti ratio of homoepitaxially grown STO(110) films of various thicknesses (see labels next to black dots for the corresponding thickness in MLs). It can be seen that for a wide range of laser fluences the films show an XPS-derived cation ratio that lies within the spread of the pristine surfaces (dashed lines).

3.6.3. Slightly Sr-rich growth

In the following two sections, we discuss the homoepitaxial growth with a low and a high laser fluence resulting in an expected Sr- and Ti-rich deposition. As presented in Section 3.1, the STO(110) surface structure depends on the near-surface stoichiometry and off-stoichiometric growth is therefore expected to influence the surface of the thin films.

Figure 3.36 compares reciprocal-space (LEED, RHEED) and direct-space (STM) surface analysis before and after deposition of 25 ML onto a mixed (4×1) and (5×1) reconstructed surface (deposition parameters: $f = 3 \text{ J/cm}^2$, $T_s = 750^\circ\text{C}$,

3. Results

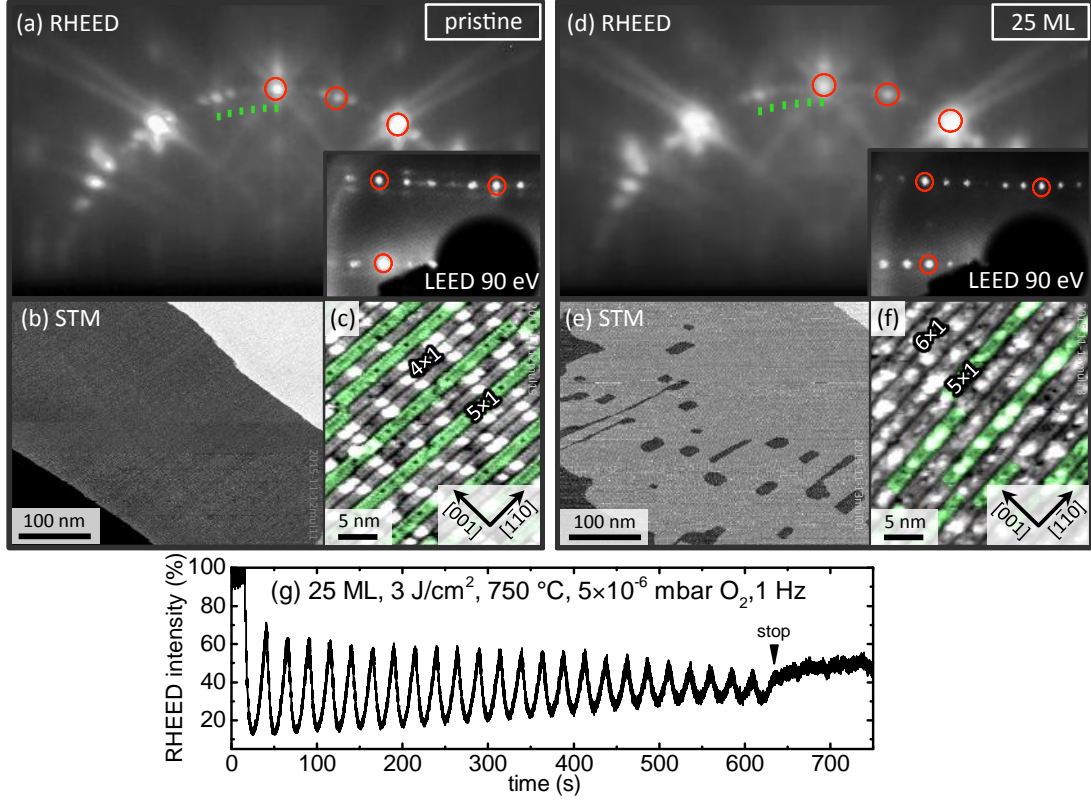


FIGURE 3.36.: Characterization of STO(110) surfaces before and after homoepitaxial growth of 25 ML. (a,d) RHEED patterns acquired with 35 keV electrons parallel to the $[\bar{1}\bar{1}0]$ direction. (b,c) STM images of the pristine $(4\times 1) + (5\times 1)$ surface, and (e,f) of the 25 ML film surface exhibiting a mixed $(5\times 1) + (6\times 1)$ reconstructed surface. Lines of (5×1) reconstruction are highlighted in green in panels (c) and (f). (g) RHEED specular-spot intensity oscillations during deposition.

3. Results

$p = 5 \times 10^{-6}$ mbar O_2 , 1 Hz). Figure 3.36(a) shows the RHEED and LEED (inset) patterns of the pristine surface; bulk-derived spots are marked by red circles. In RHEED, a five-fold periodicity is visible [green dashes in panel (a)], while LEED shows a pattern of a mixed $(4 \times 1) + (5 \times 1)$ surface (compare with Figure 3.6 in Section 3.4 above for an interpretation of this LEED pattern). Figure 3.36(c) shows a high-resolution STM image of the surface, confirming the mix of (4×1) and (5×1) reconstruction ((5×1) lines are highlighted in green). Analysis of several high-resolution STM images of the pristine surface revealed that $\sim 31\%$ of the surface was covered by the (5×1) reconstruction (highlighted in green) on an otherwise (4×1) -reconstructed surface. We determined the coverage of (5×1) -reconstructed areas by counting the number of (5×1) lines in STM images, and compared this number to the total number of (4×1) and (5×1) lines (taking into account the different widths of the two reconstructions).

This surface was used as a substrate for the homoepitaxial growth of 25 ML ($= 6.9$ nm), as determined from oscillations of the RHEED specular spot intensity, see Figure 3.36(g). The RHEED intensity drops to about 70 % of its initial value after the first oscillation. We believe this is due to the difference in temperature during annealing and during growth. Annealing was carried out at 1000°C , which results in large terraces and a nice ordering of the surface structure on the atomic scale, see Section 3.4. The substrate temperature during deposition was set to only 750°C , which is expected to result in a morphologically more rough surface. Therefore, this drop in the RHEED intensity is most likely related to the change in average terrace size, *i.e.*, to a different step density on the surface. Note that the image of the 25 ML film surface presented in Figure 3.36(e) was acquired after keeping the substrate at deposition temperature for additional 10 min after growth. The resulting film surface appears very similar to the pristine substrate surface. RHEED reveals a smeared out five-fold periodicity [green dashes in panel (d)], while LEED clearly shows a six-fold symmetry [see inset of panel (d)]. Also note the intense Kikuchi lines running through the bulk derived spots in the RHEED pattern, which indicate a flat surface with a high order of crystallinity [115]. STM shows a surface consisting of a mix of $(5 \times 1) + (6 \times 1)$ re-

3. Results

constructions [panel (f)] on terraces of several hundred nm in width [panel (e)]. Analysis of several high-resolution STM images revealed a surface after growth with 21 % (5×1) and 79 % (6×1) reconstruction. Obviously, the surface structure has changed during growth from mainly (4×1) to mainly (6×1) reconstruction. However, Figure 3.36 shows that morphologically and structurally well-defined homoepitaxial films on STO(110) can be produced by PLD – even for a Sr-rich PLD flux.

Defects in the surface structure of thick films

We deposited two films with a thickness of 39 ML and 42 ML. Each of the films exhibited a flat surface with several hundred nm wide terraces. In addition, these films showed defects in the atomic-scale surface structure. Figure 3.37 shows the surface of the 39 ML film deposited onto a mixed (4×1) and (5×1)-reconstructed substrate. (Growth parameters: $f = 4.8 \text{ J/cm}^2$, $T = 750^\circ\text{C}$, $p = 5 \times 10^{-6} \text{ mbar O}_2$). The resulting film surface is almost entirely covered with the (5×1) reconstruction. Panel (a) shows a terrace of the film with the two types of defects highlighted in green and blue, respectively. One type appears similar to a dislocation – one reconstruction line begins somewhere on the surface with bright dots at its origin (highlighted by the green oval). This defect is not necessarily related to a dislocation-like defect in the subsurface region, because the interstitial (5×1) line occupies the space of five STO unit cells along $[001]$ direction. Panel (b) shows a magnified view of such a dislocation-like defect. Another type of defect appears as big bright protrusions (blue oval), probably indicating subsurface interstitial atoms.

3.6.4. Slightly Ti-rich growth

In this section we discuss how a Ti-rich deposition causes the film to grow in a morphologically undesirable way. The substrate was again prepared to exhibit predominantly the (4×1) reconstruction with a small admixture of (5×1) reconstruction. Figure 3.38 shows the surface after homoepitaxial deposition of 385 pulses of STO with a high laser fluence of 5.7 J/cm^2 ($p = 4 \times 10^{-6} \text{ mbar O}_2$, $T = 750^\circ\text{C}$).

3. Results

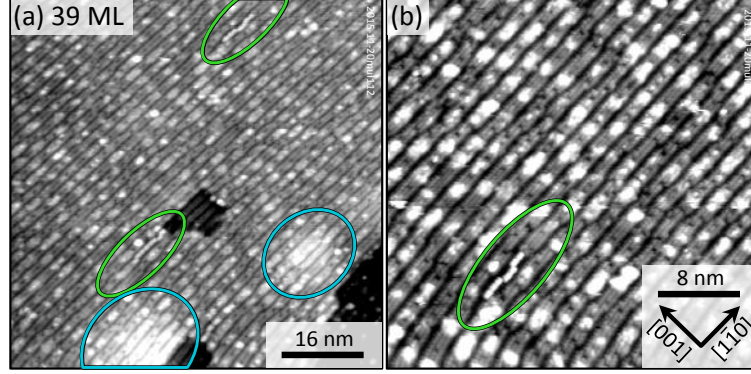


FIGURE 3.37.: STM images of 39 ML thick film showing two types of defects. Dislocation-like and subsurface-defects are highlighted by green and blue ovals, respectively. Growth parameters: $f = 4.8 \text{ J/cm}^2$, $T = 750^\circ\text{C}$, $p = 5 \times 10^{-6} \text{ mbar O}_2$.

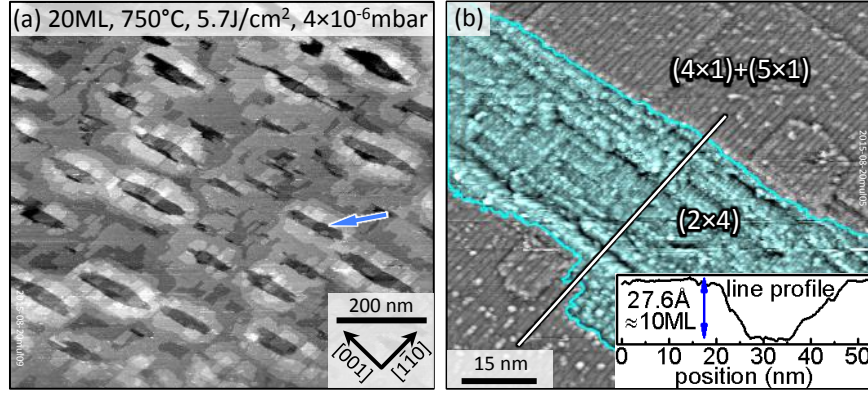


FIGURE 3.38.: STM images of a ~ 20 ML thick homoepitaxial film on STO(110) deposited with a high laser fluence. The blue arrow in (a) indicates a pit formed on the surface. (b) High-pass filtered and zoomed image of the pit marked in panel (a) revealing (2×4) reconstructed regions inside the pit. The inset shows the profile of the line across the pit in (b).

3. Results

Unfortunately, the RHEED signal was blocked by the sample mounting for this particular deposition. However, from depositions in similar conditions we can estimate this number of laser pulses to correspond to a 19–20 ML thick film. The morphology of the surface has changed considerably after deposition – deep pits have formed on the surface, see blue arrow in Figure 3.38(a). A magnified, high-pass filtered image of the pit marked by the arrow in panel (a) is shown in panel (b). Interestingly, most of the surface inside the pit exhibits the (2×4) reconstruction. From the phase diagram it can be expected that a Ti-rich flux will cause part of the surface structure to change from the (4×1) to the (2×4) structure. In order to gain insight into how the (2×4) structure can cause such a change in the surface morphology, we performed several control experiments, which will be discussed in the following.

3.6.5. Test-experiments

Stability of $(n\times 1)$ - and (2×4) -reconstructed surfaces in growth conditions

In a typical PLD deposition, the substrate is heated to the deposition temperature and remains at this temperature until the RHEED geometry is optimized and the growth is initiated. We know how the surface responds to annealing at 1000 °C, which results in flat terraces with well-defined ordering of the surface structure on the atomic scale, see Section 3.1.1. We do not know, however, how the surface reacts to the typical deposition temperature of 650 °C in 10^{-2} mbar O_2 . In the following, we will discuss how different pristine surface structures response to the typical growth conditions.

As shown in Section 3.1, the STO(110) surface exhibits a variety of structures, which are related to the near-surface stoichiometry, and only a precise preparation leads to a fully (4×1) -reconstructed surface. However, preparation by sputtering and annealing often results in a surface that consists of a mix of two reconstructions, *i.e.*, $(4\times 1) + (5\times 1)$, or $(4\times 1) + (2\times 4)$, as shown in the STM images in Figures 3.39(a) and (c), respectively.

The coexistence of (4×1) and (5×1) reconstructions results in a surface with a

3. Results

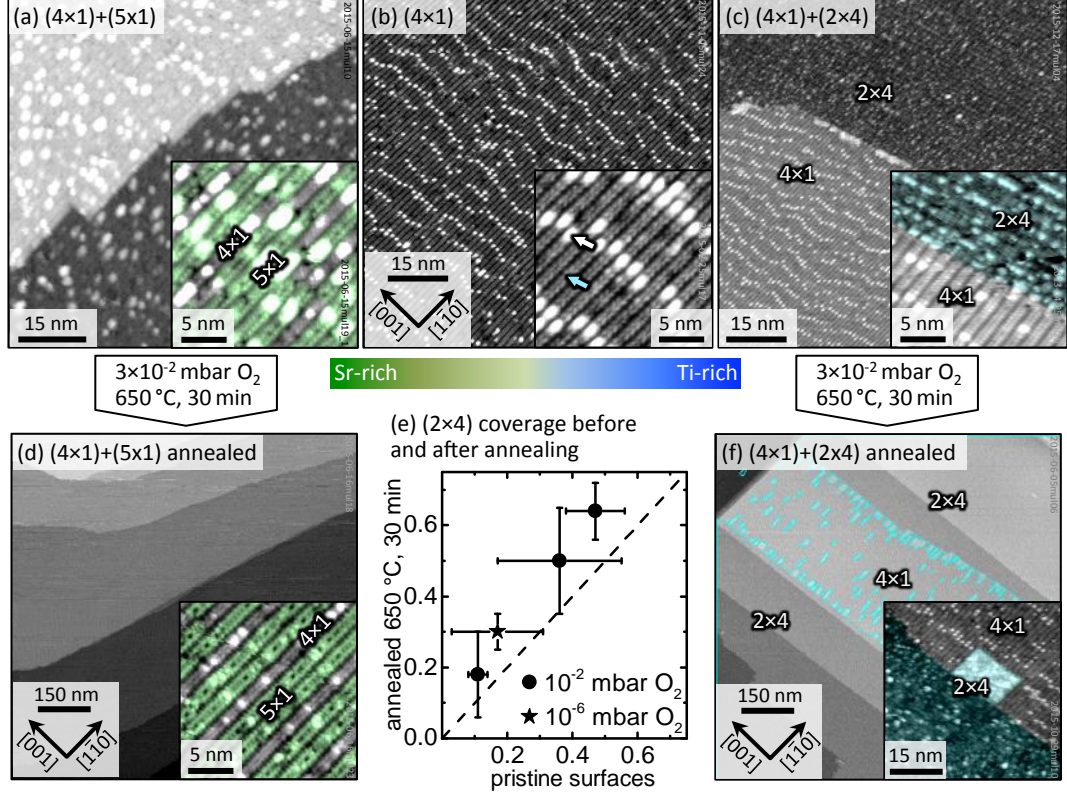


FIGURE 3.39.: STM images of typical pristine SrTiO₃(110) surfaces exhibiting a (4×1) reconstruction (b), and a mix of (4×1) and (5×1) (a), and a mix of (4×1) and (2×4) (c). The white and cyan arrows in the inset of panel (b) indicate intrinsic Sr adatoms and type-I antiphase domain boundaries, respectively. Panels (d) and (f) show the (4×1) + (5×1) and (4×1) + (2×4) surfaces, respectively, after annealing in typical growth conditions ($T = 650^\circ\text{C}$, $p = 3 \times 10^{-2}$ mbar). Panel (e) shows a quantitative evaluation of (2×4) coverage on a mixed (4×1) + (2×4) reconstructed surface before and after annealing. The error bars correspond to 1 σ standard deviation.

3. Results

homogeneous appearance. Depending on the Sr content of the surface, more or fewer of the (4×1) rows are changed into (5×1) rows [(5×1) lines are highlighted in green in the insets of Figure 3.39(a) and (d)]. On the other hand, when (4×1) and (2×4) reconstructions coexist on the surface, the two structural phases are separated from each other, with a higher degree of separation observed on samples annealed at higher temperatures [see Figure 3.39(c)].

Annealing the $(5\times 1) + (4\times 1)$ surface does not show any obvious changes in the overall appearance – the surface appears similar in STM after annealing [compare panels (a) and (d) in Figure 3.39] and the (5×1) coverage remains unchanged [(5×1) coverage before: 0.77 ± 0.04 ; after: 0.76 ± 0.03]. The $(4\times 1) + (2\times 4)$ surface, on the other hand, is considerably changed after annealing. Small islands exhibiting the (2×4) reconstruction are observed in regions of the initial (4×1) reconstruction [(2×4) areas are highlighted in cyan in Figure 3.39(f)]. This indicates that a changed surface morphology can be expected during ramping of the temperature when preparing for deposition, where small islands on the $(4\times 1) + (2\times 4)$ surface are formed. The surfaces behave similarly when annealing is carried out in 5×10^{-6} mbar O_2 .

It should be noted that an analysis of the fractional coverage of (2×4) reconstruction before and after annealing indicates a slight increase of the (2×4) coverage upon annealing, see Figure 3.39(e).

Island nucleation on (4×1) , (2×4) , and mixed surfaces

In addition to the information about the thermal stability of different surfaces presented above, the growth characteristics of these surfaces was tested. The initial stages of the homoepitaxial growth on the (4×1) surface were already discussed in Section 3.5.1. Here, we compare island nucleation on the (4×1) and on the (2×4) reconstructed surface.

Figure 3.40(a) shows submonolayer amounts deposited onto a mixed $(4\times 1) + (2\times 4)$ surface. Islands grow elongated on both surface structures. Islands on substrate areas exhibiting (4×1) or (2×4) reconstruction show elongation along $[1\bar{1}0]$ [high-lighted in yellow in panel (a)] or $[001]$ direction [highlighted in ma-

3. Results

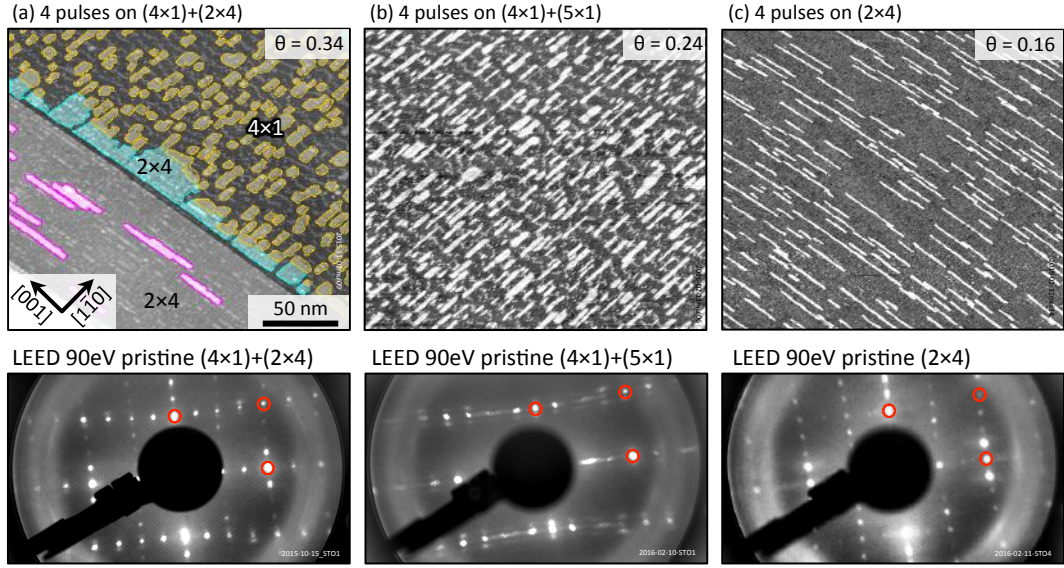


FIGURE 3.40.: (a) STM image of 0.34 ML deposited onto a mixed $(4\times 1) + (2\times 4)$ reconstructed surface. Islands nucleated on (4×1) and (2×4) regions are highlighted in yellow and magenta, respectively. Islands agglomerated at the interface between (4×1) and (2×4) are highlighted in cyan. (b) and (c) show deposition of 4 pulses on fully (4×1) and (2×4) reconstructed surfaces, respectively. The lower panels show the LEED pattern of the corresponding pristine surfaces prior to growth. Deposition and STM parameters: (a) 4.5 J/cm^2 , $5 \times 10^{-6} \text{ mbar O}_2$; $U_S=2.1 \text{ V}$, $I_t=0.4 \text{ nA}$; (b,c) 4.8 J/cm^2 , $5 \times 10^{-6} \text{ mbar O}_2$; $U_S=1.8\text{--}2.1 \text{ V}$, $I_t=0.3 \text{ nA}$.

3. Results

genta], respectively [also see Figures 3.40(b) and (c)]. This indicates anisotropic diffusion or anisotropic sticking to the island edges, with the preferential direction being determined by the underlying surface reconstruction. Furthermore, the islands tend to agglomerate at the border between the two reconstruction phases on the side of the (4×1) reconstruction. Several mechanism could cause these agglomerates. For example, they could be related to the fact that this surface is somewhat unstable when heated, as discussed above. In Figure 3.40(a), the coverage of islands nucleated on (4×1) areas (highlighted in yellow and cyan) amounts to approximately four times the coverage of islands on (2×4) areas (highlighted in magenta).

Because the situation might be different if the two structures coexist on the surface, we performed a direct comparison of island nucleation on two individually prepared surfaces. We deposited 4 pulses in similar PLD conditions ($f = 4.8 \text{ J/cm}^2$, $T = 650^\circ\text{C}$, $p = 5 \times 10^{-6} \text{ mbar O}_2$), onto exclusively (4×1) , and (2×4) reconstructed surfaces [see Figures 3.40(b) and (c)]. After deposition of 4 pulses, the island coverage on the (4×1) surface amounted to 0.243 ± 0.016 , while the coverage on the (2×4) surface was only 0.159 ± 0.015 . Since we did not observe any signs of step flow growth on the (2×4) surface, *i.e.*, no irregularly shaped step edges were observed, we conclude that adspecies are more weakly bound to the (2×4) surface, resulting in a higher reevaporation rate from this surface.

These results help to explain the mechanism that leads to the undesired growth of the surface with pits, shown in Figure 3.38. As indicated in Figure 3.35 above, the relatively high laser fluence of 5.7 J/cm^2 causes a rather Ti-rich flux, which in turn will transform the $(n\times 1)$ structures of the pristine substrate surface partially into (2×4) patches (see phase diagram in Section 3.1). While the growth proceeds, adspecies landing on newly created (2×4) areas exhibit intrinsically different diffusion and growth characteristics [see Figure 3.40(b) and (c)]. In particular, the different re-evaporation rate of adspecies on (4×1) and (2×4) areas causes the (2×4) areas to grow only $2/3$ as fast as the (4×1) areas. For a 20 ML thick film, this would result in ~ 6.7 ML deep pits. Given the fact that the pits also exhibit 1–2 ML high rims surrounding them, the 10 ML depth of the pits stated in the

3. Results

inset of Figure 3.38(b) is very close to the expected one, supporting the hypothesis of a different re-evaporation rate.

3.6.6. Using the evolution of surface reconstructions to determine the stoichiometry of thin films

Similar to our approach of preparing nearly perfect STO(110) surfaces by deliberately depositing Sr or Ti metal followed by annealing, homoepitaxial films on STO(110) exhibit a change in surface structure upon non-stoichiometric growth, as seen in Figure 3.36. In this particular deposition of 25 ML, the surface structure has changed from 69 % (4×1) + 31 % (5×1) to 21 % (5×1) + 79 % (6×1). Note that the XPS analysis shown in Figure 3.35 did not indicate considerable Sr-rich growth for this deposition conditions ($f = 3.0 \text{ J/cm}^2$, $T = 750 \text{ }^\circ\text{C}$, $p = 5 \times 10^{-6} \text{ mbar O}_2$). In order to obtain a measure of the film stoichiometry we utilize the calibration of the phase-diagram established by Wang and coworkers [52]. According to their work, a change from (4×1) to (5×1), and to (6×1) reconstruction can be induced by deposition of $0.15 + 0.40 = 0.55 \text{ ML}$ of Sr followed by annealing ($800 \text{ }^\circ\text{C}$) in $5 \times 10^{-6} \text{ mbar O}_2$ (1 ML corresponds to the density of STO(110) unit cells, *i.e.*, $4.64 \times 10^{14} \text{ atoms/cm}^2$). This indicates that the deposition of 25 ML shown in Figure 3.36 has lead to a Sr enrichment of the near-surface region by about $(1 - 0.31) \times 0.15 + 0.79 \times 0.4 = 0.42 \text{ ML}$ of Sr.

In order to relate this apparent Sr-enrichment to the stoichiometry of the PLD-grown thin film we have to make the assumption that all off-stoichiometry accumulates at the STO(110) surface during growth. This is in contrast to reports on PLD growth of the STO(001) surface, as discussed above in Section 3.6. However, in the following we will provide arguments supporting this assumption. We have already shown that 1 ML high islands on STO(110) exhibit the same reconstruction as the substrate layer [see Figure 3.29(a)]. This suggests that the surface layer is in equilibrium with the deposit, which forms sub-surface bulk-like layers. The question is therefore how much of the deviation from the optimal Sr/Ti=1 composition of the PLD flux is incorporated into the growing film. We tested this assumption by performing *ex-situ* XRD on the films, as presented in the following.

3. Results

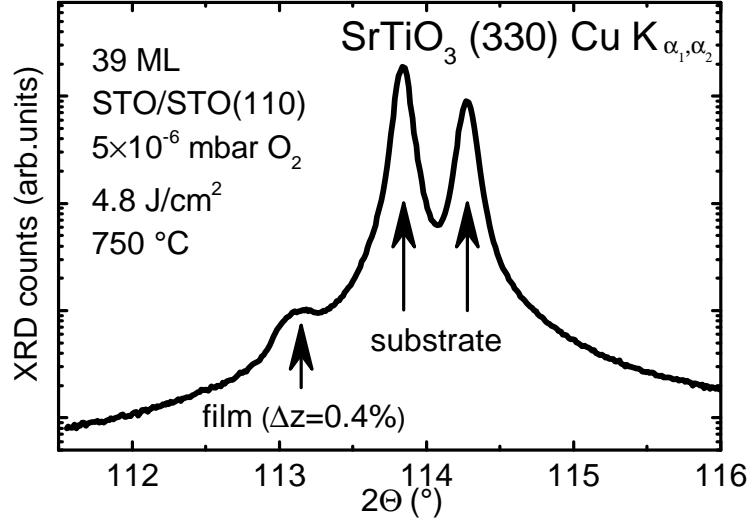


FIGURE 3.41.: X-ray diffraction 2θ scan of a 39 ML thick homoepitaxial STO(110) film showing the (330) Bragg reflection. The vertical axis indicating the diffraction intensity is in logarithmic scale. Peaks derived from the substrate and the film are indicated. The measurement was performed using a symmetric parallel beam geometry.

3.6.7. Test-experiment: Ex-situ XRD characterization

As mentioned in Section 3.6 and shown in Figure 3.34(b), off-stoichiometric growth of the STO(001) surface is typically associated with an expansion of the out-of-plane lattice parameter. We performed XRD on the 39 ML thick film homoepitaxially grown on the STO(110) surface, see Figure 3.41. (This film exhibited an STM-derived off-stoichiometry of $\text{Sr}/\text{Ti}-1 = 0.28\%$; XPS indicated a Sr/Ti ratio within the spread of the pristine surfaces.) Two major peaks appear at 2θ values of 113.8° and 114.3° . These peaks originate from X-rays ($\text{Cu K}\alpha_1$ and $\text{K}\alpha_2$) diffracted at the unstrained bulk STO underneath the film.

In addition to the two main peaks, a side-peak at $2\theta \approx 113.2^\circ$ is visible in the XRD scan. This peak most likely originates from the strained film, indicating an increased out-of-plane lattice parameter for the film. From the Bragg condition, it can be derived that the film exhibits a 0.41% elongated c-lattice parameter. This clearly shows that the film is not free of defects. Still, the remaining question is to which extent these defects are related to the composition of the film, or to the

3. Results

	film 1, 39 ML	film 2, 30 ML
STM-derived PLD-flux off-stoich.	$\frac{\text{Sr}}{\text{Ti}} - 1 = 0.28 \%$	$\frac{\text{Sr}}{\text{Ti}} - 1 = 0.82 \%$
XRD-derived c-lattice expansion	$\frac{\Delta c}{c} = 0.41 \%$	$\frac{\Delta c}{c} = 0.42 \%$
1000 °C post-annealing	—	$\frac{\text{Sr}}{\text{Ti}} - 1 = 1.09 \%$ $\frac{\Delta c}{c} = 0.42 \%$

TABLE 3.3.: Comparison of STM-derived apparent thin film off-stoichiometry with the XRD-derived c-lattice expansion. The third line shows the corresponding values after 1000 °C post-annealing in 5×10^{-6} mbar O_2 for 2 h. Growth conditions for both films: $f = 4.8 \text{ J/cm}^2$, $T = 750 \text{ °C}$, $p = 5 \times 10^{-6}$ mbar O_2 .

PLD process itself.

To further examine the origin of the lattice expansion, we compare the apparent lattice expansion of two films exhibiting a different STM-derived off-stoichiometry, see Table 3.3. Both films were grown with similar PLD parameters ($f = 4.8 \text{ J/cm}^2$, $T = 750 \text{ °C}$, $p = 5 \times 10^{-6}$ mbar O_2). (The difference in apparent stoichiometry might be related to the properties of the excimer laser gas. We experienced a trend to Sr-rich deposition with progressive aging of the laser gas. Additionally, the absorbance of the UV laser entrance window could have changed between the two depositions.) One interesting observation is that both films exhibit a similar XRD-derived lattice expansion, while film 2 appears to be four times as Sr-rich compared to film 1 (as determined by STM). This fact indicates that the stoichiometry has a rather small influence on the defects probed by XRD. In addition, we annealed film 2 (30 ML, $\sim 8.3 \text{ nm}$) to 1000 °C in 5×10^{-6} mbar O_2 for 2 h. While slight changes in the STM-derived near-surface stoichiometry were observed, the XRD result did not change. Even though cation vacancies in STO do exhibit a rather low diffusivity ($\sim 2 \times 10^{-17} \text{ cm}^2/\text{s}$ at $\sim 1050 \text{ °C}$ [116], corresponding to a characteristic diffusion length of $\sim 3.8 \text{ nm}$ within 2 h), the high-temperature annealing is expected to lead to a change in the cation vacancy concentration in the film. Furthermore, the chemical gradient of cation vacancies established between substrate

3. Results

and film would cause an increased diffusivity. Since no changes were observed by XRD, we conclude that extended stoichiometric structural defects (*e.g.*, stacking faults, or Ruddlesden-Popper-like planes) were introduced during the PLD growth.

3.6.8. Discussion: Homoepitaxial multi-layer films on STO(110) and STM-derived stoichiometry determination

We have investigated the growth of homoepitaxial films on the $\text{SrTiO}_3(110)$ surface by means of STM, RHEED, LEED, XPS, and XRD. We successfully deposited up to 39 ML (*i.e.*, ~ 10.8 nm) thick films and were able to characterize the surfaces of the films with high-resolution STM.

We performed XPS measurements in order to determine the stoichiometry of the films. However, already for the pristine, as-prepared substrates, the apparent XPS-derived Sr/Ti ratio varies by a few percent. Such a spread in cation ratios could be related to a non-uniform surface structure across the acceptance area of the photoelectrons (probably >1 mm diameter). Furthermore, the preparation history, *i.e.*, the number of sputtering and annealing cycles applied could change the substrate near-surface cation ratio and result in differences in the apparent composition. The latter possibility is not very likely since we annealed the substrates to 1000°C during preparation, causing the surface to equilibrate with sub-surface regions. In any case, the results suggest that, while trends can be observed in XPS, its accuracy does not allow for a precise determination of changes in the stoichiometry.

A strong dependence of the surface structure after growth on the substrate surface was found. If two inherently different reconstructions coexist on the surface, *e.g.*, $(4\times 1) + (2\times 4)$, a different sticking probability of adspecies results in a different effective deposition rate. The resulting film surface is covered with deep pits, *i.e.*, the films do not develop a well-defined surface morphology.

High-resolution STM analysis before and after growth reveals a change in the surface structure for all films. According to the surface phase diagram (see Fig-

3. Results

ure 3.1), such a change corresponds to an effective increase of either Sr or Ti in the near-surface region during deposition [52]. This approach therefore allows for a precise determination of changes in the near-surface chemical composition.

In order to relate this apparent enrichment in either Sr or Ti to the composition of the PLD-grown films, we have to introduce the following assumption: We assume that any deviation from the optimal Sr/Ti=1 composition of the deposit accumulates at the surface, while the growth proceeds by forming nearly-perfect bulk-like layers. This assumption is supported by the observations presented in the previous section.

Specifically, the results suggest that, in contrast to non-stoichiometric growth at STO(001), the defects observed via expansion of the c-lattice parameter of the STO(110) films are not related to cation nonstoichiometry, but are likely more complex and more stable defects.

If the assumptions we made are valid (we are about to perform high-resolution transmission electron microscopy on PLD-grown thin films to ascertain our assumptions), the evolution of surface structures on the STO(110) surface can be used as a highly sensitive probe of the stoichiometry of thin films. This enables determination of the thin film Sr/Ti ratio with a precision, defined by the film thickness, of well below 1 %.

Figure 3.42 gives an overview of the different depositions we performed. It shows the off-stoichiometry of PLD-grown thin films, as derived by the changes in surface structure from STM, dependent on the deposition pressure and the UV-laser fluence. The figure shows that all films grown at a pressure of 3×10^{-2} mbar O_2 were Sr enriched, in line with the XPS results mentioned in Section 3.6.2. Stoichiometric deposition was only achieved at a deposition pressure on the order of 10^{-6} mbar. We believe that the low optimal pressure is caused by the rather large target-to-substrate distance of the present PLD setup (~ 60 mm). PLD particles traveling along this distance have a high probability of scattering in the background gas. An increased pressure causes an even higher scattering rate and therefore a higher Sr enrichment in the central part of the plasma plume. Therefore, a high pressure during deposition can only be retained by decreasing the distance between

3. Results

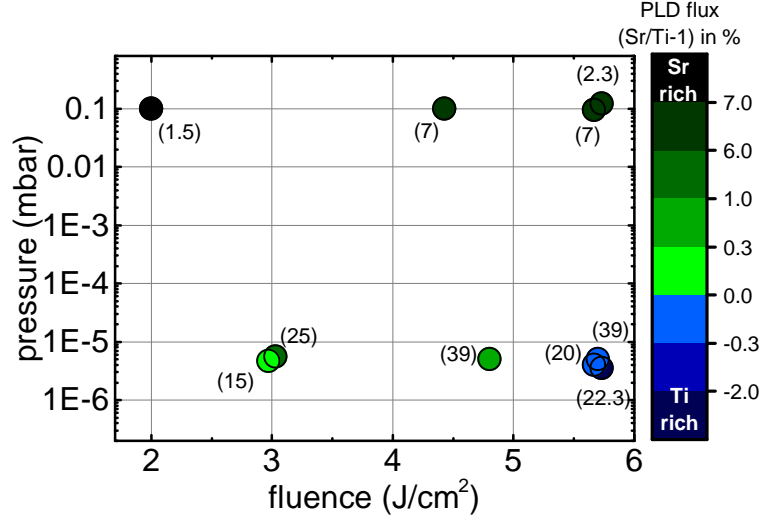


FIGURE 3.42.: Total deposition pressure (O_2) versus UV laser fluence diagram combining results of STM-derived off-stoichiometry for several homoepitaxial STO(110) films. Corresponding film thicknesses (in MLs) are stated in parentheses. The color code indicates different values of $\frac{Sr}{Ti}-1$. Information on the derivation of these values can be found in the text.

target and substrate [compare Figure 3.34(b)]. This could be of importance when growing complex oxides, which are easily reduced. Here, a high O_2 pressure during deposition might be necessary for obtaining sufficiently oxidizing conditions during film growth.

4. Summary

We have studied the structure of the $\text{SrTiO}_3(110)$ surface, the surface chemistry of the $\text{STO}(110)\text{-(}4\times 1\text{)}$ reconstruction, and the homoepitaxial growth of thin films on $\text{STO}(110)$ by PLD.

Central to our study of the $\text{STO}(110)$ surface is the surface phase diagram established by Wang *et al.* [52]. It describes the dependence of the surface reconstructions on the near-surface stoichiometry. This enables us to switch between surface reconstructions on $\text{STO}(110)$, *e.g.*, by deposition of Ti or Sr metal and subsequent annealing. Furthermore, it allows us to associate changes in the surface reconstruction of the PLD-grown thin films with the stoichiometry of the deposited film.

In this thesis, first the already established structure model of the $\text{SrTiO}_3(110)\text{-(}4\times 1\text{)}$ surface reconstruction and the characterization of this structure by means of STM, LEED, RHEED, and NEXAFS were discussed. Two different types of anti-phase domain boundaries (APDBs) were presented; these can be tuned by the oxygen pressure during annealing. These APDBs are intrinsic to this structure and help to relieve surface stress.

We further discuss the transition from $(n\times 1)$ ($n = 4\text{--}6$) to $(2\times m)$ ($m = 4, 5$) reconstructions on this surface. We characterized the (2×5) surface structure by highly resolved STM, LEED, and NEXAFS. This transition is induced by reactive deposition of Ti. In STM, we observed a change from the (4×1) structure exhibiting rows along the $[1\bar{1}0]$ direction, to the (2×5) structure exhibiting rows oriented along $[001]$ direction. NEXAFS revealed a change from tetrahedral coordination of Ti in the (4×1) reconstruction to octahedral coordination of Ti in the (2×5) structure. In cooperation with a number of surface scientists, we have solved the

4. Summary

($2\times m$) structure. It consists of a closely packed double-layer of octahedrally coordinated TiO_6 units. The two-fold periodicity along $[001]$ direction is reflected in the periodic arrangement of five-fold coordinated Sr atoms on the surface, as well as in the arrangement of subsurface units. We concluded that the high coverage of TiO_2 during reactive growth of Ti causes the transition from a network of TiO_4 units to a double-layer of TiO_6 units on the $\text{STO}(110)$ surface.

We further presented details about non-optimal growth of this surface structure, and showed defects of this structure commonly observed in STM. If the Ti deposition amount exceeds the (optimal) amount necessary to form the (2×5) structure, second-layer islands appear. Similar to the (2×5) structure, this second layer exhibits a structure consisting of rows along $[001]$ direction. However, the modulation along $[1\bar{1}0]$ direction (causing the striped appearance) is weak, as compared to the (2×5) structure. In addition, no “ $2\times$ ” periodicity is observed in STM. We therefore named this structure (1×6) reconstruction.

In the second part of this thesis, results about the adsorption of water on the (4×1)-reconstructed surface of $\text{SrTiO}_3(110)$ were presented. The results indicate that water does not adsorb on the stoichiometric surface at room temperature. It adsorbs molecularly at low temperature, or dissociatively at surface oxygen vacancies. In STM, we identified adsorbed water, adsorbed atomic hydrogen, and oxygen vacancies on this surface, and confirmed these assignments with photoemission spectroscopy (PES) results. DFT calculations (performed by coworkers) further confirmed the adsorption characteristics of water. In addition, PES results showed that oxygen vacancies (V_{Os}) can be created by exposure to synchrotron radiation, and that these V_{Os} are associated with the formation of a state ($E_{\text{B}}\sim 1.5$ eV) in the band-gap. By comparing our results with reports in the literature regarding the adsorption of water on tetrahedrally coordinated surfaces, we conclude that the geometry of the surface structure plays an important role in its reactivity. We argue that the TiO_4 tetrahedra on this surface provide a saturated environment for the Ti^{4+} ions and therefore render them inactive for interaction with water.

This thesis further presented the adsorption of Ni metal on the $\text{SrTiO}_3(110)$ -(4×1) surface. STM results showed that single Ni adatoms are formed at room

4. Summary

temperature. The Ni adatoms adsorb at special sites in the reconstruction unit cell, as observed by STM and confirmed by DFT (performed by coworkers). PES results indicated a metallic state of the Ni and the formation of an in-gap state at $E_B \sim 1.9$ eV. Mild annealing leads to the formation of Ni clusters on the surface. DFT predicts a positive adsorption energy, as compared to Ni in the bulk phase. We therefore conclude that the (4×1) surface provides a special template for the adsorption of Ni adatoms and their stabilization at RT.

In the last part regarding the surface chemistry of the $\text{SrTiO}_3(110)-(4 \times 1)$ surface, the adsorption of NiO clusters is presented. The motivation for these experiments comes from reports in the literature showing that the system NiO-STO is an active photocatalyst for water splitting under UV irradiation. While PES results indicate that Ni can be fully oxidized, STM results showed that NiO patches grow on this surface in an irregular fashion. UPS results showed that the adsorption of NiO patches results in a changed onset of the valence band – the band gap was effectively reduced by about 1.5 eV. Furthermore, XPS results showed an upward band bending (up to 0.8 eV) upon adsorption of NiO. Note that these two results are important properties of a photocatalyst. Combining XAS and STM results, we conclude that the adsorption of NiO patches resulted in the distortion or partial disruption of the surface layer. Finally, we confirmed the dissociative adsorption of water on the NiO-modified (4×1) surface by means of PES, and LEIS using isotopically labeled water. The results suggested that the active region for water dissociation is the triple-phase boundary NiO/STO/UHV.

The third part of this thesis presents results of our new pulsed laser deposition (PLD) chamber, which is connected to our surface analysis system. The PLD chamber is equipped with a high-pressure RHEED system, which provides a feedback of the film thickness during growth. The interface of the UHV chambers enables us to perform growth studies without breaking the vacuum. We performed homoepitaxial growth studies on the $\text{STO}(110)$ surface and investigated the early stages of growth. For all depositions, we freshly prepared the substrate surface to predominantly exhibit the (4×1) reconstruction. We stopped the growth at sub-monolayer (ML) amounts, and directly performed STM after cool-down and

4. Summary

transfer to the analysis chamber. STM results showed that islands on the surface exhibit the same reconstruction as the substrate layer, indicating that the reconstruction floats to the top surface and the deposited material forms bulk-like subsurface islands. By combining STM and RHEED results, we confirmed the correspondence of a RHEED intensity oscillation with the ideal layer-by-layer growth on the STO(110) surface. Furthermore, we showed that a simple step-density model, only counting the steps introduced by the islands' circumference, is insufficient for explaining the observed changes in the RHEED intensity. We analyzed the actual step density on the surface from high-resolution STM images, and compared it with the changes in the RHEED intensity. We concluded that, in addition to the steps introduced by the circumference of the islands, the interfaces between two inherently different reconstructions coexisting on the surface have to be considered as steps as well.

By systematically varying the growth parameters with subsequent STM analysis, we observed a strong dependence of the island density and shape on the substrate temperature. In addition, the growth mode can be tuned with the UV laser repetition rate from layer-by-layer growth to a predominant step-flow growth regime.

We further investigated the growth of up to 39 ML thick homoepitaxial films. We first discussed, which processes in PLD strongly influence the stoichiometry of the ablated particles, and conclude that the UV laser fluence and the background gas pressure during deposition are the most relevant parameters. We show that XPS results of several pristine substrates exhibit a few percent spread in the Sr/Ti ratios and conclude that XPS does not allow for a precise determination of the film stoichiometry. However, we confirm literature results regarding the trend for Sr-rich deposition at low UV laser fluences and high deposition pressures. We observed that the surface structure of the resulting film is strongly influenced by non-stoichiometric deposition. Sr-rich deposition (up to 39 ML) results in a change of the surface structure from predominant (4×1) towards the (6×1) reconstruction. This is in accordance with the surface phase diagram showing the dependence of the STO(110) surface structure on the near-surface stoichiometry. Similarly, Ti-

4. Summary

rich growth (~ 20 ML) results in the formation of (2×4) patches on the surface. These patches, when formed during growth, cause deep pits in the film surface. We have performed several experiments to explain this behavior. We believe that the reason for this behavior is a different re-evaporation rate of adspecies from (2×4) areas, as compared to (4×1) areas.

Using the calibration of the surface phase diagram, we were able to translate a specific change of the surface structure during growth quantitatively to a certain enrichment of Sr, or Ti metal in the near-surface region. By assuming that any deviation from the optimal Sr/Ti=1 composition during growth is accumulated at the surface, these results can be related to the stoichiometry of the PLD-grown thin films. The assumption is supported by several observations. First, islands nucleated on the surface indicate that the reconstruction is floating to the top surface. This also indicates that the surface layer is in equilibrium with the deposited material. In addition, we observed a change in the surface structure during growth. In order to test to which extent this off-stoichiometry remains in the bulk of the film, we performed XRD measurements, probing the out-of-plane lattice parameter of the substrate and the film. While we do observe a lattice expansion of the STO(110) films, this expansion does not scale with the STM-derived off-stoichiometry. Furthermore, high-temperature annealing does not change the magnitude of this lattice expansion. We therefore conclude that the PLD process introduces structural defects even in stoichiometric films. Following this approach, the accuracy of determining the stoichiometry of the PLD thin films is only limited by the thickness of the film and the possibility of performing highly-resolved STM after growth.

Bibliography

- [1] U. Diebold, S.-C. Li, and M. Schmid, “Oxide surface science,” in *Annu. Rev. Phys. Chem.*, vol. 61, pp. 129–148, 2010.
- [2] V. Henrich, “The surfaces of metal oxides,” *Rep. Prog. Phys.*, vol. 48, no. 11, pp. 1481–1541, 1985.
- [3] V. Henrich and P. Cox, *The Surfaces of Metal Oxides*. Cambridge University Press, 1994.
- [4] H. Freund, H. Kuhlenbeck, and V. Staemmler, “Oxide surfaces,” *Rep. Prog. Phys.*, vol. 59, no. 3, pp. 283–347, 1996.
- [5] V. Goldschmidt, “Die gesetze der krystallochemie,” *Naturwissenschaften*, vol. 21, pp. 477–485, 1926.
- [6] O. Tufte and P. Chapman, “Electron mobility in semiconducting strontium titanate,” *Phys. Rev.*, vol. 155, no. 3, pp. 796–802, 1967.
- [7] M. Wu, J. Ashburn, C. Torng, P. Hor, R. Meng, L. Gao, Z. Huang, Y. Wang, and C. Chu, “Superconductivity at 93-K in a new mixed-phase Y-Ba-Cu-O compound system at ambient pressure,” *Phys. Rev. Lett.*, vol. 58, no. 9, pp. 908–910, 1987.
- [8] Z. Wang, X. Hao, S. Gerhold, Z. Novotny, C. Franchini, E. McDermott, K. Schulte, M. Schmid, and U. Diebold, “Water adsorption at the tetrahedral titania surface layer of $\text{SrTiO}_3(110)-(4 \times 1)$,” *J. Phys. Chem. C*, vol. 117, no. 49, pp. 26060–26069, 2013.

Bibliography

- [9] S. P. Jiang, “Development of lanthanum strontium manganite perovskite cathode materials of solid oxide fuel cells: a review,” *J. Mater. Sci.*, vol. 43, no. 21, pp. 6799–6833, 2008.
- [10] A. Linz, “Some electrical properties of strontium titanate,” *Phys. Rev.*, vol. 91, no. 3, pp. 753–754, 1953.
- [11] R. Guo, L. Cross, S. Park, B. Noheda, D. Cox, and G. Shirane, “Origin of the high piezoelectric response in $\text{PbZr}_{1-x}\text{Ti}_x\text{O}_3$,” *Phys. Rev. Lett.*, vol. 84, no. 23, pp. 5423–5426, 2000.
- [12] G. Kwei, A. Lawson, S. Billinge, and S. Cheong, “Structures of the ferroelectric phases of barium-titanate,” *J. Phys. Chem.*, vol. 97, no. 10, pp. 2368–2377, 1993.
- [13] B. Stöger, M. Hieckel, F. Mittendorfer, Z. Wang, M. Schmid, G. S. Parkinson, D. Fobes, J. Peng, J. E. Ortmann, A. Limbeck, Z. Mao, J. Redinger, and U. Diebold, “Point defects at cleaved $\text{Sr}_{n+1}\text{Ru}_n\text{O}_{3n+1}(001)$ surfaces,” *Phys. Rev. B*, vol. 90, no. 16, 2014.
- [14] P. Tasker, “Stability of ionic-crystal surfaces,” *J. Phys. C*, vol. 12, no. 22, pp. 4977–4984, 1979.
- [15] H.-J. Freund and G. Pacchioni, “Oxide ultra-thin films on metals: new materials for the design of supported metal catalysts,” *Chem. Soc. Rev.*, vol. 37, no. 10, p. 2224, 2008.
- [16] J. I. J. Choi, W. Mayr-Schmölzer, F. Mittendorfer, J. Redinger, U. Diebold, and M. Schmid, “The growth of ultra-thin zirconia films on $\text{Pd}_3\text{Zr}(0001)$,” *J. Phys. Condens. Matter*, vol. 26, no. 22, p. 225003, 2014.
- [17] C. Freysoldt, P. Rinke, and M. Scheffler, “Ultrathin oxides: Bulk-oxide-like model surfaces or unique films?,” *Phys. Rev. Lett.*, vol. 99, no. 8, p. 086101, 2007.

Bibliography

- [18] A. Atkinson, S. Barnett, R. Gorte, J. Irvine, A. Mcevoy, M. Mogensen, S. Singhal, and J. Vohs, “Advanced anodes for high-temperature fuel cells,” *Nature Mater.*, vol. 3, no. 1, pp. 17–27, 2004.
- [19] E. Dagotto, “Physics - when oxides meet face to face,” *Science*, vol. 318, no. 5853, pp. 1076–1077, 2007.
- [20] T. Ohsawa, K. Iwaya, R. Shimizu, T. Hashizume, and T. Hitosugi, “Thickness-dependent local surface electronic structures of homoepitaxial SrTiO_3 thin films,” *J. Appl. Phys.*, vol. 108, no. 7, p. 073710, 2010.
- [21] R. Shimizu, K. Iwaya, T. Ohsawa, S. Shiraki, T. Hasegawa, T. Hashizume, and T. Hitosugi, “Atomic-scale visualization of initial growth of homoepitaxial SrTiO_3 thin film on an atomically ordered substrate,” *ACS Nano*, vol. 5, no. 10, pp. 7967–7971, 2011.
- [22] R. Shimizu, T. Ohsawa, K. Iwaya, S. Shiraki, and T. Hitosugi, “Epitaxial growth process of $\text{La}_{0.7}\text{Ca}_{0.3}\text{MnO}_3$ thin films on $\text{SrTiO}_3(001)$: Thickness-dependent inhomogeneity caused by excess Ti atoms,” *Cryst. Growth Des.*, vol. 14, no. 4, pp. 1555–1560, 2014.
- [23] K. Fuchigami, Z. Gai, T. Z. Ward, L. F. Yin, P. C. Snijders, E. W. Plummer, and J. Shen, “Tunable metallicity of the $\text{La}_{5/8}\text{Ca}_{3/8}\text{MnO}_3(001)$ surface by an oxygen overlayer,” *Phys. Rev. Lett.*, vol. 102, no. 6, p. 066104, 2009.
- [24] A. Tselev, R. K. Vasudevan, A. G. Gianfrancesco, L. Qiao, P. Ganesh, T. L. Meyer, H. N. Lee, M. D. Biegalski, A. P. Baddorf, and S. V. Kalinin, “Surface control of epitaxial manganite films via oxygen pressure,” *ACS Nano*, vol. 9, no. 4, pp. 4316–4327, 2015.
- [25] J. Schooley, W. Hosler, and M. Cohen, “Superconductivity in semiconducting SrTiO_3 ,” *Phys. Rev. Lett.*, vol. 12, no. 17, pp. 474–475, 1964.
- [26] J. Mavroides, J. Kafalas, and D. Kolesar, “Photoelectrolysis of water in cells with SrTiO_3 anodes,” *Appl. Phys. Lett.*, vol. 28, no. 5, pp. 241–243, 1976.

Bibliography

- [27] R. Sum, H. Lang, and H. Guntherodt, “Scanning force microscopy study of single-crystal substrates used for thin-film growth of high-temperature superconductors,” *Physica C*, vol. 242, no. 1-2, pp. 174–182, 1995.
- [28] M. Cardona, “Optical properties and band structure of SrTiO_3 and BaTiO_3 ,” *Phys. Rev.*, vol. 140, no. 2A, pp. A651–A655, 1965.
- [29] V. Henrich, G. Dresselhaus, and H. Zeiger, “Surface defects and electronic-structure of SrTiO_3 surfaces,” *Phys. Rev. B*, vol. 17, no. 12, pp. 4908–4921, 1978.
- [30] B. Reihl, J. Bednorz, K. Muller, Y. Jugnet, G. Landgren, and J. Morar, “Electronic-structure of strontium-titanate,” *Phys. Rev. B*, vol. 30, no. 2, pp. 803–806, 1984.
- [31] Z. Wang, A. Loon, A. Subramanian, S. Gerhold, E. McDermott, J. A. Enterkin, M. Hieckel, B. C. Russell, R. J. Green, A. Moewes, J. Guo, P. Blaha, M. R. Castell, U. Diebold, and L. D. Marks, “Transition from reconstruction toward thin film on the (110) surface of strontium titanate,” *Nano Lett.*, vol. 16, no. 4, pp. 2407–2412, 2016.
- [32] T. Wolfram, E. Kraut, and F. Morin, “ d -band surface states on transition-metal perovskite crystals: 1. qualitative features and application to SrTiO_3 ,” *Phys. Rev. B*, vol. 7, no. 4, pp. 1677–1694, 1973.
- [33] Z. Wang, Z. Zhong, X. Hao, S. Gerhold, B. Stöger, M. Schmid, J. Sanchez-Barriga, A. Varykhalov, C. Franchini, K. Held, and U. Diebold, “Anisotropic two-dimensional electron gas at $\text{SrTiO}_3(110)$,” *Proc. Natl. Acad. Sci. USA*, vol. 111, no. 11, pp. 3933–3937, 2014.
- [34] W. Sitaputra, M. Skowronski, and R. M. Feenstra, “Topographic and electronic structure of cleaved $\text{SrTiO}_3(001)$ surfaces,” *J. Vac. Sci. Technol. A*, vol. 33, no. 3, p. 031402, 2015.

Bibliography

- [35] T. Chien, T. S. Santos, M. Bode, N. P. Guisinger, and J. W. Freeland, “Controllable local modification of fractured Nb-doped SrTiO_3 surfaces,” *Appl. Phys. Lett.*, vol. 95, no. 16, p. 163107, 2009.
- [36] N. P. Guisinger, T. S. Santos, J. R. Guest, T.-Y. Chien, A. Bhattacharya, J. W. Freeland, and M. Bode, “Nanometer-scale striped surface terminations on fractured SrTiO_3 surfaces,” *ACS Nano*, vol. 3, no. 12, pp. 4132–4136, 2009.
- [37] M. Kawasaki, K. Takahashi, T. Maeda, R. Tsuchiya, M. Shinohara, O. Ishiyama, T. Yonezawa, M. Yoshimoto, and H. Koinuma, “Atomic control of the SrTiO_3 crystal-surface,” *Science*, vol. 266, no. 5190, pp. 1540–1542, 1994.
- [38] S. A. Chambers, T. C. Droubay, C. Capan, and G. Y. Sun, “Unintentional F doping of $\text{SrTiO}_3(001)$ etched in HF acid-structure and electronic properties,” *Surf. Sci.*, vol. 606, no. 3-4, pp. 554–558, 2012.
- [39] M. Castell, “Scanning tunneling microscopy of reconstructions on the $\text{SrTiO}_3(001)$ surface,” *Surf. Sci.*, vol. 505, no. 1-3, pp. 1–13, 2002.
- [40] Z. Wang, K. Wu, Q. Guo, and J. Guo, “Tuning the termination of the $\text{SrTiO}_3(110)$ surface by Ar^+ sputtering,” *Appl. Phys. Lett.*, vol. 95, no. 2, p. 021912, 2009.
- [41] Z. Wang, F. Yang, Z. Zhang, Y. Tang, J. Feng, K. Wu, Q. Guo, and J. Guo, “Evolution of the surface structures on $\text{SrTiO}_3(110)$ tuned by Ti or Sr concentration,” *Phys. Rev. B*, vol. 83, no. 15, p. 155453, 2011.
- [42] D. A. Bonnell and J. Garra, “Scanning probe microscopy of oxide surfaces: atomic structure and properties,” *Rep. Prog. Phys.*, vol. 71, no. 4, p. 044501, 2008.
- [43] N. Erdman, O. Warschkow, M. Asta, K. Poepelmeier, D. Ellis, and L. Marks, “Surface structures of $\text{SrTiO}_3(001)$: A TiO_2 -rich reconstruction

Bibliography

- with a $c(4 \times 2)$ unit cell,” *J. Am. Chem. Soc.*, vol. 125, no. 33, pp. 10050–10056, 2003.
- [44] M. Naito and H. Sato, “Reflection high-energy electron-diffraction study on the SrTiO_3 surface-structure,” *Physica C*, vol. 229, no. 1-2, pp. 1–11, 1994.
- [45] H. Tanaka, T. Matsumoto, T. Kawai, and S. Kawai, “Surface-structure and electronic property of reduced $\text{SrTiO}_3(100)$ surface observed by scanning tunneling microscopy spectroscopy,” *Jpn. J. Appl. Phys.*, vol. 32, no. 3B, pp. 1405–1409, 1993.
- [46] T. Kubo and H. Nozoye, “Surface structure of $\text{SrTiO}_3(100)$,” *Surf. Sci.*, vol. 542, no. 3, pp. 177–191, 2003.
- [47] Q. Jiang and J. Zegenhagen, “ $\text{SrTiO}_3(001)\text{-c}(6 \times 2)$: A long-range, atomically ordered surface stable in oxygen and ambient air,” *Surf. Sci.*, vol. 367, no. 2, pp. L42–L46, 1996.
- [48] C. Noguera, “Polar oxide surfaces,” *J. Phys. Condens. Matter*, vol. 12, no. 31, pp. R367–R410, 2000.
- [49] H. Bando, Y. Aiura, Y. Haruyama, T. Shimizu, and Y. Nishihara, “Structure and electronic states on reduced $\text{SrTiO}_3(110)$ surface observed by scanning-tunneling-microscopy and spectroscopy,” *J. Vac. Sci. Technol. B*, vol. 13, no. 3, pp. 1150–1154, 1995.
- [50] J. Brunen and J. Zegenhagen, “Investigation of the SrTiO_3 (110) surface by means of LEED, scanning tunneling microscopy and auger spectroscopy,” *Surf. Sci.*, vol. 389, no. 1-3, pp. 349–365, 1997.
- [51] B. C. Russell and M. R. Castell, “Reconstructions on the polar SrTiO_3 (110) surface: Analysis using STM, LEED, and AES,” *Phys. Rev. B*, vol. 77, no. 24, p. 245414, 2008.
- [52] Z. Wang, J. Feng, Y. Yang, Y. Yao, L. Gu, F. Yang, Q. Guo, and J. Guo, “Cation stoichiometry optimization of SrTiO_3 (110) thin films with

Bibliography

- atomic precision in homogeneous molecular beam epitaxy,” *Appl. Phys. Lett.*, vol. 100, no. 5, p. 051602, 2012.
- [53] M. P. Seah and W. A. Dench, “Quantitative electron spectroscopy of surfaces: A standard data base for electron inelastic mean free paths in solids,” *Surf. Interface Anal.*, vol. 1, no. 1, pp. 2–11, 1979.
- [54] P. A. Thiel and T. E. Madey, “The interaction of water with solid surfaces: fundamental aspects,” *Surf. Sci. Rep.*, vol. 7, no. 6, pp. 211–385, 1987.
- [55] C. Powell and A. Jabalonski, *NIST Electron Inelastic-Mean-Free-Path Database, V 1.2, SRD 71*. Gaithersburg, MD: National Institute of Standards and Technology, 2010.
- [56] E. Stavitski and F. M. F. de Groot, “The CTM4XAS program for EELS and XAS spectral shape analysis of transition metal L edges,” *Micron*, vol. 41, no. 7, pp. 687–694, 2010.
- [57] H. H. Brongersma, M. Draxler, M. de Ridder, and P. Bauer, “Surface composition analysis by low-energy ion scattering,” *Surf. Sci. Rep.*, vol. 62, no. 3, pp. 63–109, 2007.
- [58] G. Binnig, H. Rohrer, C. Gerber, and E. Weibel, “Surface studies by scanning tunneling microscopy,” *Phys. Rev. Lett.*, vol. 49, no. 1, pp. 57–61, 1982.
- [59] U. Diebold, J. F. Anderson, K. O. Ng, and D. Vanderbilt, “Evidence for the tunneling site on transition-metal oxides: $\text{TiO}_2(110)$,” *Phys. Rev. Lett.*, vol. 77, no. 7, pp. 1322–1325, 1996.
- [60] M. Schmid, “http://www.iap.tuwien.ac.at/www/surface/stm_gallery/stm_schematic,” 2016. [Online; accessed March-2016].
- [61] P. R. Willmott and J. R. Huber, “Pulsed laser vaporization and deposition,” *Rev. Mod. Phys.*, vol. 72, no. 1, pp. 315–328, 2000.

Bibliography

- [62] G. Rijnders and D. Blank, “Growth kinetics during pulsed laser deposition,” in *Pulsed Laser Deposition of Thin Films* (R. Eason, ed.), ch. 8, pp. 177–190, New Jersey: Wiley-Interscience, 2007.
- [63] R. Dittmann, “9 - stoichiometry in epitaxial oxide thin films,” in *Epitaxial Growth of Complex Metal Oxides* (G. Koster, M. Huijben, and G. Rijnders, eds.), Woodhead Publishing Series in Electronic and Optical Materials, pp. 231 – 261, Woodhead Publishing, 2015.
- [64] J. Klein, *Epitaktische Heterostrukturen aus dotierten Manganaten*. PhD thesis, Universität zu Köln, 2001.
- [65] D. H. Blank, G. J. Rijnders, G. Koster, and H. Rogalla, “In-situ monitoring by reflective high energy electron diffraction during pulsed laser deposition,” *Appl. Surf. Sci.*, vol. 138, pp. 17–23, 1999.
- [66] R. D. Deslattes, E. G. Kessler, P. Indelicato, L. de Billy, E. Lindroth, and J. Anton, “X-ray transition energies: new approach to a comprehensive evaluation,” *Rev. Mod. Phys.*, vol. 75, pp. 35–99, 2003.
- [67] M. Bass, *Handbook of Optics*, p. 33.72. McGraw-Hill, 1995. table 28.
- [68] J. L. M. van Mechelen, D. van der Marel, C. Grimaldi, A. B. Kuzmenko, N. P. Armitage, N. Reyren, H. Hagemann, and I. I. Mazin, “Electron-phonon interaction and charge carrier mass enhancement in SrTiO_3 ,” *Phys. Rev. Lett.*, vol. 100, no. 22, p. 226403, 2008.
- [69] J. A. Enterkin, A. K. Subramanian, B. C. Russell, M. R. Castell, K. R. Poeppelmeier, and L. D. Marks, “A homologous series of structures on the surface of $\text{SrTiO}_3(110)$,” *Nat. Mater.*, vol. 9, no. 3, pp. 245–248, 2010.
- [70] F. Li, Z. Wang, S. Meng, Y. Sun, J. Yang, Q. Guo, and J. Guo, “Reversible transition between thermodynamically stable phases with low density of oxygen vacancies on the $\text{SrTiO}_3(110)$ surface,” *Phys. Rev. Lett.*, vol. 107, no. 3, p. 036103, 2011.

Bibliography

- [71] Z. Wang, F. Li, S. Meng, J. Zhang, E. W. Plummer, U. Diebold, and J. Guo, “Strain-induced defect superstructure on the $\text{SrTiO}_3(110)$ surface,” *Phys. Rev. Lett.*, vol. 111, no. 5, p. 056101, 2013.
- [72] Z. Wang, X. Hao, S. Gerhold, M. Schmid, C. Franchini, and U. Diebold, “Vacancy clusters at domain boundaries and band bending at the $\text{SrTiO}_3(110)$ surface,” *Phys. Rev. B*, vol. 90, no. 3, p. 035436, 2014.
- [73] L. E. Walle, S. Agnoli, I. H. Svenum, A. Borg, L. Artiglia, P. Krüger, A. Sandell, and G. Granozzi, “High resolution photoemission and x-ray absorption spectroscopy of a lepidocrocite-like TiO_2 nanosheet on $\text{Pt}(110)$ (1×2),” *J. Chem. Phys.*, vol. 135, no. 5, p. 054706, 2011.
- [74] T. Orzali, M. Casarin, G. Granozzi, M. Sambi, and A. Vittadini, “Bottom-Up Assembly of Single-Domain Titania Nanosheets on $(1\times 2)\text{-Pt}(110)$,” *Phys. Rev. Lett.*, vol. 97, no. 15, p. 156101, 2006.
- [75] A. Sutoh, Y. Okada, and S. Ohta, “Cracking efficiency of hydrogen with tungsten filament in molecular beam epitaxy,” *Jpn. J. Appl. Phys.*, vol. 34, no. 2, pp. L1379–L1382, 1995.
- [76] G. S. Parkinson, Z. Novotný, P. Jacobson, M. Schmid, and U. Diebold, “Room temperature water splitting at the surface of magnetite,” *J. Am. Chem. Soc.*, vol. 133, no. 32, pp. 12650–12655, 2011.
- [77] L.-Q. Wang, K. F. Ferris, and G. S. Herman, “Interactions of H_2O with $\text{SrTiO}_3(100)$ surfaces,” *J. Vac. Sci. Technol. A*, vol. 20, no. 1, p. 239, 2002.
- [78] C. Peden, G. S. Herman, I. Z. Ismagilov, and B. D. Kay, “Model catalyst studies with single crystals and epitaxial thin oxide films,” *Catal. Today*, vol. 51, pp. 513–519, 1999.
- [79] N. B. Brookes, F. M. Quinn, and G. Thornton, “The involvement of step and terrace sites in H_2O adsorption on $\text{SrTiO}_3(100)$,” *Phys. Scripta*, vol. 36, pp. 711–714, 1987.

Bibliography

- [80] L. R. Merte, G. Peng, R. Bechstein, F. Rieboldt, C. A. Farberow, L. C. Grabow, W. Kudernatsch, S. Wendt, E. Lægsgaard, M. Mavrikakis, and F. Besenbacher, “Water-mediated proton hopping on an iron oxide surface,” *Science*, vol. 336, pp. 889–893, 2012.
- [81] S. Wendt, J. Matthiesen, R. Schaub, E. K. Vestergaard, E. Lægsgaard, F. Besenbacher, and B. Hammer, “Formation and splitting of paired hydroxyl groups on reduced $\text{TiO}_2(110)$,” *Phys. Rev. Lett.*, vol. 96, no. 6, p. 066107, 2006.
- [82] M. Lazzeri and A. Selloni, “Stress-driven reconstruction of an oxide surface: The anatase $\text{TiO}_2(001)$ -(1×4) surface,” *Phys. Rev. Lett.*, vol. 87, no. 26, p. 266105, 2001.
- [83] J. Blomquist, L. E. Walle, P. Uvdal, A. Borg, and A. Sandell, “Water dissociation on single crystalline anatase $\text{TiO}_2(001)$ studied by photoelectron spectroscopy,” *J. Phys. Chem. C*, vol. 112, no. 42, pp. 16616–16621, 2008.
- [84] G. Lu, A. Linsebigler, and J. T. Yates, Jr, “ Ti^{3+} defect sites on $\text{TiO}_2(110)$: production and chemical detection of active sites,” *J. Phys. Chem.*, vol. 98, no. 45, pp. 11733–11738, 1994.
- [85] A. C. Dupuis, M. Abu Haija, B. Richter, H. Kuhlenbeck, and H.-J. Freund, “ $\text{V}_2\text{O}_3(0001)$ on $\text{Au}(111)$ and $\text{W}(110)$: growth, termination and electronic structure,” *Surf. Sci.*, vol. 539, no. 1-3, pp. 99–112, 2003.
- [86] M. Abu Haija, S. Guimond, A. Uhl, H. Kuhlenbeck, and H.-J. Freund, “Adsorption of water on thin $\text{V}_2\text{O}_3(0001)$ films,” *Surf. Sci.*, vol. 600, no. 5, pp. 1040–1047, 2006.
- [87] C. Wu, M. S. J. Marshall, and M. R. Castell, “Surface structures of ultrathin TiO_x films on $\text{Au}(111)$,” *J. Phys. Chem. C*, vol. 115, no. 17, pp. 8643–8652, 2011.

Bibliography

- [88] M. H. Farstad, D. Ragazzon, L. E. Walle, A. Schaefer, A. Sandell, and A. Borg, “Water Adsorption on TiO_x Thin Films Grown on $\text{Au}(111)$,” *J. Phys. Chem. C*, vol. 119, no. 12, pp. 6660–6669, 2015.
- [89] X.-F. Yang, A. Wang, B. Qiao, J. Li, J. Liu, and T. Zhang, “Single-atom catalysts: A new frontier in heterogeneous catalysis,” *Acc. Chem. Res.*, vol. 46, no. 8, pp. 1740–1748, 2013.
- [90] B. Qiao, A. Wang, X. Yang, L. F. Allard, Z. Jiang, Y. Cui, J. Liu, J. Li, and T. Zhang, “Single-atom catalysis of CO oxidation using Pt_1/FeO_x ,” *Nat. Chem.*, vol. 3, no. 8, pp. 634–641, 2011.
- [91] Z. Novotný, G. Argentero, Z. Wang, M. Schmid, U. Diebold, and G. S. Parkinson, “Ordered array of single adatoms with remarkable thermal stability: $\text{Au}/\text{Fe}_3\text{O}_4(001)$,” *Phys. Rev. Lett.*, vol. 108, no. 21, p. 216103, 2012.
- [92] G. S. Parkinson, Z. Novotny, G. Argentero, and M. Schmid, “Carbon monoxide-induced adatom sintering in a $\text{Pd}-\text{Fe}_3\text{O}_4$ model catalyst,” *Nat. Mater.*, vol. 12, pp. 724–728, 2013.
- [93] Z. Wang, X. Hao, S. Gerhold, P. Mares, M. Wagner, R. Bliem, K. Schulte, M. Schmid, C. Franchini, and U. Diebold, “Stabilizing single Ni adatoms on a two-dimensional porous titania overlayer at the $\text{SrTiO}_3(110)$ surface,” *J. Phys. Chem. C*, vol. 118, no. 34, pp. 19904–19909, 2014.
- [94] N. S. McIntyre and M. G. Cook, “X-ray photoelectron studies on some oxides and hydroxides of cobalt, nickel, and copper,” *Anal. Chem.*, vol. 47, no. 13, pp. 2208–2213, 1975.
- [95] J. F. Moulder, W. F. Stickle, P. E. Sobol, and K. D. Bomben, *Handbook of X-ray Photoelectron Spectroscopy. A Reference Book of Standard Spectra for Identification and Interpretation of XPS Data*. Perkin-Elmer Corporation, Eden Prairie, MN, 1992.

Bibliography

- [96] H.-C. Fang, Z. H. Li, and K.-N. Fan, “CO oxidation catalyzed by a single gold atom: benchmark calculations and the performance of DFT methods,” *Phys. Chem. Chem. Phys.*, vol. 13, no. 29, p. 13358, 2011.
- [97] J. G. Tao, J. S. Pan, C. H. A. Huan, Z. Zhang, J. W. Chai, and S. J. Wang, “Origin of XPS binding energy shifts in Ni clusters and atoms on rutile TiO₂ surfaces,” *Surf. Sci.*, vol. 602, no. 16, pp. 2769–2773, 2008.
- [98] M. Kitano and M. Hara, “Heterogeneous photocatalytic cleavage of water,” *J. Mater. Chem.*, vol. 20, no. 4, p. 627, 2010.
- [99] A. Fujishima and K. Honda, “Electrochemical photolysis of water at a semiconductor electrode,” *Nature*, vol. 238, pp. 37–38, 1972.
- [100] K. Domen, S. Naito, M. Soma, T. Onishi, and K. Tamaru, “Photocatalytic decomposition of water vapour on an NiO-SrTiO₃ catalyst,” *J. Chem. Soc., Chem. Commun.*, no. 12, pp. 543–544, 1980.
- [101] T. K. Townsend, N. D. Browning, and F. E. Osterloh, “Overall photocatalytic water splitting with NiO_x-SrTiO₃ – a revised mechanism,” *Energy Environ. Sci.*, vol. 5, no. 11, pp. 9543–9550, 2012.
- [102] S. Gerhold, M. Riva, Z. Wang, R. Bliem, M. Wagner, J. Osiecki, K. Schulte, M. Schmid, and U. Diebold, “Nickel-oxide-modified SrTiO₃(110)-(4 × 1) surfaces and their interaction with water,” *J. Phys. Chem. C*, vol. 119, no. 35, pp. 20481–20487, 2015.
- [103] F. De Groot, J. Faber, J. Michiels, and M. T. Czyżyk, “Oxygen 1s x-ray absorption of tetravalent titanium oxides: A comparison with single-particle calculations,” *Phys. Rev. B*, vol. 48, no. 4, pp. 2074–2080, 1993.
- [104] F. May, M. Tischer, D. Arvanitis, M. Russo, and J. H. Dunn, “Modifications of the electronic and magnetic properties of ultrathin Ni/Cu (100) films induced by stepwise oxidation,” *Phys. Rev. B*, vol. 53, pp. 1076–1079, 1996.

Bibliography

- [105] D. N. Tafen, J. Wang, N. Wu, and J. P. Lewis, “Visible light photocatalytic activity in nitrogen-doped TiO_2 nanobelts,” *Appl. Phys. Lett.*, vol. 94, no. 9, p. 093101, 2009.
- [106] S. Gerhold, M. Riva, B. Yildiz, M. Schmid, and U. Diebold, “Adjusting island density and morphology of the $\text{SrTiO}_3(110)-(4\times 1)$ surface: Pulsed laser deposition combined with scanning tunneling microscopy,” *Surf. Sci.*, vol. 651, pp. 76–83, 2016.
- [107] J. Feng, F. Yang, Z. Wang, Y. Yang, L. Gu, J. Zhang, and J. Guo, “Growth of $\text{SrTiO}_3(110)$ film by oxide molecular beam epitaxy with feedback control,” *AIP Adv.*, vol. 2, no. 4, p. 041407, 2012.
- [108] S. Wicklein, A. Sambri, S. Amoruso, X. Wang, R. Bruzzese, A. Koehl, and R. Dittmann, “Pulsed laser ablation of complex oxides: The role of congruent ablation and preferential scattering for the film stoichiometry,” *Appl. Phys. Lett.*, vol. 101, no. 13, p. 131601, 2012.
- [109] T. Linderoth, J. Mortensen, K. Jacobsen, E. Laegsgaard, I. Stensgaard, and F. Besenbacher, “Homoepitaxial growth of Pt on $\text{Pt}(100)\text{-hex}$: Effects of strongly anisotropic diffusion and finite island sizes,” *Phys. Rev. Lett.*, vol. 77, no. 1, pp. 87–90, 1996.
- [110] H. Brune, “Microscopic view of epitaxial metal growth: nucleation and aggregation,” *Surf. Sci. Rep.*, vol. 31, no. 4-6, pp. 125–229, 1998.
- [111] B. Dam, J. H. Rector, J. Johansson, and S. Kars, “Stoichiometric transfer of complex oxides by pulsed laser deposition,” *Appl. Surf. Sci.*, vol. 96-98, pp. 679–684, 1996.
- [112] T. Ohnishi, M. Lippmaa, T. Yamamoto, S. Meguro, and H. Koinuma, “Improved stoichiometry and misfit control in perovskite thin film formation at a critical fluence by pulsed laser deposition,” *Appl. Phys. Lett.*, vol. 87, no. 24, 2005.

Bibliography

- [113] C. M. Brooks, L. F. Kourkoutis, T. Heeg, J. Schubert, D. A. Muller, and D. G. Schlom, “Growth of homoepitaxial SrTiO_3 thin films by molecular-beam epitaxy,” *Appl. Phys. Lett.*, vol. 94, no. 16, p. 162905, 2009.
- [114] Y. Tokuda, S. Kobayashi, T. Ohnishi, T. Mizoguchi, N. Shibata, Y. Ikuhara, and T. Yamamoto, “Growth of Ruddlesden-Popper type faults in Sr-excess SrTiO_3 homoepitaxial thin films by pulsed laser deposition,” *Appl. Phys. Lett.*, vol. 99, no. 17, p. 173109, 2011.
- [115] G. Rijnders and D. Blank, “In situ diagnostics by high-pressure RHEED during PLD,” in *Pulsed Laser Deposition of Thin Films* (R. Eason, ed.), ch. 4, pp. 85–97, New Jersey: Wiley-Interscience, 2007.
- [116] R. Meyer, R. Waser, J. Helmbold, and G. Borchardt, “Observation of vacancy defect migration in the cation sublattice of complex oxides by ^{18}O tracer experiments,” *Phys. Rev. Lett.*, vol. 90, no. 10, p. 105901, 2003.

A. Appendix

A.1. Determination of UV laser spot size

Figure A.1 shows a zoomed photo of a polished, polycrystalline Cu target, used to determine the UV laser spot size. The values f indicate different distances of the focusing lens from the target. The dimensions (in mm) of the UV laser spot and area are stated below individual spots. Using a Cu target instead of thermal paper represents a more clean and well-defined way of determining the UV spot dimensions. Potential problems may arise for the Cu target when using a large UV laser spot, as the resulting low UV laser fluence may be insufficient for ablating Cu. We have used the UV spot with $f = 32$ shown in Fig. A.1 for the experiment presented in Section 3.6 of this thesis.

A.2. Reproducible alignment of target and substrate

The alignment of the substrate and target with respect to each other is a crucial step in a pulsed laser deposition. This is because the PLD flux varies strongly with the angle of emission (ablation). Prior to growth we therefor always aligned the target and the substrate within the red pilot laser of the heating laser, which provides a well-defined reference. Figure A.2 shows three steps within this alignment procedure. First, the Cu target is centered with the red pilot laser. Fig. A.2(a) shows a photograph from the IR-laser (and red pilot laser) entrance window. The back-reflection of the red light is used in addition to the align the target rotation with the axis of the red pilot laser. As a second step, the UV laser is focused into

A. Appendix

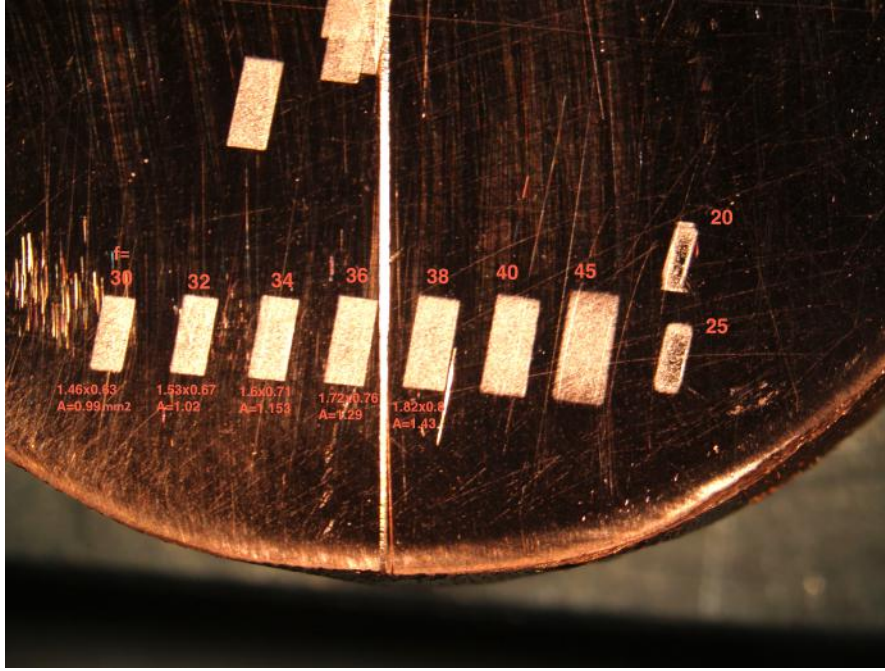


FIGURE A.1.: Zoomed photo of polished, polycrystalline Cu target for determination of UV laser spot width. The focal distances f indicate different distances of the focusing lens from the target. The corresponding UV spot dimensions and areas measured in mm are mentioned below individual spots.

A. Appendix

the center of the Cu-alignment-target. Fig. A.2(b) shows a photograph from the UV laser entrance window. The inset shows a zoomed view of the target inside vacuum with the red pilot laser spot visible. Using the last UV laser mirror, the UV laser is positioned into the center of the Cu target. As a last step, the substrate is positioned within the red pilot laser light. Fig. A.2(c) shows again a view from the IR laser entrance window. It shows the heater stage with the substrate visible as a black square (*cf.* sample mounting in Section 2.11). After these alignment steps, the UV laser spot on the target and the substrate are aligned, and the plasma plume expands directly towards the substrate.

A.3. Magnetic Disturbances influencing the RHEED

This section exemplifies potential problems that could arise in a lab situated inside the city center. Upon arrival and commissioning of our new pulsed laser deposition (PLD) chamber, we immediately recognized a problem with the RHEED analysis. That is, we were not able to obtain a condition with a stable RHEED specular spot intensity.

Figure A.3 shows the intensity of the RHEED specular spot acquired during daytime and during night. The stability of the RHEED intensity is clearly dependent on the time of day. This dependence is especially obvious in Figure A.4(a) showing the vertical position of the direct RHEED beam on the phosphor screen measured over several hours (acquired with the kSA software). The different colors indicate different measurements with and without an additional mu-metal shielding installed. The influence on the direct beam position is considerably reduced starting from about half past midnight. This indicated that the public transport might be the origin of the influence. In front of the laboratory building (the lab is in the 4th floor) is a streetcar station, and these wagons are powered by a overhead line. Upon acceleration most likely there is a high drag of current, producing a strong magnetic field, which in turn influences the RHEED beam in the lab. Indeed, after installing a specially designed mu-metal shielding (see Fig. A.5), which

A. Appendix

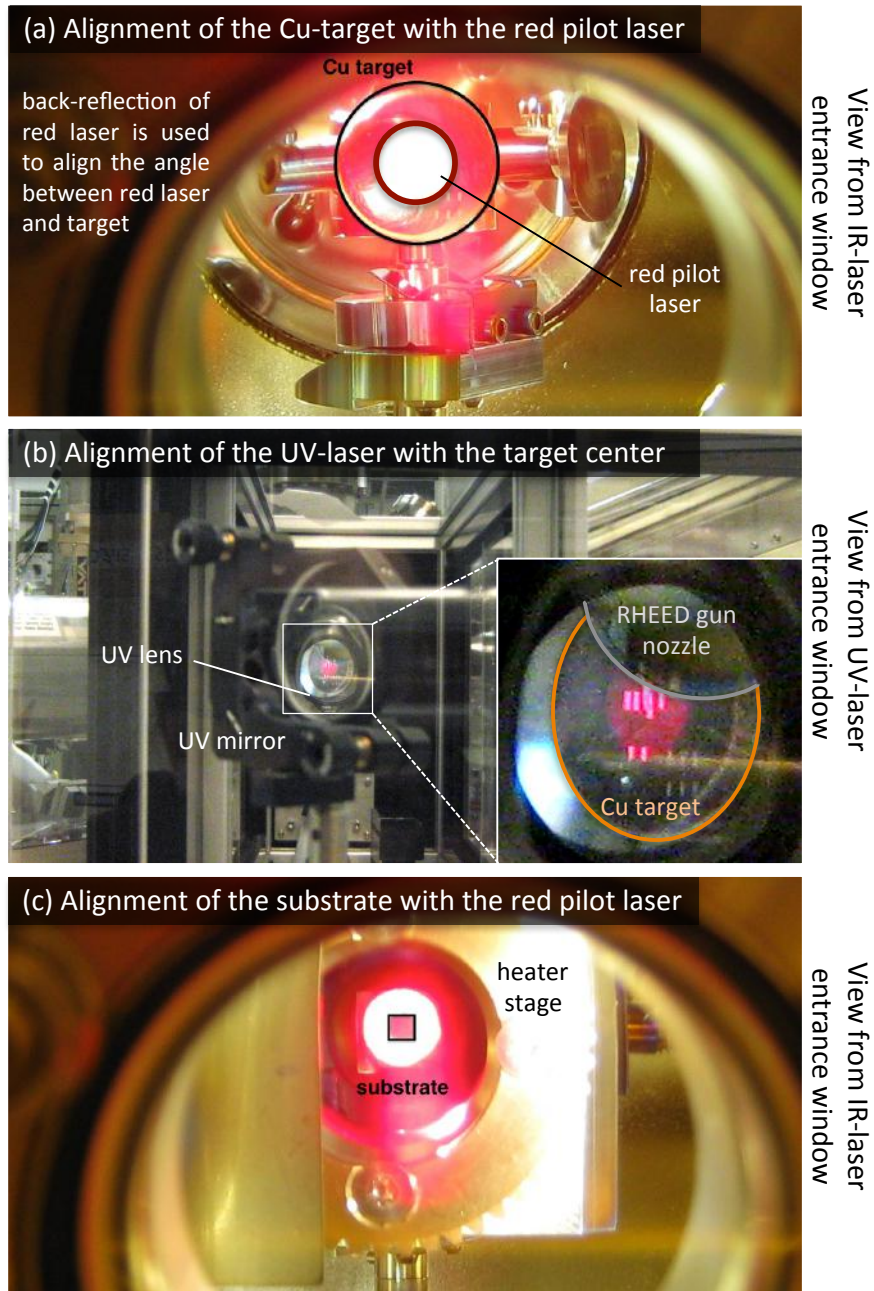


FIGURE A.2.: Photographs explaining the procedure to align substrate and target prior to PLD growth.

A. Appendix

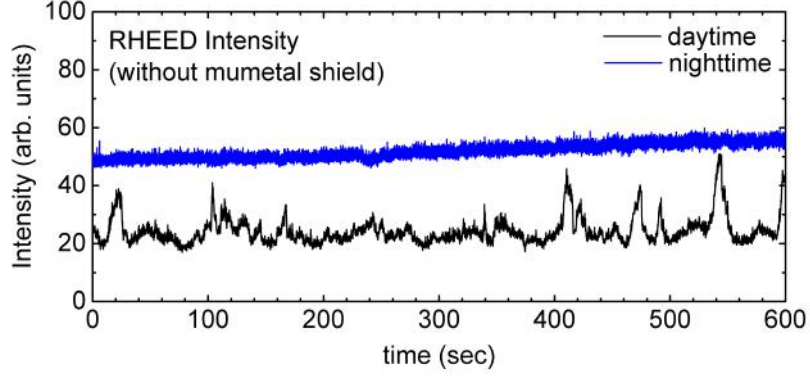


FIGURE A.3.: Stability of the RHEED specular spot intensity as acquired in the in-phase condition ($\sim 1^\circ$ grazing incidence) during daytime (black curve) and during nighttime (blue curve).

covers the whole RHEED gun outside of vacuum, the magnetic influence on the direct RHEED spot position is reduced by a factor of two, see Figure A.4(b).

A. Appendix

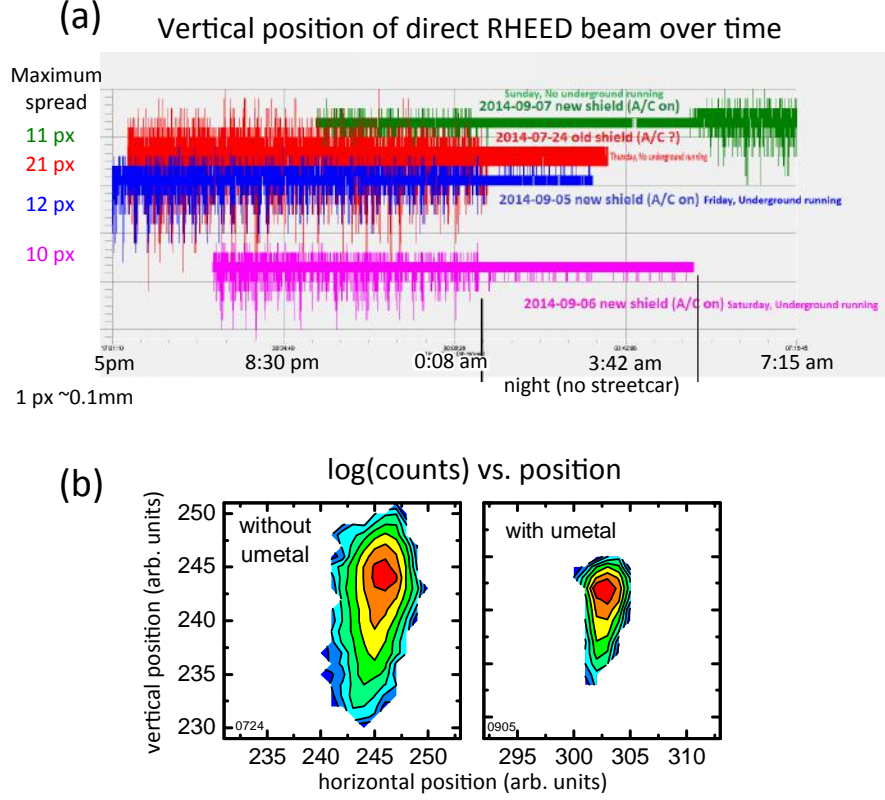


FIGURE A.4.: (a) Vertical position of the pixel with the highest intensity during an acquisition of the direct RHEED beam over several hours including daytime (with the streetcar in operation in front of the university building) and nighttime (with no public transport). (b) Position of direct RHEED spot (determined from the pixel with the highest intensity) over several hours before (left), and after (right) mounting of the mu-metal shielding. The color code indicates different numbers of counts (red stands for high counts, blue for low counts).

A. Appendix

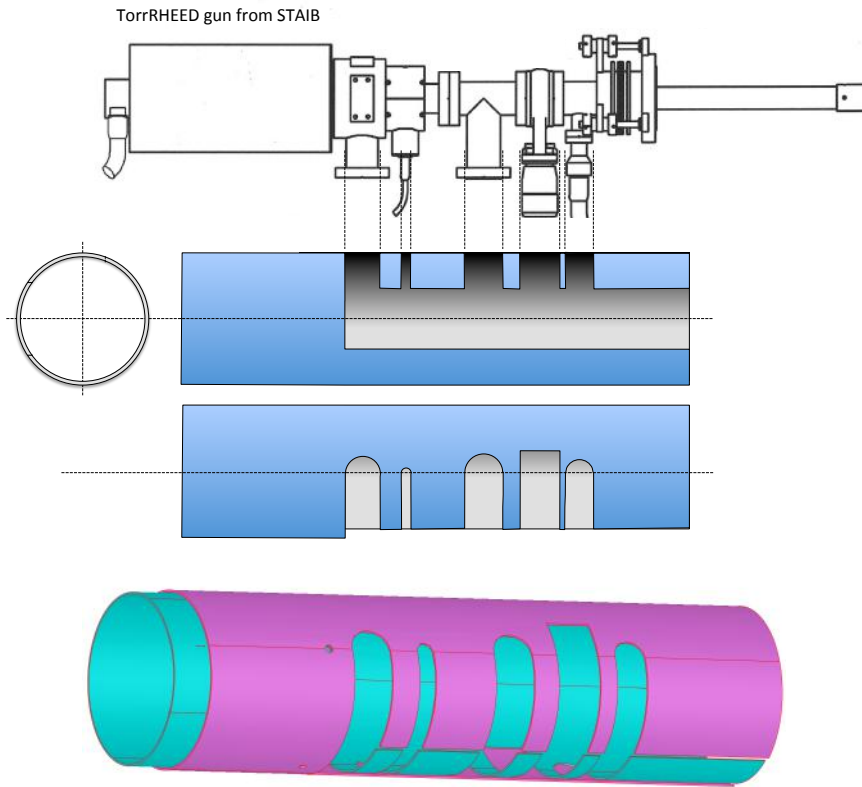


FIGURE A.5.: Upper panel: Technical drawing of the TorrRHEED gun (adapted from a technical drawing by Staib Instruments). Center panels: Mu-metal shielding designed to cover the part of the RHEED gun outside of vacuum. The lowest panel shows two mirrored mu-metal shieldings which are rotated after mounting to cover most of the gun with two layers of mu-metal.

CURRICULUM VITAE

STEFAN GERHOLD



PERSONAL INFORMATION

Born in Wels, Austria, 01 May 1986

email s.gerhold@gmail.com

EDUCATION

PhD Studies	Vienna University of Technology, Vienna, Austria
<i>2013-2016</i>	PhD thesis: "Surface Reactivity and Homoepitaxial Growth of Strontium Titanate (110)" Supervisor: Prof. Ulrike Diebold
Undergraduate	TU Wien, Vienna, Austria
Studies	Master thesis: "Investigation of SrTiO ₃ (001) and (110) Surfaces"
<i>2006-2013</i>	Supervisor: Prof. Ulrike Diebold
Secondary School	HTL Wels, Austria
<i>2000-2005</i>	

PUBLICATIONS

as first author	<ul style="list-style-type: none">• "Homoepitaxial Growth of SrTiO₃(110)-(4×1) Surface: Influence of Surface Structure on the Growth and Determination of the PLD Flux Stoichiometry, in preparation• "Adjusting Island Density and Morphology of the SrTiO₃(110)-(4×1) Surface: Pulsed Laser Deposition Combined with Scanning Tunneling Microscopy, Surf. Sci. 651 (2016) 76• "Nickel-Oxide-Modified SrTiO₃(110)-(4×1) Surfaces and Their Interaction with Water, J. Phys. Chem. C 119 (2015) 20481• "Stoichiometry-Driven Switching Between Surface Reconstructions on SrTiO₃(001)", Surf. Sci. 621 (2014) L1
-----------------	---

as co-author

- “*Bridging the gap: New experimental approach to oxygen tracer diffusion on $\text{SrTiO}_3(110)$* ”, Riva M. *et al.* ,in preparation
- “*Transition From Reconstruction Toward Thin Film on the (110) Surface of Strontium Titanate*”, Wang Z. *et al.* , Nano Lett. 16 (2016) 2407
- “ *$\text{Fe}_3\text{O}_4(110)-(1\times 3)$ Revisited: Periodic (111) Nanofacets*”, Parkinson G.S. *et al.* , Surf. Sci. 649 (2016) 120
- “*Adsorption and Incorporation of Transition Metals at the Magnetite $\text{Fe}_3\text{O}_4(001)$ Surface*”, Bliem R. *et al.* , Phys. Rev. B 92 (2015) 075440
- “*Stabilizing Single Ni Adatoms on a Two-Dimensional Porous Titania Overlayer at the $\text{SrTiO}_3(110)$ Surface*”, Wang Z. *et al.* , J. Phys. Chem. C 118 (2014) 19904
- “*Vacancy Clusters at Domain Boundaries and Band Bending at the $\text{SrTiO}_3(110)$ Surface*”, Wang Z. *et al.* , Phys. Rev. B 90 (2014) 035436
- “*Anisotropic two-dimensional electron gas at $\text{SrTiO}_3(110)$* ”, Wang Z. *et al.* , PNAS 111 (2014) 3933
- “*Water Adsorption at the Tetrahedral Titania Surface Layer of $\text{SrTiO}_3(110)-(4\times 1)$* ”, Wang Z. *et al.* , Surf. Sci. 621 (2014) L1
- “*Photoelectron angular distributions of Cu, Ag, Pt and Au samples: experiments and simulations*”, Tasneem G. *et al.* , Surf. Int. Anal. 43 (2011) 934